Surface Force Analysis and Application of DLVO Modeling in Predicting and Controlling Fines Migration in Sandstone Reservoirs

Rizwan Muneer

Lead Supervisor: Prof. Peyman Pourafshary

Internal Co-Supervisor: Dr. Timur Atabaev

External Co-Supervisor: Dr. Muhammad Rehan Hashmet

A thesis submitted in fulfillment of the requirements for the degree of

Doctor of Philosophy

Department of Petroleum Engineering

School of Mining and Geosciences

2023

Originality Statement

I hereby state that the work presented in this submission is entirely my own, and I attest that it does not include any materials that have been previously published or written by someone else, except in cases where appropriate acknowledgment is given in the thesis. Furthermore, I affirm that the intellectual content of this thesis is a product of my independent effort, and no substantial parts of this material have been used to fulfill the requirements for any other degree or diploma at Nazarbayev University or any other educational institution.

Signature: 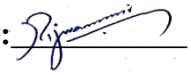

Date: August 2023

Dedication

I dedicate my thesis wholeheartedly to my beloved parents, my dear wife Mariam Shakeel, and my lovely son Muhammad Shaheer, whose unwavering love, support, and understanding have been my guiding lights throughout this challenging academic pursuit. To my parents, your sacrifices and belief in me have been the foundation of my determination; to my wife, your encouragement and presence have brought joy to even the toughest moments; and to my son, your innocent and lovely smiles have fueled my passion to achieve more. Though physically apart during my Ph.D. studies, you remained the source of my strength and inspiration.

May this dedication be a humble expression of my gratitude and a testament to the profound impact they have had on my life and this academic achievement.

With all my love and devotion,

Rizwan Muneer

Acknowledgments

I am immensely grateful and humbled as I stand on the threshold of completing this thesis, a journey that has been filled with invaluable experiences and learning. At this moment, I wish to express my heartfelt gratitude to the individuals who have been instrumental in making this accomplishment possible.

First and foremost, I extend my deepest appreciation to my supervisor, Prof. Peyman Pourafshary. His unwavering support, expert guidance, and profound knowledge have been the driving force behind this thesis. His mentorship has not only refined my research abilities but has also inspired me to explore new horizons in academia. I am truly fortunate to have had the privilege of working under his guidance.

I am equally indebted to my co-supervisors, Dr. Timur Atabaev and Dr. Muhammad Rehan Hashmet, for their invaluable contributions and support throughout this academic journey. Their insightful feedback, dedication, and encouragement have been instrumental in shaping this thesis into its present form. Their passion for research and commitment to excellence have been a constant source of inspiration for me.

I am immensely grateful to Prof. Randy Hazlett, Dean of the School of Mining and Geosciences, and Prof. Ali Mortazavi, for their insightful feedback on my research. Their guidance has significantly improved the quality of my work, and I am obliged for their expertise and assistance.

I extend my sincerest thanks to Mr. Gylym Sapinov, Senior Laboratory Coordinator, for his continuous assistance throughout my research. His expertise and technical knowledge have been instrumental in the success of my experiments and data collection. Whenever I faced challenges in the laboratory, he was always there with a helping hand. His commitment to fostering a conducive research environment has made a substantial impact on my work.

Thank you all for being part of this incredible journey and for making my pursuit of knowledge a rewarding and fulfilling experience.

Abstract

Sandstone reservoirs contain ultra-fine particles of quartz and clay attached to the sand surface. This creates a sand-fine-brine (SFB) system maintained by electrostatic and gravitational forces. Various forces, including van der Waals attraction and electric double-layer repulsion, affect the interaction between fine particles and sand grains in high salinity formation water. The attractive van der Waals force attaches the fine particles to the sand surface, while the electric double-layer repulsion force tends to detach them. Fines can be released and migrate under certain conditions, affecting injectivity and productivity. Formation damage caused by fines migration and pore throat blockage is a well-documented problem in sandstone reservoirs. Current research highlights fines migration as a significant issue affecting the decline in injectivity and productivity due to fines migration and pore throat blocking. Parameters like brine salinity, ionic strength, pH, and flow rate influence fines detachment and movement. In this context, the critical salt concentration (CSC) represents the minimum salt concentration in the injection brine at which fines migration initiates within sandstone reservoirs. The critical pH is the highest pH at which fines migration commences. Similarly, the critical flow rate is the highest flow rate at which fines detach and migrate within the porous media. Low salinity water injection decreases SFB system salinity, leading to fine particle dislodgement and migration. pH changes from alkaline flooding can also trigger fine particle release. Furthermore, hydrodynamic force in high-rate injection or production operations contributes to fines migration. The SFB system has complex dynamics due to the various forces acting on the fine particles and sand grains. The DLVO theory proposed by Derjaguin, Landau, Verwey, and Overbeek is a comprehensive model that accounts for all surface forces in a system and can be used to predict the initiation of fines migration in the SFB system. This thesis proposes a novel approach to applying the DLVO model to the SFB system and predicting critical parameters such as CSC and critical pH.

To carry out this research, outcrop Upper Berea Gray sandstone cores were used, and their average grain and particle sizes and chemical compositions were determined using Scanning Electron Microscopy (SEM) and X-ray Diffraction (XRD). The zeta

potentials of cleaned and dispersed sand grains under varying salinity were measured to define the surface potential of sand grains. The quantified zeta potentials, injection brine salinity, ionic strength, pH, and average fine particle size were used as inputs to calculate surface forces in the SFB system. Using the principle of superposition, the DLVO models were developed for varying salinity and pH scenarios, and CSC and critical pH were predicted by analyzing the total interaction energy of the system under consideration. The shift from negative to positive interaction energy indicated the dominance of the repulsion force in the system. Additionally, the effectiveness of silica nanoparticles was incorporated into the DLVO model, which resulted in the prediction of reduced CSC and improved critical pH. Moreover, the DLVO models showed accurate results for CSCs for both monovalent and divalent brines. Finally, the research proposed a novel fines detachment model that integrated electrostatic, gravitational, and hydrodynamic forces. This model predicted the critical flow rates under varying salinity conditions and accurately determined the initiation of fines migration under high rates. The developed DLVO models were experimentally validated, thus proving their effectiveness in predicting fines migration in porous media. The experimental validation involved measuring the CSC, critical pH, and critical flow rate of the SFB system under varying salinity and pH conditions and comparing the results with the predicted values of the models. The experimental results were found to be in good agreement with the model predictions.

In conclusion, the DLVO modeling approach has the potential to revolutionize the way fines migration is predicted and controlled in sandstone reservoirs. This approach can help avoid the extensive experimentation that is often required for the optimization of EOR processes. The ability to accurately predict fines migration behavior can facilitate the selection of appropriate injection brine salinity, composition, pH, and nanoparticle concentration to minimize the risk of fines migration, pore plugging, and injectivity decline. Further research can make it an invaluable tool for designing waterflooding and alkaline flooding operations for enhanced oil recovery and better reservoir management.

Contents

List of Figures

List of Tables

CHAPTER 1: Introduction and Overview

1.1 Background

Sandstone reservoirs naturally contain ultra-fine particles of quartz and clay attached to the sand surface. This attachment creates what is known as a sand-fine-brine (SFB) system, which is maintained by electrostatic and gravitational forces. In this system, the electric double layers (EDLs) around the fine particles and sand grains are compressed due to the high charge density, keeping the fine particles in equilibrium with the sand grains in the high salinity formation water. The interaction between the fine particles and sand grains in a high salinity formation water is influenced by several forces, including van der Waals attraction, electric double-layer repulsion, and weak Born repulsion. The overall attractive interaction energy of the SFB system affixes the fine particles to the sand's surface, mainly through the van der Waals force, which is proportional to the fine particle size and the distance separating them from the sand surface. The electric double-layer repulsion force, on the other hand, tends to detach the fine particles from the rock surface, and the zeta potential of the SFB system is the primary factor. Under certain conditions, fines can be released and migrated. The movement of fines can be predicted based on factors such as the injected brine's salinity, ionic strength, flow rate, pH, presence of monovalent and divalent ions, and concentration of in-situ fines. When low-salinity water is injected during waterflooding, the SFB system's salinity decreases, and the electric double layers (EDL) around the fines and sand grains expand. This high repulsion force causes fine particles to dislodge and migrate inside the reservoir, even at low flow rates. The detached and migrating fines can block the pore throats, leading to a decrease in productivity and injectivity, as well as a high-pressure drop in the system. The pH of the SFB system can also impact the release of fine particles. After alkaline flooding or waterflooding, the pH of the system may rise due to the solubilization and dissolution of rock minerals like calcite and siderite. When the pH reaches a specific value known as the critical pH, fines may be released due to the increase in the repulsion force. In high-rate injection or production operations, the hydrodynamic force comes into play along with electrostatic and gravitational forces, triggering fines migration in the porous media. Various techniques have been employed to address the issue of fine migration, such as

adjusting the ionic composition and salinity of injection fluids, utilizing nanotechnology, and limiting injection rates below a critical value. However, there is no comprehensive modeling approach available that quantifies surface forces and predicts the initiation conditions for fines migration.

1.2 Problem Statement

Attraction forces are responsible for retaining fines on the rock surface, whereas repulsion forces try to detach fines and promote migration. High injection rates, decreasing water salinity, and an increase in the pH of the system collectively affect the attraction, repulsion, and hydrodynamic forces. At a critical salt concentration (CSC), and critical pH of the system, the total interaction energy of the SFB system shifts from negative to positive due to an increase in repulsion force and expansion of electric double-layer, resulting in the initiation of fines release in the porous media. Similarly, injection/production flow rate is another important factor that significantly affects fines migration. When the flow rate reaches a critical value, the hydrodynamic force takes over the attraction force, which leads to the movement of fines. At a system salinity less than CSC, lifting of fines occurs even at a low injection rate, and the critical flow rate has no significance. Conversely, at a flow rate greater than the critical flow rate, fines migration happens due to rolling/sliding mechanisms, and salinity has no meaning, even if it is higher than CSC. Setting the optimum injection rate, maintaining the system pH below the critical pH, and salinity above the CSC, tuning the ionic composition of injected water, and using nanoparticles (NPs) are practical options to control fines migration in sandstone reservoirs. DLVO modeling explains the total interaction energy between fines and sand grains based on the quantification of the surface forces of the system. Fines migration in sandstone reservoirs has adverse effects on permeability, fluid productivity, and injectivity, and their release, migration, and straining can significantly impair the hydraulic connectivity of the reservoir because fine particles plug the actual path for fluid flow. These effects have been reported in the literature.[1–3]

In the context of controlling fines migration in low-salinity environments, most of the research conducted thus far has been limited to a core scale, with some promising results being reported. However, despite the progress made, there is currently a gap in the

literature regarding the detailed particle-scale DLVO modeling of fines migration phenomena, as well as the effect of NPs in mitigating this problem. Moreover, although there are some discrete critical flow rate models available that describe lifting and rolling mechanisms separately for fines migration in high- and low-salinity systems, there is a lack of comprehensive modeling for a critical flow rate that takes into account electrostatic, gravitational, and hydrodynamic forces, and can accurately estimate the critical injection rate for fines migration initiation in subsurface sandstone formations. Nonetheless, the DLVO model can be a useful tool in predicting the CSC, critical pH, and critical flow rate to prevent fines migration during various enhanced oil recovery (EOR) processes. In order to address these unanswered questions and fill the current gaps in the literature, systematic modeling and experimentation have been required on sandstone outcrops.

1.3 Research Objectives

The main idea of this research is to model fines migration using the DLVO modeling approach under varying system salinity, pH, and injection rate conditions, and to investigate the impact of NPs on CSC. As these variables change, surface forces gradually shift, potentially leading to fines migration in the reservoir under certain conditions.

Based on the earlier discussion, this research aimed to accomplish the following objectives:

- Prediction of critical parameters such as critical salinity, pH, and flow rate by employing the DLVO modeling approach following the quantification of surface forces.
- Application of nanotechnology to prevent formation damage resulting from fines migration, by incorporating the effect of nanoparticles (NPs) in DLVO modeling.
- Validation of the developed models by matching them with observed experimental data.

1.4 Thesis Organization

The thesis includes seven chapters. Chapter 1 serves as the introductory section of this research work, where the background of the study is presented in detail. The chapter highlights the contextual framework of the study, including the problem statement that

outlines the gap in knowledge that the research aims to address. Additionally, this chapter outlines the research objectives, which identify the specific goals that the study aims to achieve. By providing a comprehensive overview of the study's background, problem statement, and research objectives, Chapter 1 sets the basis for the subsequent chapters.

Chapter 2 is devoted to presenting a comprehensive literature review on the fines migration problem that occurs in sandstone reservoirs. The chapter provides an overview of the key factors that trigger this phenomenon, including critical salt concentrations, pH, and flow rates. Additionally, this chapter reviews the existing techniques and solutions that have been developed to address this problem, including the use of surface force analysis and DLVO theory to model the SFB system and nanoparticles. By synthesizing and analyzing relevant literature on fines migration in sandstone reservoirs, this chapter aims to provide a solid foundation for the subsequent chapters that detail the research methodology, findings, and conclusions of the study.

Chapters 3 to 6 comprise the core of this research work, where a comprehensive analysis of surface forces and DLVO modeling is presented in various scenarios considering single-phase flow. Each chapter presents a separate methodology section that is tailored to the parameters being predicted and validated experimentally.

Chapter 3 specifically focuses on predicting and reducing the CSC using DLVO modeling techniques for monovalent and divalent brines. The DLVO models used in this chapter accurately predicted the CSCs and validated them experimentally. Furthermore, the impact of system pH on surface forces and fines migration initiation, which is a critical parameter during alkaline flooding was also investigated in this chapter. The findings of this chapter provide valuable insights into the use of DLVO modeling as a useful tool for predicting fines migration in sandstone reservoirs.

Chapter 4 investigates the application of nanotechnology to reduce CSC and enhance critical pH using the DLVO modeling technique. By accurately predicting the CSC and critical pH using DLVO modeling, this chapter presents a novel approach to control fines migration in sandstone reservoirs during waterflooding and alkaline flooding. The findings of this chapter recommend that nanotechnology has significant potential to enhance the effectiveness of waterflooding and alkaline flooding in sandstone reservoirs. By demonstrating the use of DLVO modeling in predicting the CSC and critical pH for

effective fines migration control, this chapter makes a valuable contribution to the field of reservoir management.

Chapter 5 of this research work presents a novel integrated model for predicting the critical flow rate for fines migration initiation in sandstone reservoirs. The model is developed by considering the influence of various forces such as electrostatic, gravitational, and hydrodynamic forces on fines migration during high-rate injection or production operations. The integrated model is highly effective and accurately predicted the critical flow rate for different salinities and validated the predictions through core flood experiments. This chapter presents a detailed analysis of the impact of different forces on fines migration during high-rate injection or production operations, which is crucial for optimizing reservoir management.

Chapter 6 focuses on upscaling core data to the reservoir scale. It uses DLVO model predictions and coreflood experiment data to accurately translate micro-scale findings to a larger field scale to show the application of the proposed approach.

Chapter 7 marks the conclusion of this research and presents a comprehensive summary of the research findings. The chapter summarizes the effectiveness of DLVO modeling in predicting fines migration, and the critical parameters that trigger this phenomenon. It also offers insights into how the integration of DLVO modeling and nanotechnology can be used to mitigate fines migration. Finally, this chapter presents recommendations for future research, considering the prediction capability of DLVO modeling for a given SFB system under consideration. The research findings and recommendations provide valuable insights for future research on mitigating fines migration in sandstone reservoirs.

CHAPTER 2: Literature Review

Fines migration is primarily caused by changes in the electrostatic surface forces which are triggered by mud invasion during drilling activities, the use of completion fluids, acidizing treatments, and water injection into the reservoir during secondary and tertiary recovery operations. The attraction and repulsion forces are collectively affected by increasing pH and decreasing water salinity. At a specific value of pH known as the critical pH and CSC, the total interaction energy of the SFB system shifts from negative to positive, indicating the initiation of fines release. To control fines migration, practical options include maintaining the system pH below critical pH, setting the salinity above the CSC, tuning the ionic composition of injected water, and use of NPs. The DLVO modeling elucidates the total interaction energy between fines and sand grains by calculating the surface forces of the system. Zeta potential is an important indicator of an increase or decrease in repulsion force in this context. This chapter is based on the results published in the referenced article[a].

2.1 Sandstone Reservoirs

Sandstone reservoirs containing oil are a major source of energy worldwide and account for approximately 60% of the world's petroleum reservoirs.[4] In subsurface porous and permeable sandstone reservoirs that contain various types of clay minerals, the reduction in ionic strength (I_s) and alteration in the ionic composition of the formation water can result in fines migration and a decrease in permeability. These clay minerals are present within the pore space either as agglomerate particles or as fine particles that coat the sand grains. Clay minerals are characterized as aluminosilicates with a layered structure made up of layers of silica, alumina, and magnesia. The three main types of clay minerals are kaolinite, montmorillonite, and illite/mica.[5,6] Sandstones consist of a matrix of quartz grains enclosing an interconnected pore space. The nature of the depositional environment can lead to the presence of siliceous fines due to grain compaction and crushing because of applied stresses as well as fines deposition. These fines are generally held within the

[a] Muneer, R.; Rehan Hashmet, M.; Pourafshary, P. Fine Migration Control in Sandstones: Surface Force Analysis and Application of DLVO Theory. ACS Omega 2020, 5 (49), 31624–31639.

formation water film which surrounds the quartz grain in water-wet conditions.[4] Fines migration may happen in different types of natural and technical processes, such as water aquifer recharging by some external water source, underground formation water disposal, groundwater flows, invasion of drilling muds, invasion of completion fluids, acidizing treatment and waterflooding, high rate oil and gas production and injection, and improper design of oil recovery processes with low salinity water injection.[7–18]

2.2 Fines Migration

Water injection operations into sandstone and carbonate reservoirs performed by reducing the salinity and tuning the ionic composition are promising and evolving technologies to maximize oil recovery, primarily by modifying the wettability of the crude-brine-rock system.[19–28] During the aforementioned process of water-flooding, the salinity, chemistry, and injection rate of injected brine play a vital role in altering the rock wettability and changing the surface forces between fines and sand grains in sandstone reservoirs, which affect the efficiency of the procedure.[20,27–33] Fine particles can detach, become suspended in the injected fluid, and form a colloidal system in the reservoir due to the alteration of attraction and repulsion surface forces; while they move with the injected fluid/ brine, and they may block the pore throats. This phenomenon is referred to as straining: it blocks already open pores and results in formation damage, with a substantial decline in the formation permeability,[8,34–37] as shown in Figure 2.1.

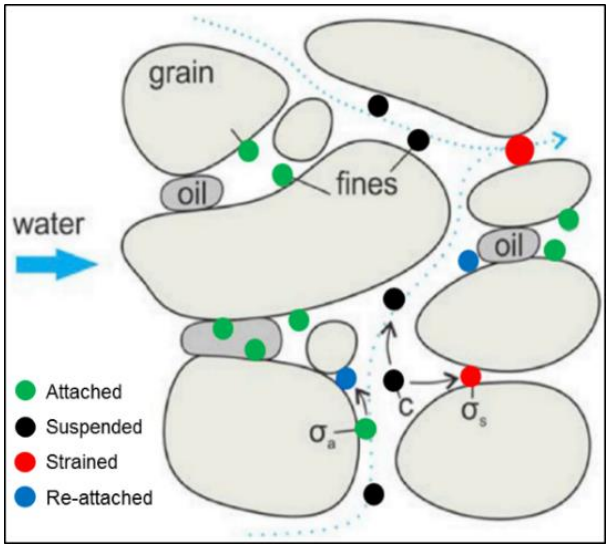

Figure 2.1 Migration of natural fine particles in the reservoir.[37]

Fines migration in sandstone reservoirs is supposed to be one of the possible mechanisms of enhanced oil recovery (EOR) in low-salinity projects. It provides better mobility control by plugging some of the pores, diverting flow towards un-swept sections of the reservoir, and increasing the sweep efficiency, which eventually is favorable for incremental oil recovery.[6,30,31,34,38–44] As yet, fines assisted oil recovery phenomenon is still not well understood and in-depth research on this issue is necessary to address the associated productivity and injectivity decline. On the other hand, fines migration has been reported by some researchers to have adverse effects on fluid productivity and injectivity, and their release, migration, and straining can significantly impair the hydraulic connectivity of the reservoir because they plug the actual path for fluid flow.[1–3,45,46] Russell et al. performed several flooding experiments on unconsolidated cores made of silica sand and kaolinite and investigated permeability loss when injection fluid ionic strength decreased from high to low salinity under a constant flow rate. They observed a substantial decrease in permeability from 500 mD to ~20 mD when injection fluid NaCl salinity decreased from 0.6M to 0.0001M.[47] Yu, M. et al. conducted coreflood experiments on sandstone samples and an 80% to 99% reduction in permeability was observed during LSW injection while an increase in pressure drop of 200-250 psi was observed. This translates into a pressure gradient of ~600 psi/ft. Such a high-pressure drop is not practical on a field scale as it will certainly fracture the rock.[35] In another study performed by [48] M. et al., around three folds increase in pressure drop was observed during LSW flooding which was attributed to fines detachment and migration in the sand pack. They observed that the oil recovery during LSW flooding was 10-15% lower compared to the nanofluid injection scenario. This reduced productivity during LSW flooding can be attributed to fines release and migration, leading to the blocking of pathways for oil flow. Similarly, the permeability of Berea sandstone cores was decreased from 120 mD to 0.03024 mD in flooding tests performed by A. Al-Sarihi et al. when the injection fluid was switched from high salinity NaCl to deionized water. This huge decrease in permeability was due to an extremely high-pressure drop across a five cm-long core sample. The fines migration not only causes permeability impairment but also adversely affects the oil recovery during low salinity or alkaline flooding by blocking the pore throats. A considerable increase in pressure drop across the core samples during brine injection is a clear indication of the productivity

decline.[40]

2.2.1 Conditions for Fines Migration Initiation

Fines release and migration inside sandstone reservoirs are related to several factors such as the available concentration of fine particles, ionic composition, salinity of injected water, pH, wettability, flow rate, and relative flow of different phases.[12,17,49,50] In the past, Martin[51] performed many waterflooding experiments on sandstone cores and observed that a decrease in injected water salinity resulted in additional oil recovery, accompanied by a decrease in core permeability because of clay swelling. Later, Khilar et al.[52] found that when injected fluid salinity falls below a critical salt concentration, fines are released, and migration starts within porous media. Fines migration and subsequent permeability reduction were also confirmed by experimental research.[12,30,34,39,53–56] Kumar et al.[25] and Mansouri et al.[48] used the scanning electron microscope (SEM), the field emission scanning electron microscope (FESEM), and atomic force microscopy (AFM) to visually show the mobilization of mixed-wet kaolinite particles with high-resolution images. In some recent studies,[56–61] it has been found that CO_2 injection in sandstone, can also lead to permeability reduction due to fines migration. Mineral dissolution caused by CO_2-brine-rock interaction could be the reason for fine particle generation in porous media and the related decline in CO_2 injectivity. Therefore, all these key factors must be considered to get an in-depth understanding of interactive forces between fine particles and sand grains to properly design a solution and mitigate the fines migration problem.

2.2.2 pH Increase

The pH of colloidal dispersions is one of the most important factors that affect the repulsion force, and it is indicated by the change in the zeta potential of the system. Zeta potential is generally positive at low pH values (acidic region), and with increasing pH, it becomes negative because of the presence of excess OH^{-1}. There is a specific pH where zeta potential becomes zero, which is called the point of zero charge (PZC) or the iso-electric point (IEP), as shown in Figure 2.2. For a pH higher than the PZC, the surface charge becomes negative, which means a repulsion force that leads to the separation of fines.

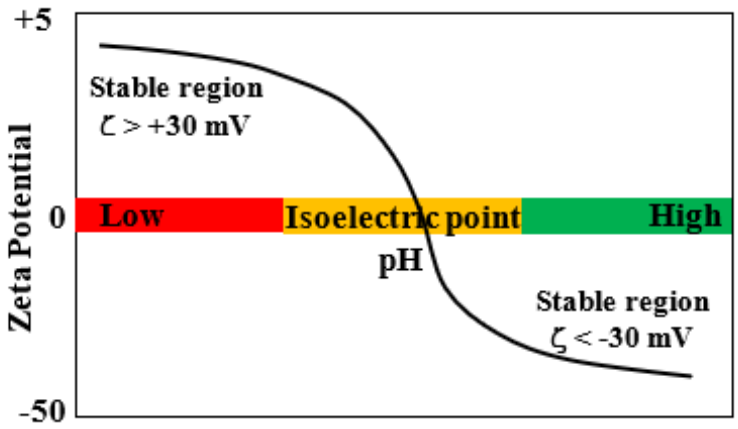

Figure 2.2 Change in zeta potential with the pH of a solution.[62]

During alkaline flooding EOR, the alkali generates in-situ surfactants that reduce the oil-water interfacial tension to maximize oil recovery. However, alkaline flooding in sandstones may cause fines migration problem due to the change in surface potential caused by an alteration in pH. As the pH of the system increases during alkaline flooding, the repulsion force between fine particles and sand grains increases, and the corresponding zeta potential decreases (becomes more negative) because of excess OH^{-1} in the system. This mechanism results in fines detachment and migration during alkaline flooding.

2.2.3 Ionic Strength

The ionic strength (I_s) of the solution affects the expansion and thickness of the EDL, which further affects the repulsion force and total energy of the system. The higher the ionic strength of the solution, the more compressed the EDL becomes. Debye length (k^{-1}) represents the thickness of the electric double layer. It is an important parameter that is influenced by various factors, mainly the brine's ionic strength. The Debye length is reduced as the ionic strength is increased, making the electric double layer thinner. Equation 2.1 is used to compute the Debye length.

$$k^{-1} = \sqrt{\frac{\varepsilon_o \varepsilon K_B T}{2 N_A e^2 I_s}} \tag{2.1}$$

The ionic strength (I_s) of a solution is a measurement of the ions' concentration in that solution. Ionic compounds such as monovalent and divalent salts dissociate into ions when dissolved in water. Equation 2.2 is used to calculate the ionic strength of an

electrolyte solution.

$$I_s = \frac{1}{2}\sum_{j=1}^{n} c_j\, z_j^2 \tag{2.2}$$

The effect of decreasing the ionic strength on the Debye length has been shown in Table 2.1. As the brine salinity decreases, EDLs around the fine particle and the sand grain expand simultaneously, generating more repulsion between the fines and the sand grain. Consequently, detachment of the fines occurs. The low zeta potential confirms the high repulsion force in these conditions.

Table 2.1 Effect of ionic strength on EDL thickness.

I_s of NaCl at 298 K (M)	$k^{-1} = \sqrt{\frac{\varepsilon_o \varepsilon k_B T}{2N_A e^2 I_s}}$	ζ-potential (mV)[63]
0.6	0.4 nm	-17.9
0.4	0.5 nm	-21.3
0.2	0.7 nm	-24.3
0.1	1 nm	-30.5
0.05	1.4 nm	-33.7
0.025	2 nm	-34.0
0.01	3 nm	-34.3

The presence of divalent ions (Ca^{2+}, Mg^{2+}) in the solution is beneficial and can suppress the EDL thickness, resulting in reduced repulsion force as compared to monovalent ions (Na^{+}) for the same salinity. Xie Q. et al.[64] performed experimental research and measured zeta potentials for a solution containing crushed sand particles in the presence of monovalent (Na^{+}) and divalent ions (Ca^{2+}, Mg^{2+}) separately. They observed that divalent ions suppressed the electric double-layer, which was formed around the sand grain and hence, resulted in reduced repulsion, which is indicated by low zeta potential (absolute value) as shown in Figure 2.3. Similar results for zeta potential data were observed in the studies performed by Shehata et al.[65] and Gulgonul[66] on sandstone and natural hydrophobic Teflon, respectively, in the presence of monovalent and divalent ions (Ca^{2+}, Mg^{2+}). Assef et al.[67] also utilized $CaCl_2$ and $MgCl_2$ solutions and performed similar experiments.

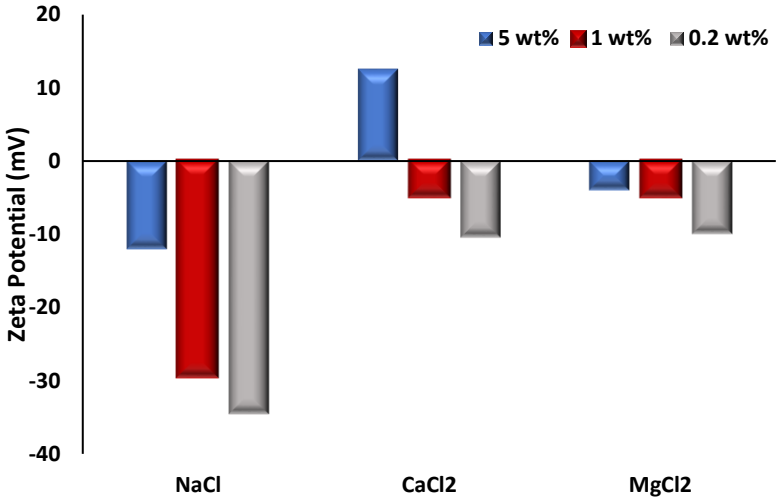

Figure 2.3 Monovalent & divalent ions effect on ζ-potential.[64]

2.2.4 Injection Rate

Water injection in petroleum and geothermal reservoirs may cause in-situ fines detachment from the rock surface under the shearing effect of injection fluid. Particularly in reservoirs with weak cementation, the unequal torques may cause pore blockage and reduce formation permeability.[68] Adhesion and hydrodynamic forces produce torques on fine particles that are attached to the rock surface. The adhesion forces between particles and the rock surface include electrostatic and gravity forces. For injection at low rates and below the critical rate, the effect of the electric double-layer repulsion force is more dominant to initiate fines migration. On the other hand, at higher rates, hydrodynamic force plays a significant role in detaching the fines from the rock surface. The electrostatic forces include van der Waals attraction and electric double-layer repulsion force. The flow rate of injection fluid controls the hydrodynamic forces, while the particle and permeating fluid densities control the gravity forces.

Ochi et al. looked into the impact of flow rates on fines migration and found that there is a threshold value above which permeability reduces due to the detachment of fine particles. They deduced from their observations that formation permeability was influenced by injection rate.[69] Bedrikovetsky et al. utilized the concept of maximum retention and successfully modeled it considering the effect of injection fluid velocity. Their model showed that after raising the fluid velocity to a threshold level, particles might be quickly dislodged from the sand surface. Conversely, lowering the velocity results in a

greater retention concentration up to a maximum owing to given hydrodynamic conditions.[70] Numerous imaging studies carried out on the synthetic core of glass beads have supported the rate-dependent fines detachment. The shearing force increases with flow rate, and particle detachment and mobilization may happen when hydrodynamic force is greater than adhesion forces.[71–73] Despite the imposed flow rate causing a hydrodynamic shearing exceeding the critical threshold, Torkzaban et al. determined that a single layer of attached fine particles is partly removed rather than fully. Due to the variability of pore structure, surface charge, and roughness, hydrodynamic and adhesion forces vary spatially.[74]

2.3 Sand-Fine-Brine System

The presence of fine particles adhering to sand grains within a saline environment gives rise to what is known as a sand-fine-brine (SFB) system. The detachment of fine particles from the sand grain surface is the initial step in the process of fines migration in sandstones. A comprehensive understanding of this detachment process is necessary to analyze conditions for migration and the resultant formation damage. Generally, two types of forces are responsible for the detachment and mobilization of fine particles. These forces are classified as colloidal forces and hydrodynamic forces. Colloidal forces are electrostatic in nature, and they are further divided into two types, which are London–van der Waals attraction forces and electrical double-layer repulsion forces between particles and surfaces. The hydrodynamic forces are mainly related to the flow of permeating fluid through porous media.

To mimic sandstone reservoirs with fine particles, synthetic fines, and spherical silica glass beads in brine have been used in numerous studies,[48,67,75–79] as shown in Figure 2.4. On the other hand, kaolinite in sandstone reservoirs has a platelet structure with a finite thickness (FT), while natural sand and glass beads both have infinite thicknesses (IT) as compared to fine particle size. Based on the aforementioned configuration of synthetic/ natural fines and sand/ glass beads, generally, there are different electrostatic energies for two different systems: the sphere-IT plate and the kaolinite platelet-IT plate.

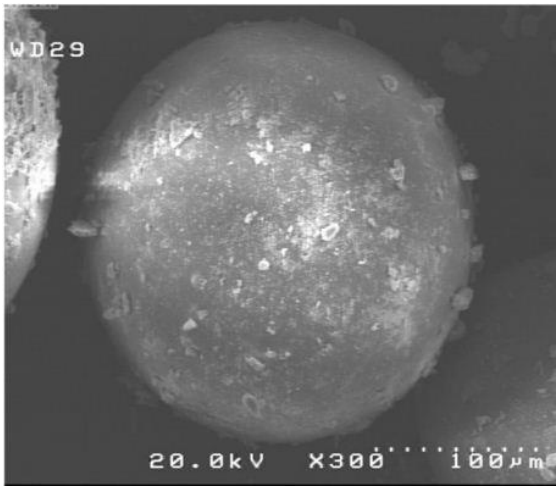

Figure 2.4 Adsorbed fines on the surface of a glass bead.[75]

An analysis of a single fine particle of presumably spherical shape on a sand grain surface had been performed to describe the conditions required for the detachment of fine from a flat surface.[80–83] Figure 2.5 describes the sphere-IT plate model designed to mimic a spherical fine particle attached to the pore/ rock grain through which a high salinity permeating liquid is flowing. However, Figure 2.6 demonstrates a kaolinite platelets-IT plate configuration, where small kaolinite platelets are present on a sandstone grain. Most of these platelets are in the form of clusters and can move together based on attraction forces between individual plates. Similar kaolinite platelet configurations have also been found in other sources.[84–89]

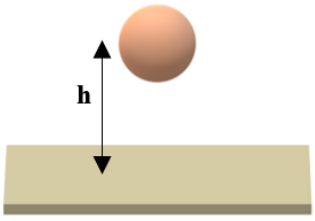

Figure 2.5 Spherical fine on the sand grain surface.

The separation distance (h) between a fine particle and the pore surface in Figure 2.5 is quite small (usually on the order of 10^{-1} nanometer, nm), and additionally, these fine particles are subjected to the hydrodynamic forces of the flowing liquid during production and injection processes. There are different energy contributions from colloidal and hydrodynamic forces, and the total energy of all interactions between a fine particle and

the pore/ grain surface must be determined precisely in the DLVO model to incorporate the effects of attraction and repulsion forces. If the net interaction energy of the system comes out to be positive, it means repulsion forces dominate the attraction forces; as a result, fines will be detached from the surface, and migration will start in the porous medium.

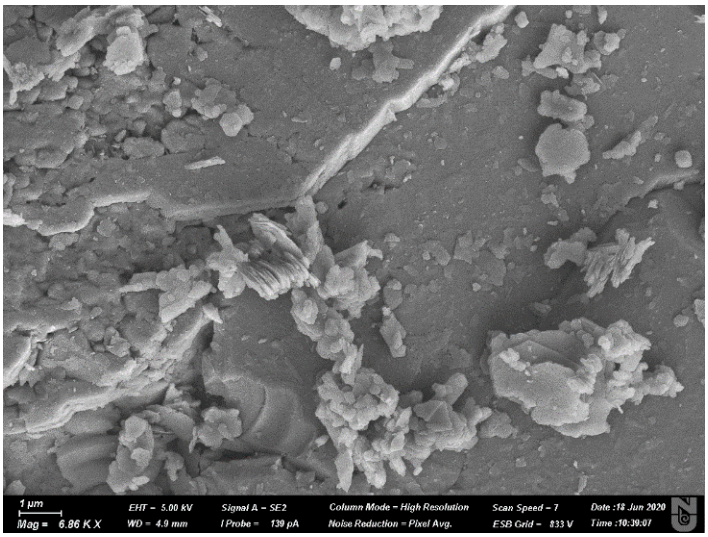

Figure 2.6 Kaolinite platelets-IT plate configuration.

During early research studies and to date, a single fine particle of spherical shape on a sand grain flat surface (sphere-plate model) has been extensively used for the calculation of DLVO interactions due to the simplicity of the approach.[36,63,75,76,78,79,90–93] A few researchers have utilized a plate-plate model for the quantification of interaction energies.[94,95] A single sphere model can be accurately used for synthetic fines and glass bead configurations, but when it comes to natural kaolinite and sand grain configurations, it can provide erroneous results because natural kaolinite has a platelet structure and must be modeled with a kaolinite platelets-IT plate model. In some studies during the last few years,[34,35,96–100] clustered fine particles' detachment and combined movement were assumed instead of a single fine particle model. Not long ago, Chequer et al.[63] used this new idea to show that the single-colloid single-surface system is not an accurate representation of colloidal behavior in porous media and significantly underestimates the critical flow rate of the fluid to initiate the fines migration. Experimental results were in close agreement with the clustered fines model.

2.4 DLVO Theory

The well-known DLVO theory was established by Derjaguin, Landau, Verwey, and Overbeek.[101–103] It describes the V_T of the system incorporating attraction and repulsion forces due to the van der Waals attraction potential (V_{LVW}), electric double layer potential (V_{EDL}), and the Born repulsion potential (V_{BR}), respectively. This theory assumes that the V_{LVW}, V_{EDL}, and V_{BR} potentials are independent of each other, and therefore can be added for the particle-plate system, using either a sphere-plate or plate-plate model configuration, to quantify total interaction energy at each interacting distance. The DLVO-based V_T of the system comprised of a fine particle and a pore surface is presented as Equation 2.3.

$$V_T = V_{LVw} + V_{EDL} + V_{BR} + V_{AB} \tag{2.3}$$

Generally, the DLVO theory provides good estimates for the surface-surface forces with a separation distance of around 5 nm, provided that all the important parameters, such as the particle size (a_p), ionic strength (I_s), Hamaker constant (A_H), and zeta potential (ζ), are accurately and precisely measured. The total energy of a specific system can range from positive (repulsion) to negative (attraction) depending on the individual contributions of the attraction and repulsion forces.

2.4.1 Application of DLVO Theory in the Petroleum Industry

The DLVO theory has been widely used in the petroleum industry to quantify surface forces between fines and sand grains during nanofluid injection scenarios, disjoining pressure estimation, and polymer and surfactant adsorption on the rock surface. Quantification of DLVO-based interactions has been reported to be in close agreement with experimental results. Habibi et al.[78] utilized NPs in synthetic cores to mitigate the fines migration problem, computed total interactions and found MgO NPs reduced the repulsion force between fines and the grain surface. Arab et al.[75] performed several experiments on glass beads to mitigate the fines migration issue, accompanied by low salinity flooding. They used five different types of nanoparticles to control fines migration and found ZnO and γ-Al_2O_3 NPs were the best at this task. In addition to experimental results, they also measured the zeta potentials of the system before and after the application of NFs and applied a DLVO sphere-IT plate model to calculate interactive energy. The total energy

was attractive after the application of NPs as compared to the non-treated case. Arab et al.[76] performed experiments using SiO_2 and MgO NPs in pre-flush mode and found that 0.03% MgO NPs performed the best among all scenarios. They confirmed their experimental findings with the DLVO theory by calculating the total interaction potential between the rock and fine particles. Assef et al.[67] demonstrated their work to mitigate colloidal particle movement in porous media by using MgO NPs and 97% retention of fines was observed. They utilized the extended DLVO (X-DLVO) theory by incorporating the effect of acid-base energy and neglecting the hydrodynamic forces and quantified the total interaction energy of the system. Zou et al.[104] applied the X-DLVO theory to investigate the adsorption of anionic polyacrylamide onto coal and kaolinite particles. Based on the results, they observed that the V_T between kaolinite and coal particles was repulsive after the adsorption of polymer on coal particles, which proves the effectiveness of the mechanism of coal purification.

2.5 Quantification of Interaction Energies

2.5.1 The London van Der Waals (V_{LVW}) Interaction Energy

In particle physics, there exists an attraction force between similar particles/plates when they are infinitesimally close to each other. A German-American physicist, Fritz London, published the first satisfactory microscopic theory of dipole-dipole dispersion forces.[105] This force is a distance-dependent force between molecules, atoms, and particles and does not have any association with any type of ionic or covalent bonds. It decays slowly and acts at a distance of less than 10 nm. The main cause of this electrostatic force is the presence of permanent and oscillating dipoles of atoms.[17] These forces are weak chemical forces, but still, play a critical role when colloidal particles are infinitesimally close to each other in a solution. Based on the sphere-IT plate model, London-van der Waals energy (V_{LVW}) is presented in two forms, in Equation 2.4[81] and Equation 2.5.[106]

$$V_{LVW} = -\frac{A_H a_p}{12h} \tag{2.4}$$

$$V_{LVW} = -\frac{A_H}{6}\left[\frac{2(1+H)}{H(2+H)} + \ln\left(\frac{H}{2+H}\right)\right] \tag{2.5}$$

Chequer et al.[63] presented a new model based on the clustered fines sphere-IT plate model, as shown in Equation 2.6.

$$V_{LVW} = -n\frac{A_H}{6\sqrt{2}a_p}\left(\frac{a_p}{h}\right)^{\frac{5}{2}} \tag{2.6}$$

On the other hand, a separate model for kaolinite platelets-IT-plate configuration has been presented by Gregory et al.[81] as shown in Equation 2.7.

$$V_{LVW} = -\frac{A_H}{12\pi h^2} \tag{2.7}$$

The negative sign of V_{LVW} demonstrates the attractive nature of this potential.

2.5.2 Electric Double Layer (V_{EDL}) Interaction Energy

When charged colloidal particles (fines) are immersed in an electrolyte solution of specific ionic strength, mobile ions from the electrolyte solution form an ionic film around the particles.[103] Based on the positive or negative charge of a particle, oppositely charged ions from the surrounding electrolyte solution are attracted and form an ionic layer over the charged particle, called a compact layer (stern layer), which is moved with the particle. The excess charge on the compact layer is balanced by the oppositely charged ions from the electrolyte solution forming another layer, which is called the diffuse layer (slipping plane). In the diffuse layer, ions are not tightly bound to each other and are free to move to and from the electrolyte solution. These two layers are electrostatic, and their combined effect is called the electric double layer (EDL), as shown in Figure 2.7.[107]

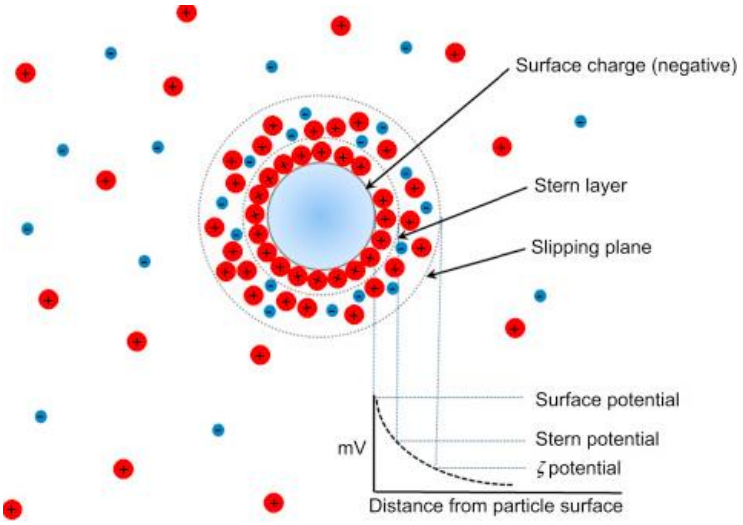

Figure 2.7 Compact and diffuse electric double layers and corresponding zeta potential.[107]

The potential difference between these two layers is called zeta potential and is denoted by 'ζ'. Zeta potential provides the closest surface potential estimate and is used in the quantification of the electric double-layer interaction energy. Zeta potential is not directly measured and is obtained by applying an electric field across the dispersion: this process is called electrophoresis.[108,109] Particles within the dispersion with a specific zeta potential value move towards the electrode of opposite charge with a velocity proportional to the magnitude of the zeta potential. At lower ion strength, such as in the low salinity injection condition, EDLs that have already formed around the sand grain surface and the fine particles, expand and overlap, which leads to a repulsion interaction energy (V_{EDL}). High repulsion force may detach the fine particles from the sand grain surface. The force is stronger at a lower solution salinity.

Regarding the formulation of V_{EDL}, the simplest case of sphere-plate geometry is used as shown in Figure 2.5. For the boundary conditions, the rock and fine particle surfaces both may have a constant surface potential or constant charge, or one of the surfaces may maintain its charge density constant while the other surface possesses a constant potential resulting in a mixed case. Generally, fines migration can be modeled with a constant potential case because zeta potential is easy to measure as compared to surface charge. V_{EDL} can be calculated by different formulae, such as Equation 2.8, Equation 2.9[110], or Equation 2.10[82], for the sphere-IT plate model.

$$V_{EDL} = \left(\frac{\epsilon a_p}{4}\right)\left[2\Psi_1\Psi_2 \ln\left(\frac{1+e^{-kh}}{1-e^{-kh}}\right) + \left({\Psi_1}^2 + {\Psi_2}^2\right)\ln(1-e^{-2kh})\right] \quad (2.8)$$

$$V_{EDL} = \left(\frac{\epsilon a_p}{4}\right)\left[2\zeta^2 \ln\left(\frac{1+e^{-kh}}{1-e^{-kh}}\right) + (2\zeta^2)\ln(1-e^{-2kh})\right] \quad (2.9)$$

$$V_{EDL} = 2\pi\varepsilon_m\varepsilon_0 a_p \zeta^2 . ln(1+e^{\frac{-h}{k^{-1}}}) \quad (2.10)$$

Equation 2.6 is valid for potentials less than 60 mV when the double layer thickness is less than the fine particle size, which is true in most scenarios of fines migration in sandstone porous media. Ψ_1 and Ψ_2 are the surface and compact layer potentials, respectively, and can be replaced by the measured value of the zeta potential to develop Equation 2.7. Chequer et al.[63] presented a new model to calculate V_{EDL} based on the clustered fines sphere-IT plate model, as shown in Equation 2.11.

$$V_{EDL} = -n160.4\varepsilon_m\varepsilon_{0k}(ka_p)^2\left(\frac{k_B T}{ze}\right)^2 \gamma_s\gamma_g e^{-kh} \quad (2.11)$$

For V_{EDL} calculations based on the kaolinite platelets-IT-plate model, Gregory[111] presented a different model as shown in Equation 2.12.

$$V_{EDL} = \frac{64 n_\infty k_B T}{k}\gamma_s\gamma_g e^{-kh} \quad (2.12)$$

2.5.3 Born Repulsion (V_{BR}) Interaction Energy

In a colloidal system, when particles approach and are about to contact each other, a short-range repulsion potential called the Born repulsion potential (V_{BR}) is generated because their electron clouds overlap. This potential is quite sensitive to the structure of surfaces in contact and permeating liquid. Formulations to quantify the Born repulsion potential for the previously described sphere-IT-plate system have been presented by Ruckenstein et al. and Schumacher et al.[112,113] in Equation 2.13 and Mahmood et al.[83] in Equation 2.14.

$$V_{BR} = \frac{A_H}{7560}\left(\frac{\sigma}{a_p}\right)\left[\frac{8+H}{(2+H)^7} + \frac{6-H}{H^7}\right] \quad (2.13)$$

$$V_{BR} = \frac{A_H a_p \sigma^6}{1260\, h^7} \quad (2.14)$$

For clustered fines movement in the porous medium, Chequer et al.[63] presented another model to calculate V_{BR}, as shown in Equation 2.15.

$$V_{BR} = -n\frac{A_H {a_p}^2 \sigma^6}{45\ h^9} \tag{2.15}$$

A separate model for the natural kaolinite platelets-IT-plate configuration has been presented by Mahmood et al.[83] as Equation 2.16.

$$V_{BR} = \frac{A_H \sigma^6}{360\pi h^8} \tag{2.16}$$

To compute Born repulsion accurately for the fines-rock-fluids system configuration, A_H and σ (atomic collision diameter, nm) must be known precisely. An average value for 'σ' used in the calculation of V_{BR} is around 0.5 nm. Generally, V_{BR} has a very small impact on the V_T and can be neglected in comparison to other electrostatic potentials (V_{LVW} and V_{EDL}) if the separation distance is greater than 1 nm.

2.5.4 Acid-Base (V_{AB}) Interaction Energy

At the liquid-solid interface, the acid-base reaction produces an interactive potential, which is a short-range potential called acid-base potential (V_{AB}). It can be either negative or positive, depending on whether the two phases are attracted to each other or repel each other. A sand-fine-brine system is expected to have a weak acid-base interaction; therefore, it can be neglected for fines migration modeling in porous media. For a solid surface and liquid system, Equation 2.17 is used to compute acid-base potential.[114]

$$E_{AB} = \pm E^o_{AB}\ Exp\left[-\left(\frac{h-h_o}{\lambda}\right)\right] \tag{2.17}$$

2.5.5 Assumptions for DLVO Model

The following assumptions are considered for DLVO modeling:

i. The fine particles are all the same size.
ii. The sand grains and fine particles have the same separation distance (h).
iii. The surface potential remains constant everywhere on sand grains.

iv. The Hamaker constant and the van der Waals attraction are unaffected by ionic strength.
v. Particles agglomerate when their spacing is less than the Debye length.

The DLVO model is based on certain assumptions; however, not all of the assumptions are met in every case, and thus not all of the fine particles are released and migrated. Because the size of the fine particles in the rock sample can never be the same, therefore, average fine particle size is used in the modeling to reduce the effect of fine particle size variation. Similarly, the Zetasizer measures the surface potential of several sand particles in the dispersion and provides an average value of zeta potential for a defined sand-fine-brine system. However, when measuring zeta potential, care must be taken because incorrect measurement of zeta potential will lead to incorrect calculations of electric double layer and total interaction potentials.

2.6 Interactive Parameters for the SFB System

Van der Waals particle-particle attraction is produced when particles/ molecules come close to each other in a medium. The Hamaker constant (A_H) is a coefficient that relates this interactive energy among particles, whereas zeta potential (ζ) is a measure of the surface charge of the particles and an indicator of the increase and decrease of the repulsion force. The following section discusses these parameters in detail.

2.6.1 Hamaker Constant (A_H)

Hamaker constant is dependent on the integrated system of the fine particle, its shape, pore surface, aqueous medium type and salinity, and crude oil properties.[82] The Hamaker constant is determined experimentally with great caution based on the specific system configuration. The typical values for A_H are found in the range of 10^{-21} to 10^{-19} J. These experimental values are in close agreement with the theoretical calculations of Israelachvili.[82,115] Based on the specific system configuration, the Hamaker constant is determined experimentally with extreme caution. Using the Hamaker constants from Table 2.2 and Equation 2.18[116], an integrated Hamaker constant of 1.52×10^{-20} J for the kaolinite-sand-brine system was calculated and used in DLVO modeling.

$$A_H = (A_{11}^{0.5} - A_{33}^{0.5})(A_{22}^{0.5} - A_{33}^{0.5}) \quad (2.18)$$

Table 2.2 Hamaker constants for fines, sand, and brine.[117]

Materials	*Hamaker constants, J*
Kaolinite, A_{11}	1.5×10^{-20}
Water/ brine, A_{22}	4.38×10^{-20}
Sand, A_{33}	8.8×10^{-20}

Equation 2.19 can also be used to calculate this constant using experimental data.

$$A_H = \frac{3}{4}k_BT\left(\frac{\varepsilon_1-\varepsilon_3}{\varepsilon_1+\varepsilon_3}\right)\left(\frac{\varepsilon_2-\varepsilon_3}{\varepsilon_2+\varepsilon_3}\right) + \frac{3h_p\nu_e}{8\sqrt{2}}\frac{(\eta_1^2-\eta_3^2)(\eta_1^2-\eta_3^2)}{(\eta_1^2+\eta_3^2)^{1/2}(\eta_2^2+\eta_3^2)^{1/2}\{(\eta_1^2+\eta_3^2)^{1/2}+(\eta_2^2+\eta_3^2)^{1/2}\}} \quad (2.19)$$

'ε' is the static dielectric constant, η is a refractive index, and the subscripts 1, 2, and 3 refer to particles, grains, and water/ brine, respectively. h_p is the Planck constant (6.62×10^{-34} J-sec), and ν_e is a constant value of electronic adsorption frequency equal to 3×10^{-15} s^{-1}. Table 2.3 presents studies where Hamaker constants were calculated and a few studies where experimental approaches have been used to measure A_H based on the system's actual configuration.[63,94,118,119] A high Hamaker constant leads to more attraction, whereas its low value is related to reduced attraction. Also, particle deposition onto a rock's surface is affected by the Hamaker constant of the interactive system. Elimelech et al.[120] found that at low salinity, the range of EDL is much higher than that of van der Waals attraction, and the rate of particle deposition is mainly controlled by double-layer repulsion energy. However, at high salinity, the van der Waals attraction force is more effective, and as a result, the rate of particle deposition is controlled by A_H.

Table 2.3 Hamaker Constant Data.

Author	*Year*	*Base Liquid*	*pH*	*T (°C)*	*System*	*A_H (J)*	*Experimental/ Theoretical*
El-Monier et al.[94]	2011	Distilled Water	12	149	Kaolinite-Quartz	1.61×10^{-20}	Experimental
Habibi et al.[78]	2012	Water	7	25	Glass Beads-water	6×10^{-21}	Theoretical
El Badawy et al.[118]	2012	0.03M NaCl	7	--	Metallic NPs	6.04×10^{-20}	Experimental
Arab et al.[75]	2013	Water	7	25	Glass Beads-water	6×10^{-21}	Theoretical

Arab et al.[75]	2013	0.03M NaCl	6.9	25	Glass Beads-brine	1×10^{-21}	Theoretical
Arab et al.[76]	2014	Water	7	25	Glass Beads-water	6×10^{-21}	Theoretical
Habibi et al.[90]	2014	0.03M NaCl	6.5-7	25	Sand-NaCl	1×10^{-20}	Theoretical
Xie et al.[28]	2014	0.2 wt% NaCl	8.1	65	Oil/silica in water	8×10^{-21}	Theoretical
Yang et al.[91]	2016	Water	--	25	kaolinite and quartz	2×10^{-20}	Theoretical
Mahani et al.[24]	2017	0.035M diluted Sea Water	7	25	Limestone-brine	1×10^{-19}	Theoretical
Hasannejad et al.[79]	2017	0.3M NaCl	7	25	Glass Beads-brine	1×10^{-20}	Theoretical
Xie et al.[121]	2018	NaCl, $MgCl_2$ and $CaCl_2$	4-10	25	Shale-oil	0.81×10^{-20}	Theoretical
Huang et al.[92]	2018	2 wt% KCl	7	25	Coal-brine	4.62×10^{-20}	Theoretical
Sanaei et al.[95]	2019	0.01M NaCl	7	25	Carbonate-brine	1.3×10^{-20}	Theoretical
Chequer et al.[63]	2019	0.6M NaCl	7	25	Kaolinite-Sand	1.49×10^{-20}	Experimental
Takeya et al.[26]	2020	0.1M ALSW	7	25	Calcite-brine	6.6×10^{-21}	Theoretical
Tangparitkul et al.[36]	2020	0.0005M NaCl Brine	--	--	Clay-sand	2×10^{-21}	Theoretical
Gomez-Flores et al.[93]	2020	0.001M NaCl	7	25	Silica-Brine	3.91×10^{-21}	Theoretical
Peng et al.[119]	2020	0.007M SDS and 0.0005M NaCl	--	25	Surfactant-water	5.2×10^{-20}	Experimental

2.6.2 Zeta Potential (ζ)

Zeta potential is an important indicator of surface charge and is used for the quantification of the electrostatic repulsion energy between dispersed fines and sand grains. It is the potential difference between the surfaces due to the electrical difference between a particle surface and points away from the particle in the fluid at the boundary of the slipping plane,[122,123] as shown in Figure 5. This potential is also known as electro-kinetic potential in colloidal dispersions. It is worth mentioning here that the measured zeta potential of clay fine particles is negative and is an important parameter that provides information about the charge on the particle surface, colloidal system stability in an ionic environment, electrostatic forces between particles and the rock surface, and interaction energy between NPs and formation fines in porous media. Zeta potential is an input parameter in the calculation of the EDL repulsion force and must be determined experimentally with great accuracy. It is usually measured with a Zetasizer, which uses the electrophoretic mobility (EFM) concept based on the Helmholtz-Smoluchowski equation

as shown in Equation 2.20.

$$\zeta = \frac{U_E \, 3 \, \eta}{2 \, \varepsilon \, F(ka)} \tag{2.20}$$

Table 2.4 and Table 2.5 present the zeta potential data collected from several previously published research articles that show the widespread use of this parameter. It is evident from the data that in all the studies, the zeta potential of the system has been determined with the help of the Zetasizer/ zeta potential analyzer, which is a high-technology and expensive apparatus being used worldwide. It measures the electrophoretic mobility and automatically converts it to provide the direct zeta potential value of the system under study. No comprehensive correlation is available to directly calculate zeta potential as a function of system configuration (sand, glass beads, fines, kaolinite, calcite, etc.), salinity, viscosity, pH, and temperature.

Table 2.4 Zeta potential data in the presence of NPs.

Author	*Year*	*NPs Type*	*NPs Size (nm)*	*NPs Concentration*	*Base Liquid*	*pH*	*T (°C)*	*Environment*	*ζ - Before (mV)*	*ζ - After (mV)*	*Apparatus/ Method*
Rouxel et al.[124]	2011	Al_2O_3	13	0.03 wt%	DI Water	7.2	25	Water	--	34	Zetasizer
Priya et al.[125]	2012	CuO	40–60	0.016 vol%	DI Water	12	28–55	Water	--	30	Zetasizer
El Badawy et al.[118]	2012	H_2-Ag	13	3 vol%	0.03 M NaCl	7	--	Saline	--	-22	Zetasizer
Suganthi et al.[126]	2012	ZnO	30–45	1 vol%	DI Water	--	25	Water	--	49.9	Zetasizer
Habibi et al.[78]	2012	MgO	63	--	DI Water	7	40	Glass Beads	--	-5.68	Zetasizer
			63	0.03 wt%	0.3 M NaCl	7	25	Berea sand	--	-7	Zetasizer
			63	0.1 wt%	DI Water	7	25	Glass Beads	-34	12.8	Zetasizer
Ahmadi et al.[77]	2013	MgO	63	0.1 wt%	DI Water	7	25	Glass Beads	-44.4	-11	Zetasizer
		SiO_2	48	0.1 wt%	DI Water	7	25	Glass Beads	--	-22.5	Zetasizer
		Al_2O_3	43	0.1 wt%	DI Water	7	25	Glass Beads	--	-28.4	Zetasizer
Arab et al.[75]	2013	ZnO	30	0.03 wt%	DI Water	7	25	Glass Beads	-44	1.57	Zetasizer
		γ-Al_2O_3	20	0.03 wt%	DI Water	7	25	Glass Beads	-44	0.82	Zetasizer
Arab et al.[76]	2014	MgO	20	0.03 wt%	0.03 M NaCl	6.9	25	Glass Beads	-27.6	-5.7	Zetasizer
		MgO	20	0.03 wt%	DI Water	7	25	Glass Beads	-44	-1	Zetasizer
Assef et al.[67]	2014	MgO	20	0.0075 wt%	0.02 NaCl	7	25	Glass Beads	-24.3	6.9	Zetasizer
Bayat et al.[127]	2015	Al_2O_3	40	0.005 wt%	DI Water	6.4	26	Water	--	19.1	ζ analyzer
		TiO_2	30	0.005 wt%	DI Water	6.4	26	Water	--	9.1	ζ analyzer
		SiO_2	20	0.005 wt%	DI Water	6.4	26	Water	--	-28.1	ζ analyzer

Alomair A. et al.[128]	2015	TiO_2	50	0.1 wt%	30000 ppm Brine	5.9	40	Berea sand	--	-13.2	Zetasizer
		SiO_2	15	0.1 wt%	30000 ppm Brine	5.9	40	Berea sand	--	-28.3	Zetasizer
		Al_2O_3	40	0.1 wt%	30000 ppm Brine	5.9	40	Berea sand	--	25.3	Zetasizer
		NiO	50	0.1 wt%	30000 ppm Brine	5.9	40	Berea sand	--	-23.4	Zetasizer
Sabiha et al.[129]	2016	SWCNT	2,500 L	0.1 Vol%	DI Water	--	25	Water	--	-53.1	Zetasizer
M. Adil et al.[130]	2016	ZnO	55	0.1 wt%	30000 ppm NaCl	9	95	Saline	--	-20	Zetasizer
Hasannejad et al.[79]	2017	SiO_2	145	0.1 wt%	0.3 M NaCl	7	25	Glass Beads	-28	-25	Zetasizer
Lee et al.[131]	2017	SiO_2	37	6.72 wt%	4.5 M NaCl/ CaCl2	8	25	Saline	--	-24	Zetasizer
Al-Anssari et al.[132]	2017	SiO_2	10	0.1 wt%	1 wt% NaCl	6.3	--	Saline	-40	-5	Zetasizer
Abdelfatah et al.[133]	2017	SiO_2	10	--	--	6	25	--	--	-22	--
Skoglund et al.[134]	2017	Ag NPs	9	--	DI Water	--	25	Water	--	-44	Zetasizer
Choudhary et al.[135]	2017	γ-Al_2O_3	20	0.1 wt%	DI Water	7.6	--	Water	--	36.7	Zetasizer
Upendar et al.[136]	2018	α-Fe_2O_3	20	0.05 wt%	0.001 M NaCl	6.5	25	Saline	--	9.7	EFM
Kuang et al.[137]	2018	Al_2O_3	50	0.1 wt%	0.001 M NaCl	7	25	Saline	--	39	ζ analyzer
Mansouri et al.[48]	2019	SiO_2	15	0.1 wt%	0.03 M NaCl	5.9	25	Glass Beads	-25	-7.5	Zetasizer
Ma et al.[138]	2019	SiO_2-g-SPMA	100	0.5 wt%	5.4 M NaCl+CaCl2	11	170	Saline	--	54	Zetasizer
Siddiqui et al.[139,140]	2019	Cu-Al_2O_3	270	0.01 wt%	DI Water	7	23	Water	--	48.15	ζ analyzer
Aramendiz et al.[141]	2019	SiO_2	20	0.75 wt%	DI Water	9.5	25	Water base mud	--	-34.66	ζ analyzer
Kumar et al.[142]	2020	SiO_2-TiO_2	15, 20	0.4, 0.05 wt%	DI Water	7	90	Water	-45.4	-34.1	Zetasizer
Wang et al.[143]	2020	CNCs	70	0.25 wt%	0.175 M NaCl	7	21	Saline	--	-60	Zetasizer

Table 2.5 Zeta potential data without NPs.

Author	*Year*	*Base Liquid*	*Salinity*	*pH*	*T (°C)*	*Environment*	*ζ (mV)*	*Apparatus/ Method*
Yousef et al.[144]	2012	Seawater	600 ppm	7-8	60	Carbonate	-13	Zetasizer
Nasralla et al.[145]	2012	NaCl Brine	0.2 wt%	7.7	25	Berea SS	-35	Phase-analysis light-scattering PALS
Hussain et al.[34]	2013	NaCl Brine	0.5 M	--	25	Sand	-20	--
Chen et al.[146]	2014	Formation water	14000 ppm	8	25	Limestone	-15	Phase-analysis light-scattering PALS
Xie et al.[28]	2014	0.2 wt% NaCl	0.2 wt%	8.1	65	Sandstone	-23.7	Zetasizer
Xie et al.[64]	2016	NaCl Brine	0.2 wt%	--	25	Sandstone	-33	--
Yao et al.[147]	2016	Distilled water	0	9.2	25	Quartz	-23	Zetasizer
Mahani et al.[24]	2017	Diluted seawater	0.035 M	7	25	Limestone	-11	Zetasizer
Huang et al.[92]	2018	KCl	2 wt%	7	25	Coal-brine	-12.61	Micro-electrophoresis
Sanaei et al.[95]	2019	NaCl Brine	0.01 M	7	25	Carbonate	-50	--
Chequer et al.[63]	2019	NaCl Brine	0.6 M	7	25	Sand	-20	Zetasizer
Takeya et al.[23]	2019	NaCl Brine	0.7 M	7.2	50	Crude oil	-23	Zeta-potential analyzer
Alghamdi et al.[148]	2020	Smart Water	5761 ppm	7.4	--	Carbonate	-8	Smoluchowski equation
Ruan et al.[149]	2020	0.1 M KCl	0.1 M	7	30	Clay-brine	4.9	Zetasizer
Takeya et al.[26]	2020	ALSW	0.1 M	7	25	Calcite-brine	-3.72	Zetasizer
Tangparitkul et al.[36]	2020	NaCl Brine	0.000513 M	--	--	Clay-sand	-50	Zetasizer
Gomez-Flores et al.[93]	2020	NaCl Brine	0.001 M	7	25	Silica-Brine	-39	--
Peng et al.[119]	2020	7 mM SDS and 0.5m M NaCl Brine	--	--	25	Surfactant-water	-80	--

2.7 Description of a DLVO Model

For the sand-fine-brine system, Equation 2.3 contains attraction and repulsion potentials, which are calculated using important constants presented in Table 2.6 with given values used in the DLVO modeling. The majority of them are constants that are used as is it, but some important parameters such as fine particle size, system salinity, zeta potential, and Hamaker constant are accurately measured based on a given sand-fine-brine system. The precision of these measured parameters determines the accuracy of a DLVO model prediction. When all the critical parameters are precisely measured, the DLVO theory accurately predicts the surface-to-surface interaction for a separation distance of roughly 5 nm and below. Based on the contributions from repulsion and attraction potentials, the V_T can range from a negative to a positive value corresponding to either attractive or repulsive, respectively. For example, a simple description of a DLVO model with attraction and repulsion forces has been presented and the overall interaction energy of the SFB system is repulsive (positive) as shown in Figure 2.8, resulting in an energy barrier. In comparison to the neutral condition (V_T = 0), the height of this barrier corresponds to the high value of repulsion potential in the total interaction potential. The surface charge of the sand grains is affected by changes in the salinity or pH of the injected water, which can increase or decrease the energy barrier.

Table 2.6 Constants used in the DLVO model.

Parameter	*Symbol*	*Value*
Fluid temperature	T	297.15 K
Hamaker constant	A_H	3×10^{-21} J
Boltzmann constant	k_B	1.38×10^{-23} JK^{-1}
Dielectric constant of water	ε_m	80
Permittivity of vacuum	ε_o	8.85×10^{-12} $C^2J^{-1}m^{-1}$
electron charge	e	1.6×10^{-19} C
Avogadro's Number	N_A	$6.02\times10^{+23}$ $mole^{-1}$
Atomic collision diameter	σ	5×10^{-10} m
pH of solution	pH	6.5-7.5
Pi	π	3.1416

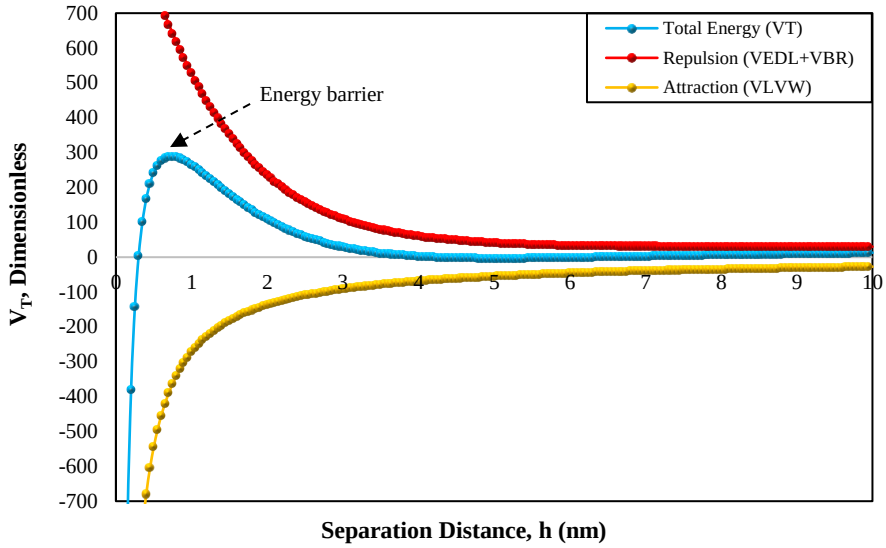

Figure 2.8 A DLVO model with attraction and repulsion forces.

2.8 Fine Migration Control by Nanoparticles

Various techniques have been developed and utilized to overcome the aforementioned problems and enhance oil recovery economically. Some examples include the utilization of clay stabilizer, matrix acidizing treatment,[150,151] adjusting the salinity, tuning the ionic composition, and changing the pH of the injected water.[33,152,153] The application of nanoparticles is one of the emerging technologies used to fix the fines migration problem. NPs are extremely small particles; their size can vary between 1–100 nm, and they have a high surface-area-to-volume ratio because of their small size. NPs can change the surface properties of the materials to which they are adsorbed. A single type of NPs (in the form of NFs), a combination of more than one type of NP (hybrid case), and nanoparticles and surfactants in combination are being used to reduce formation damage and enhance oil production.[48,75,128,139,142,154] NPs alter surface forces and potential as they are adsorbed on the rock. Several types of NPs with different chemical natures and distinct properties have been used to control fines migration; they include magnesium oxide (MgO),[67,76,154,155] silicon oxide (SiO_2),[48,77], and aluminum oxide (Al_2O_3).[75,77,78,156] The adsorption of nanoparticles has been the subject of investigation in numerous studies, and findings indicate that 30-45% of injected nanoparticles become adsorbed onto the sandstone surface.[133,157–160] This process leads to a change in the surface potential, which has been characterized by zeta-potential measurements conducted by various researchers.

A shift towards a more positive zeta-potential has been reported, which suggests that fine particles are more likely to remain attached to the sandstone surface, thereby minimizing the problem of fine particle release and migration.[66,126,146,161–164]

NPs can shift the PZC by changing the surface forces, so they can be used to control the repulsion force and the detachment of fines. The PZC for SiO_2 NPs is around pH = 2.5–3. For alumina, it lies between 7.5–9, and for MgO, it is around 12–13.[165] Hence, for highly alkaline conditions, the application of MgO NPs prevents fines detachment even at high pH values. Data concerning various nanoparticles used in different studies, which were performed for fines fixation, wettability modification, interfacial tension (IFT) reduction, drilling mud preparation, and stable nanofluids formulation, have been collected, and the results have been presented in Figure 2.9.

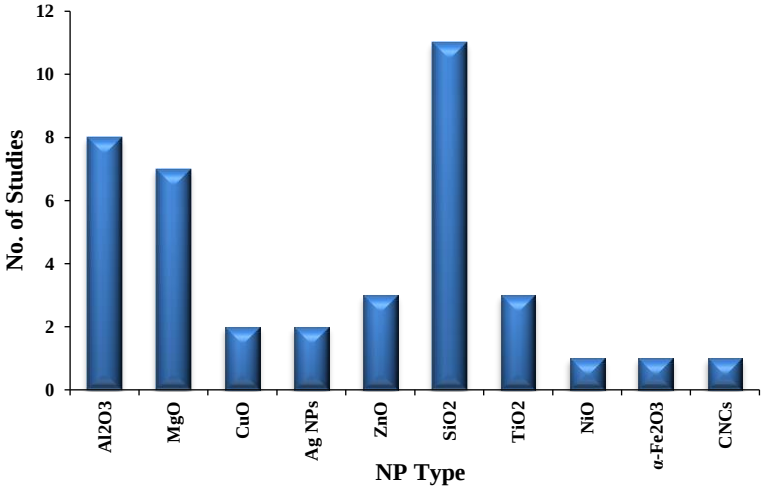

Figure 2.9 Different NP utilization in various studies.

It is observed that the maximum number of studies are performed using SiO_2 NPs because of their high stability, low toxicity, resistance to pH changes, and easy availability.[166] MgO and Al_2O_3 NPs are next on the list and have been utilized in several studies to mitigate fines release, the migration issue, and IFT reduction, respectively. Nanoparticles are used to overcome the fines migration problem in sandstone reservoirs by changing the surface forces, which can be observed by an alteration in zeta potential values before and after the adsorption of NPs onto rock/ grain surfaces. Figure 2.9 presents the zeta potential values of glass beads before and after the application of different NPs in low salinity conditions.[48,67,75–79,132,142] Figure 2.9 shows that MgO NPs are the best at changing

the surface energy and increasing zeta potential. In a few research studies, ZnO, TiO_2, and NiO NPs, and combinations of more than one NP, have been used in the form of nanofluids (NFs). Future research will benefit most from using different types of single and hybrid NFs.

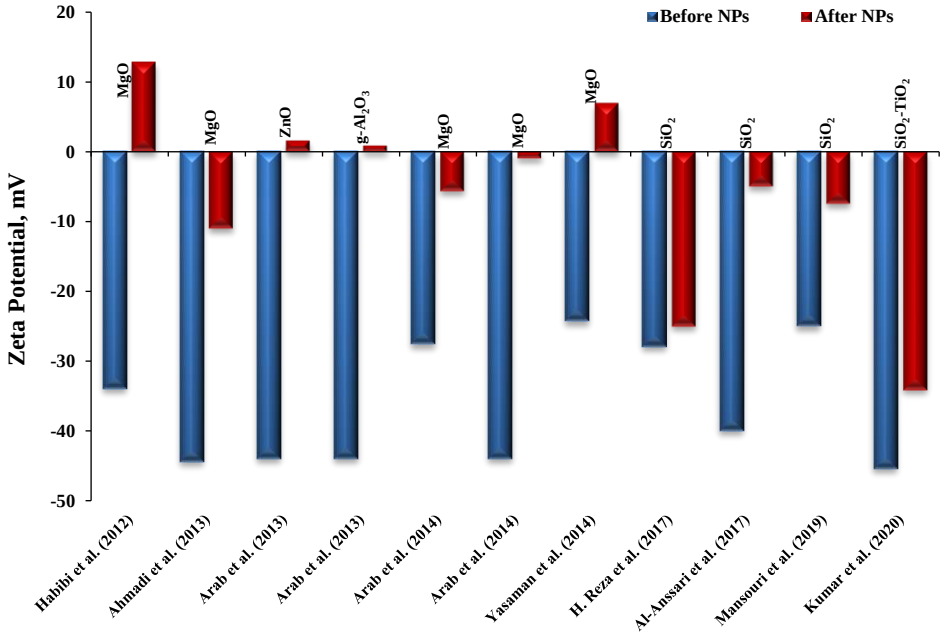

Figure 2.10 Change in zeta potential by the application of NPs.

In an experimental study, Assef et al.[67] used MgO NPs to mitigate the adverse effects of fines migration that were noticed under low salinity flow conditions (0.02M NaCl). They observed experimentally that the application of only 0.0075 wt% MgO NPs retained around 97% of in-situ fine particles even in highly alkaline conditions of pH = 9.2. Retention of fine particles was attributed to increasing attraction forces between fines and glass beads in the presence of MgO NPs.

A comprehensive literature review is presented in this chapter, which sheds light on the phenomenon of fines migration in sandstone reservoirs, and the different factors that contribute to it. It is well-documented that fines migration can have a detrimental impact on rock permeability, and the initiation of fines migration is determined by various forces such as attraction, repulsion, gravitational, and hydrodynamic forces. These forces are themselves influenced by factors such as brine salinity, ionic strength, pH, and the rate of injection or production in the SFB system. Furthermore, injection brines typically contain

both monovalent and divalent ions. Notably, even a small quantity of divalent ions can have a significant impact on reducing the CSC of the injection brine. This is because divalent ions have a greater charge density than monovalent ions, which makes them more effective in reducing the repulsion forces between fine particles and sand grains. As a result, the presence of divalent ions in the injection brine can lead to a lower CSC, which can in turn reduce the risk of fines migration. In order to control fines migration in sandstone formations, the literature review highlights the extensive use of nanoparticles as one of the most effective strategies. Nanoparticles can alter the surface potential of the rock, thereby reducing the repulsion force between fines and sand grains, and ultimately, suppressing the expansion of EDLs around sand grains and fine particles.

In the upcoming chapters, the DLVO modeling approach has been systematically employed to predict critical parameters such as the CSCs for both monovalent and divalent brines, as well as the combination brines. Accurately defining the SFB system under consideration is crucial for applying the DLVO model and predicting the initiation conditions for fines migration during various EOR processes such as waterflooding, alkaline flooding, and high-rate injection/production scenarios. Moreover, the effectiveness of nanotechnology in controlling fines migration has been incorporated into the DLVO model, which provides a comprehensive approach to assess the impact of nanoparticles on controlling fines migration.

CHAPTER 3: Application of DLVO Model for Low-Rate Fluid Flow

The well-known DLVO theory was established by Derjaguin, Landau, Verwey, and Overbeek. It describes the van der Waals attraction potential (V_{LVW}), electric double layer potential (V_{EDL}), and the Born repulsion potential (V_{BR}) in the system, incorporating both attraction and repulsion potentials. This theory assumes that the V_{LVW}, V_{EDL}, and V_{BR} potentials are independent of each other. Therefore, for the particle-plate system, these potentials can be combined to quantify the total interaction energy at each interacting distance. This chapter is based on the results published in the referenced articles[b,c,d].

3.1 Introduction

The migration of natural reservoir fines has been widely reported in previous studies as a cause of productivity and injectivity decline in sandstone petroleum reservoirs.[167–169] The fine particles attached to the rock coat the surface of the rock. As a result, the detachment of these particles from the rock surface does not increase rock permeability. However, the plugging of thin pores during fines migration blocks the flow paths, resulting in a significant decrease in permeability with a high-pressure drop in the SFB system. Fine particles are detached from the rock surface at a CSC, and their migration and plugging can cause severe formation damage.[17,34,36,37,170]

Fines may be released and migrate under specific conditions and can be predicted as a function of velocity, salinity, pH, the ionic strength of the injected brine, the concentration of in-situ fines, and temperature.[8,17,84] Fine particles are attached to the rock surface by electrostatic and gravitational forces. Because of the high charge density in the sand-fine-brine system, the electric double layers (EDLs) around fine and sand grains are contracted, keeping the fine particles in equilibrium in a high salinity formation water environment. However, when the system salinity drops due to the invasion of low-salinity water in any operation, both electric double layers expand, fine particles are detached due

[b] Muneer, R.; Hashmet, M. R.; Pourafshary, P. DLVO Modeling to Predict Critical Salt Concentration to Initiate Fines Migration Pre-and Post-Nanofluid Treatment in Sandstones. SPE J. 2022, 1–15.
[c] Muneer, R.; Hashmet, M. R.; Pourafshary, P. Application of DLVO Modeling to Study the Effect of Silica Nanofluid to Reduce Critical Salt Concentration in Sandstones. IOP Conf. Ser. Mater. Sci. Eng. 2021, 1186 (1), 12001.
[d] Muneer, R.; Hashmet, M. R.; Pourafshary, P. Predicting the Critical Salt Concentrations of Monovalent and Divalent Brines to Initiate Fines Migration Using DLVO Modeling. J. Mol. Liq. 2022, 352, 118690.

to high repulsion, and migration begins within the reservoir, even at a low flow rate. Hence, by altering the surface forces, fines can be released, make a suspension with the injection brine, develop a colloidal system in the porous media, move with the injected fluid, and block pore throats.[2,37]

Clay minerals, primarily kaolinite, illite, and chlorite, are the most widely distributed minerals that produce migrating fines.[5,171,172] However, unconsolidated sand or silica silt can easily be detached and mobilized, resulting in a significant loss of permeability.[11,47,48,173] An image of released and migrating kaolinite fines in the Berea sandstone core captured using scanning electron microscopy (SEM) is shown in Figure 3.1. Distilled water was injected into the core sample at a low rate, and it detached in-situ fines due to an increase in repulsion forces. Fine particles moved in the direction of flow and collected at the effluent. Thin and large kaolinite platelets are joined together by electrostatic attraction to form thick booklets. The kaolinite platelet can plug even larger pores after being detached from the sand surface.[174]

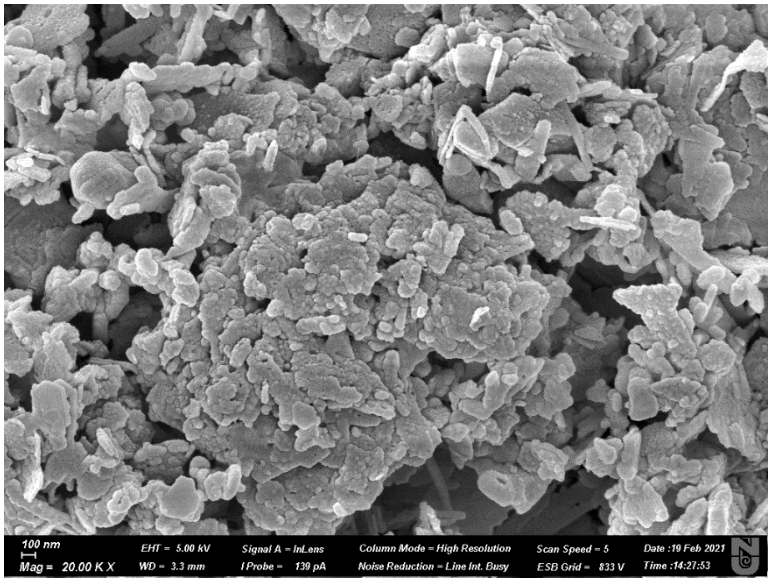

Figure 3.1 SEM image of produced in-situ fines.

Fines migration can occur in a variety of natural and technical processes, including water aquifer recharging from a peripheral water source, disposal of produced water back into underground porous and permeable formations, groundwater flows, drilling mud, and completion fluid invasion in the near-wellbore region, acidizing and conventional waterflooding treatments, petroleum production at high rates, and the inappropriate design

of crude oil recovery methods. There are van der Waals attractive and electric double layers, as well as Born repulsion forces, between the fines and sand grains in a reservoir environment. The attractive forces retain fine particles in the porous media, whereas EDL and Born repulsion forces tend to separate the fines and encourage migration, as presented in Figure 3.2. The total interaction potential of the system is determined using the principle of superposition, which takes into account both attractive and repulsive forces between fines and sand grains. The salinity, chemistry, ionic composition, and injection rate of the injected brine all have significant impacts on the procedure's efficiency by modifying the surface forces in sandstone and carbonate reservoirs.[26,28,31,175–177]

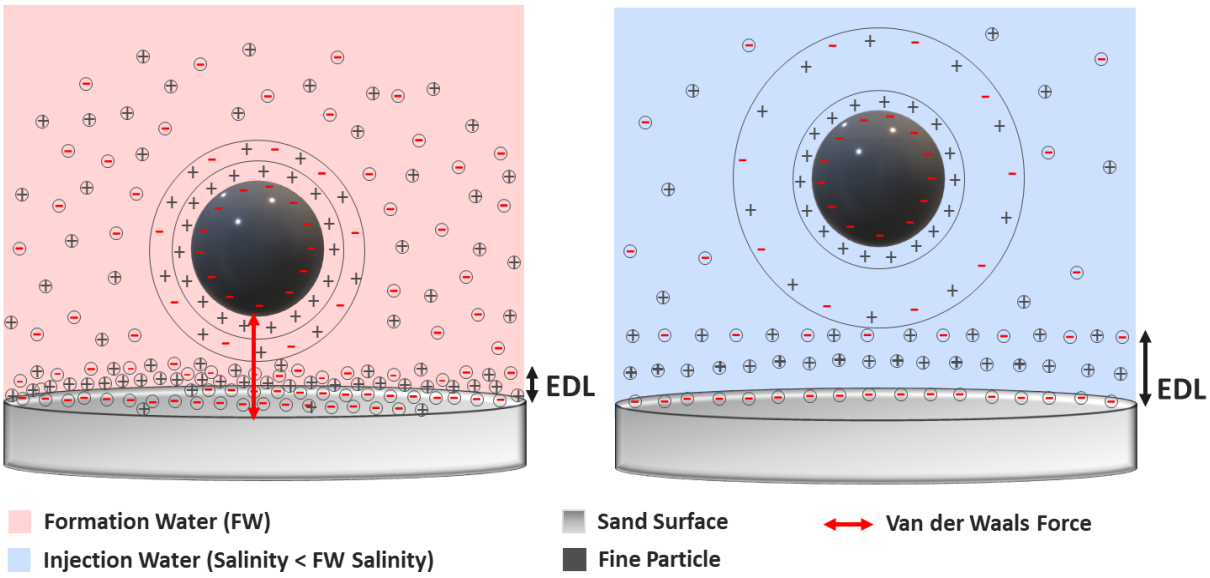

Figure 3.2 Schematic of fines detachment caused by a salinity gradient.

3.2 Materials and Methods

This work is subdivided into two phases. The first phase consisted of modeling the surface interactions using DLVO theory to predict the CSCs for monovalent and divalent brines. Furthermore, the critical pH was also predicted using DLVO modeling. The second phase included the validation of the developed model by performing corefloods and determining the actual CSC for each scenario. The materials and methods used in each phase are discussed hereafter.

3.2.1 DLVO Modeling

The objective of using DLVO theory in this research was to predict the CSC and

critical pH for fines migration initiation for Berea outcrop samples. The input parameters for the DLVO modeling included the measured zeta potentials at room temperature for the sand-brine system, injection brine salinity and ionic strength, and average fine particle size. The DLVO models presented in a previous study were used to compute the surface forces and predict the CSC for both monovalent and divalent brines and also under varying pH conditions.[178]

3.2.2 Monovalent and Divalent Brines

To determine the CSC for the sand-fine-brine system under investigation, different brines were prepared with decreasing salinities ranging from 0.2 to 0.05M NaCl and varying pH from 2 to 12. To prepare the brines, reagent grade NaCl provided by Sigma Aldrich was mixed with distilled water in the required amount using a magnetic stirrer. Formation water (FW) with a salinity of 77000 ppm was used to saturate the core samples for the experimental phase of the study. The solutions were stored in air-tight containers to avoid contamination and precipitation. Table 3.1 shows the composition and mass of NaCl used for each brine as well as the composition of the formation water.

NaCl+$CaCl_2$ brines were prepared with varying compositions and salinities ranging from 0.15M to 0.01M to predict the CSCs for the SFB systems under investigation. To make these brines, Sigma-Aldrich reagent-grade NaCl and $CaCl_2$ were combined with distilled water in calculated amounts using a magnetic stirrer. To avoid contamination and precipitation, the prepared solutions were kept in airtight containers. The composition of NaCl+$CaCl_2$ combinations, salinity, and ionic strength for each brine are shown in Table 3.2.

Table 3.1 Composition of formation water and injection NaCl brines.

Ions	*Formation water*	*NaCl brines*							
		0.2M	*0.15M*	*0.1M*	*0.09M*	*0.08M*	*0.07M*	*0.06M*	*0.05M*
	[ppm]								
Na^+	23426	4596	3447	2297	2068	1838	1608	1379	1150
Ca^{2+}	4448	-	-	-	-	-	-	-	-
Mg^{2+}	1300	-	-	-	-	-	-	-	-
Cl^-	47781	7093	5320	3547	3192	2837	2483	2128	1774
Total	76955	11693	8770	5847	5260	4675	4091	3506	2922

Table 3.2 Salinity and ionic composition of $NaCl+CaCl_2$ brines.

Salinity (M)	*$NaCl:CaCl_2$ = 9:1*					*$NaCl:CaCl_2$ = 8:2*				
	Ionic Composition									
	Ionic strength (M)	*Na^+*	*Ca^{2+}*	*Cl^-*	*Total*	*Ionic strength (M)*	*Na^+*	*Ca^{2+}*	*Cl^-*	*Total*
0.15	0.36	6207	1205	11699	19111	0.42M	5518	2405	12763	20685
0.1	0.24	4138	802	7800	12740	0.28M	3678	1603	8508	13790
0.05	0.12	2069	401	3900	6370	0.14M	1839	802	4254	6895
0.01	0.024	414	80	780	1274	0.028M	368	160	851	1379
	$NaCl:CaCl_2$ = 7:3					*$NaCl:CaCl_2$ = 4:6*				
0.15	0.48	4828	3607	13826	22261	0.66M	2759	7214	17016	26990
0.1	0.32	3219	2405	9217	14841	0.44M	1839	4810	11344	17993
0.05	0.16	1609	1202	4609	7420	0.22M	920	2405	5672	8997
0.01	0.032	322	240	922	1484	0.04M	184	481	1134	1799

3.2.3 Zeta Potentials

For sand-brine zeta potential measurement, the Berea sandstone core sample was crushed using a core-crushing apparatus and the crushed material was sieved through a 40 µm sieve to obtain a fine powder. The sand powder was thoroughly cleaned and washed several times to remove the impurities and obtain a representative sandstone sample. Several soakings in n-hexane, acetone, and distilled water were used to clean the sand. The sand was then dried for 24 hours in an atmospheric oven at 60 °C, washed in 0.5M hydrochloric acid, and finally washed in distilled water until the pH of the floating water was equal to the pH of the source distilled water. The zeta potentials of all the samples were measured using a Malvern Zetasizer after an equilibrium time of 24 hours to ensure sufficient interactions between the sand particles and brine. Furthermore, the sand-brine zeta potential data for KCl, $CaCl_2$, and $MgCl_2$ solutions were obtained from the literature and utilized in DLVO modeling. The given work aimed to predict the CSCs of monovalent and divalent salts in Berea sandstone samples using the DLVO modeling technique. Measured/collected zeta potentials for the sand-brine systems, injection brine ionic strength, and average fine particle size were utilized for the modeling, and CSCs were predicted for each case. The zeta potentials of dispersed sand in brine were also measured with varied pH using Malvern Zetasizer (NanoZS) and a Titrator system to quantify the effect of pH on zeta potentials.

3.2.4 Fines Characterization

One of the important input parameters for DLVO modeling is the size of the movable fine particles present inside the porous media. The selection of a particular DLVO model (plate–plate model, sphere–plate model) also requires prior knowledge of the shape of the in-situ fines. For this purpose, the in-situ fine particles were collected by performing a baseline flooding test on the same Berea sandstone core sample using distilled water. The recovered effluent was heated in the oven at 120 ^{o}C to evaporate the water and an in-situ fines sample was collected. The composition of the fine particles was determined through X-ray diffraction (XRD), and they were mainly composed of kaolinite clay ($Al_2Si_2O_5(OH)_4$). To estimate the average fine particle size, shape, and elemental composition, scanning electron microscopy (SEM) was used as shown in Figure 3.1.

3.2.5 Rock Samples

To estimate the CSC for sandstone reservoirs, Upper Berea sandstone outcrop samples were used. The elemental composition of the powdered rock sample was determined by SEM-EDS and XRF and is presented in Figure 3.3 and Table 3.3. The mineralogy of the rock sample was determined using XRD analysis, which revealed that the sample was mostly quartz with small quantities of iron oxide (Fe_2O_3), magnesium oxide (MgO), aluminum oxide (Al_2O_3), and aluminum silicate (Al_2SiO_5). as presented in Table 3.4. In total, 6 core samples with an average length of 7.5 cm and a diameter of 3.812 cm each were cut and oven dried. The dry weights of the samples were measured, and the cores were then saturated with formation water in a manual saturator by Vinci Technologies. The wet weight of each sample was measured, and porosities were calculated. The average liquid permeability and saturated porosity of the core samples were in the range of 300–350 mD and 19.2–19.4%, respectively.

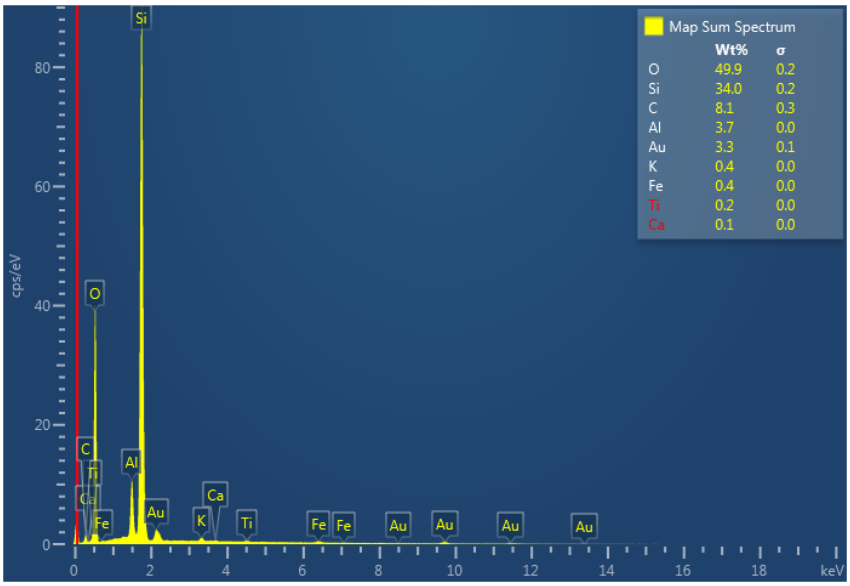

Figure 3.3 Scanning electron microscopy-Energy dispersive spectroscopy (SEM-EDS) results for sandstone sample.

Table 3.3 X-ray fluorescence (XRF) for sandstone sample.

Elements	*Concentration (%)*
Si	64.199
Al	3.623
O	2.024
Fe	12.775
Ca	3.365
K	6.697
Mn	0.371
P	1.046
Cr	2.196
Cl	0.228

Table 3.4 XRD analysis for Berea sandstone core.

Chemical Compound	*Chemical Formula*	*Weight %*
Quartz	SiO_2	87.14 ± 5.0
Kaolinite	$Al_2Si_2O_5(OH)_4$	6.41 ± 0.5
Aluminum oxide	Al_2O_3	3.97 ± 0.5
Iron oxide	Fe_2O_3	1.67 ± 0.3
Magnesium oxide	MgO	0.81 ± 0.5

3.2.6 Coreflood Tests

A set of coreflood tests was first conducted to determine a CSC for NaCl brine. All the experiments were performed at the ambient temperature of 24 ^{o}C. The confining

pressure was set at 1100 psi while the backpressure was maintained at 500 psi. Fines migration was observed using effluent turbidity and spectrophotometry results. A total of four corefloods were designed with the injection sequence given in Table 3.5. A soaking period of 15 hours was provided after each injection stage to achieve equilibrium and ensure sufficient contact between the injected brine, fine particles, and sand surface.

Table 3.5 Injection sequence for coreflood tests.

Test No.	*Injection Design*
1	Distilled water injection at increasing rates of 0.2 to 12 cc/min to collect maximum fines from the core.
2	0.20M NaCl → 15 hrs. soaking → 0.20M NaCl
3	0.15M NaCl → 15 hrs. soaking → 0.15M NaCl
4	0.10M NaCl → 15 hrs. soaking → 0.10M NaCl

The first test was designed for the collection of in-situ fines by saturating and flooding the core with distilled water. Experiments 2, 3, and 4 were designed to determine the critical salt concentration for the sand-fine-brine system. The designed NaCl brine was injected at a rate of 0.2 cc/min for 2 to 3 pore volumes (PVs) and a soaking period of 15 hours was provided. After soaking, the same brine was injected for 3 to 4 PVs, and the effluents' turbidity and light absorbance were analyzed for fines production. The pressure drop data were also recorded to observe any pressure changes caused by fines release, mobilization, and production. The same procedure was followed for all the tests until the critical salt concentration was obtained.

3.2.7 Effluent Analysis

The effluents recovered during coreflood tests were analyzed for the presence of fines using two techniques. The turbidity was measured using a turbidity meter for each PV collected, and the critical salt concentration was determined based on the ionic strength at which a sudden increase in turbidity was observed. An increase of 3–4 times and more in the effluent turbidity compared to the base brine injection stage was set as a criterion for CSC determination based on turbidity analysis. To confirm the turbidity results, the light absorbance of the effluents was also measured using a UV-Vis spectrophotometer. The fines containing effluents showed a relatively higher absorbance value, indicating the CSC in the SFB system under study. The experimental critical salt concentration values obtained

by turbidity and absorbance analysis were used to validate the DLVO models and quantitatively assess the effectiveness of nanotechnology.

3.3 Results and Discussion

3.3.1 Zeta Potential Measurements

Using a magnetic stirrer and an ultrasonic homogenizer, clean and washed sand particles were dispersed in NaCl brines, and the zeta potentials were measured for each case. A decrease in zeta potentials was observed with decreasing NaCl solution salinity (M), which corresponds to the expansion of the electric double layer, increase in the Debye length, and increase in the repulsive forces between sand grains and fine particles. Similarly, zeta potential also decreased with increasing pH of the solution due to an increase in OH^{-1} ions concentration. The measured zeta potentials are given in Table 3.6.

Table 3.6 Measured zeta potentials.

NaCl Salinity (M)	*Measured Zeta Potential (mV)*
0.20	-29.5
0.15	-30.6
0.11	-30.9
0.10	-30.8
0.09	-31.6
0.085	-32.0
0.08	-32.5
0.075	-33.3
0.07	-32.8
0.06	-33.6
0.05	-35.2

The zeta potential data for NaCl - sand, and NaCl+$CaCl_2$–sand solutions of various concentrations were measured in the lab using a Zetasizer. With decreasing NaCl solution salinity (M), zeta potentials also decreased, corresponding to the expansion of the electric double layer, increase in Debye length, and increase in repulsive forces between sand grains and fine particles. In contrast to simply NaCl–sand zeta potentials, the presence of varying quantities of $CaCl_2$ in NaCl–sand solutions raised the zeta potential. Because calcium ions have a double charge, the solution has a higher ionic strength than NaCl, resulting in a shorter Debye length and less repulsion force in the presence of divalent salt. Due to the valence of one, the salinity and ionic strength of monovalent salt solutions

remain the same, however, adding divalent salt to monovalent salt solutions increases the ionic strength of the solution because of the high charge and the valence of two.

The zeta potential data for KCl–sand, $CaCl_2$–sand, and $MgCl_2$–sand systems were acquired from various sources. Because the KCl salt solution contains a single charge, its salinity and ionic strength remain constant. However, because of their valence of two and high charge, the ionic strength of $CaCl_2$ and $MgCl_2$ solutions differs from their salinity. The Debye length is suppressed by the high ionic strength of the divalent salt solutions, resulting in high zeta potentials (more positive) and a weak repulsion between fines and sand grains. Table 3.7 shows the measured and collected zeta potential data for monovalent and divalent brines considered in this study.

Table 3.7 Zeta potential data.

Type of salt	*Salinity (M)*	*Ionic strength (M)*	*Zeta potential (mV)*	*Operating conditions*	*Data source*
NaCl+CaCl₂ (9:1)	0.15	0.36	-12.6	pH = 6.9 – 7.1, Temp = 25ºC	Measured in the lab using a Zetasizer
	0.1	0.24	-16.3		
	0.05	0.12	-18.2		
	0.01	0.024	-21.1		
NaCl+CaCl₂ (8:2)	0.15	0.42	-10.2		
	0.1	0.28	-12.1		
	0.05	0.086	-15.8		
	0.01	0.028	-17.1		
NaCl+CaCl₂ (7:3)	0.15	0.48	-8.5		
	0.1	0.32	-11.6		
	0.05	0.16	-13.5		
	0.01	0.032	-15.1		
NaCl+CaCl₂ (4:6)	0.15	0.66	-5.9		
	0.1	0.44	-8.3		
	0.05	0.22	-10.5		
	0.01	0.04	-11.5		
KCl	0.00001	0.00001	-75	pH = 6.0, Temp = 25ºC	Alkafeef S. F. et al. [179]
	0.007	0.007	-57		
	0.011	0.011	-48		
	0.027	0.027	-27		
	0.08	0.08	-16		
	0.1	0.1	-11		
CaCl₂	0.45	1.35	-4.0	pH = 7 – 7.3 Temp = 23 – 25 ºC	Xie et al., Shuai Li et al., and Jan et al. [180–182]
	0.35	1.05	-6.03		
	0.1	0.3	-6.33		
	0.09	0.27	-5.5		
	0.045	0.135	-7.03		
	0.02	0.06	-10.2		
	0.015	0.045	-10.8		
MgCl₂	0.53	1.59	-4	pH = 6.8 – 7.4 Temp = 20 – 25 ºC	Xie et al., Shehata et al.,
	0.45	1.35	-7.5		
	0.45	1.35	-8.6		

	0.11	0.33	-5		and Farooq et al. [163,180,183]
	0.053	0.159	-5.8		
	0.02	0.06	-10.1		

The zeta potentials of dispersed sand particles were measured with varying pH of the dispersion as shown in Table 3.8. As the pH of the solution increases, the electric double layer expands, and the corresponding zeta potential decreases. To further assess the effects of pH level changes in a high-salinity system, consisting of crushed sandstone grains with kaolinite particles and a 0.2M solution of 8 wt% NaCl with 2 wt% $CaCl_2$, zeta potential data were collected from relevant literature.

Table 3.8 Measured and collected zeta potential data.

Medium and ionic strength	*pH*	*Zeta*	*Source*
0.2M NaCl	2	-5	Measured by Zetasizer with a titrator
	3	-9	
	4	-12.5	
	5	-15	
	6	-18.2	
	7	-20.4	
	8	-23.7	
	9	-25.8	
	10	-27.5	
	11	-28.9	
	12	-31	
2M (8 wt% NaCl + 2 wt% CaCl2)	2	-7	Singh et al.[184]
	3.5	-11	
	5	-16	
	6	-22.5	
	6.5	-26	
	7	-28	
	8.5	-32	

3.3.2 Development of zeta potential correlations

To determine zeta potentials at the desired salinity, correlations for the KCl - sand, $CaCl_2$ - sand, $MgCl_2$ - sand, and NaCl+$CaCl_2$–sand systems were developed based on the measured and gathered zeta potential data in Table 3.7.

3.3.3 Correlation for KCl-Sand System

Based on the data collected for the KCl–sand system (pH = 6.0, temperature = 25

°C), two linear correlations were developed to estimate the zeta potential of the given system at high and low salinity conditions, as shown in Figure 3.4. The developed correlations for high-salinity (0.027–0.1 M) and low-salinity (0.0001–0.027 M) conditions are presented in Equations 3.1 and 3.2, respectively.

$$\zeta\text{-}potential = 216.8 \times M - 32.959 \quad (3.1)$$

$$\zeta\text{-}potential = 1713.3 \times M - 71.029 \quad (3.2)$$

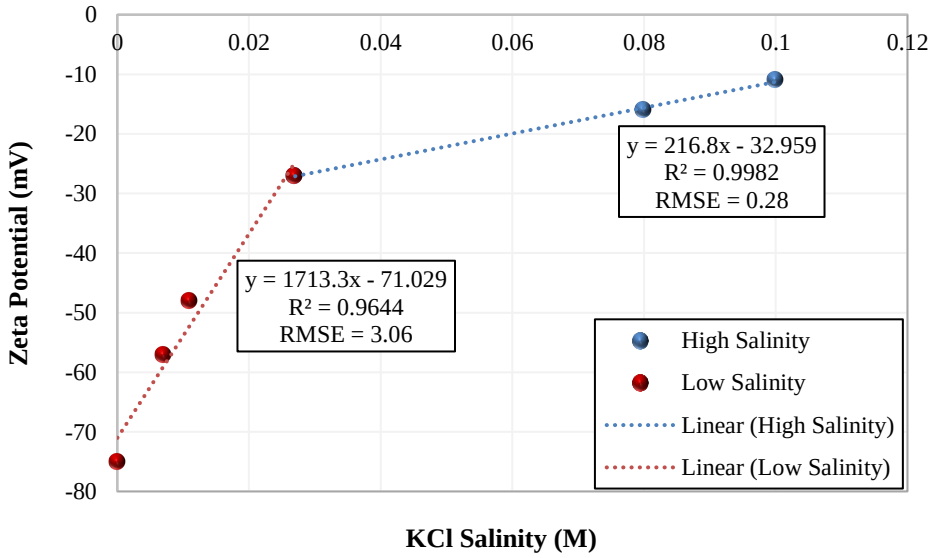

Figure 3.4 Zeta potential correlations for KCl–sand system.

3.3.4 Correlation for $CaCl_2$-Sand System

Based on the data obtained in Table 3.7 for the $CaCl_2$–sand system (pH = 7–7.3, temperature = 23–25 °C), two linear correlations were developed to estimate the zeta potential of the $CaCl_2$–sand system at high and low salinity conditions, as shown in Figure 3.5.

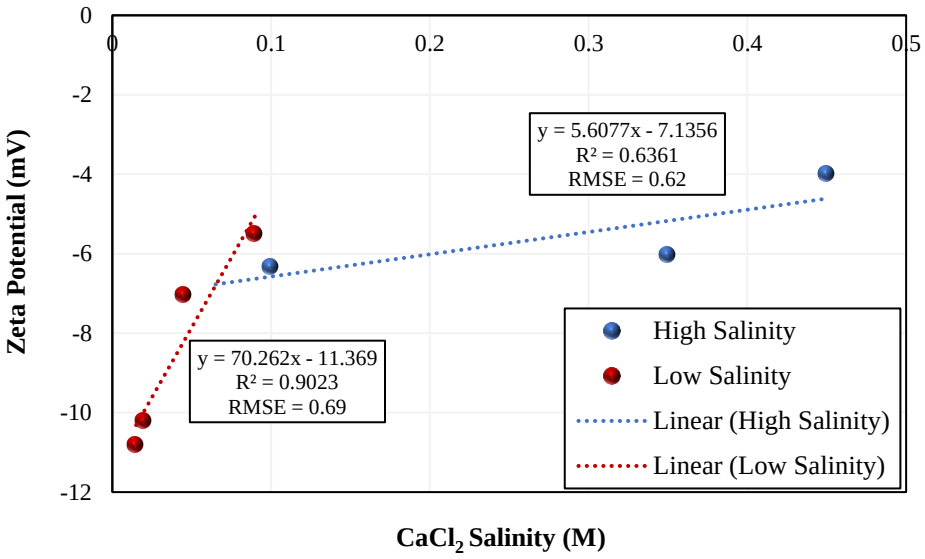

Figure 3.5 Zeta potential correlations for $CaCl_2$–sand system.

The developed correlations for the high-salinity range (0.07–0.45 M) and low-salinity range (0.015–0.07 M) conditions are shown in Equations 3.3 and 3.4, respectively.

$$\zeta\text{-}potential = 5.6077 \times M - 7.1356 \quad (3.3)$$

$$\zeta\text{-}potential = 70.262 \times M - 11.369 \quad (3.4)$$

3.3.5 Correlation for $MgCl_2$-Sand System

Two linear correlations were developed based on the data collected in Table 3.7 for the $MgCl_2$ - sand system (pH = 6.8–7.4, temperature = 20–25 ^oC), as shown in Figure 3.6, to determine the zeta potential of the given system for high and low salinity conditions.

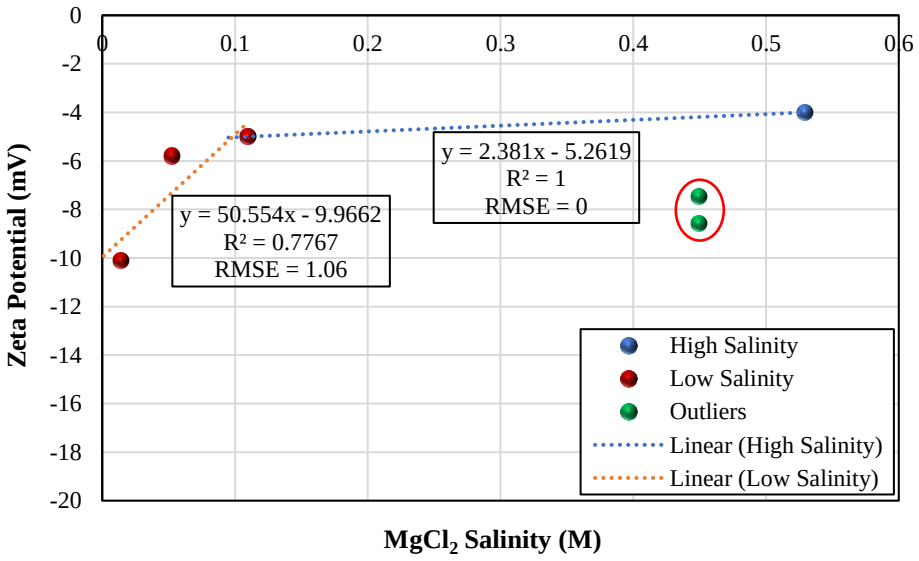

Figure 3.6 Zeta potential correlations for $MgCl_2$–sand system.

The developed correlations for the high-salinity range (0.07–0.45 M approx.) and low-salinity range (0.015–0.07 M) conditions are shown in Equations 3.5 and 3.6, respectively.

$$\zeta\text{-}potential = 2.381 \times M - 5.2619 \quad (3.5)$$

$$\zeta\text{-}potential = 50.554 \times M - 9.9662 \quad (3.6)$$

3.3.6 Correlations for NaCl+$CaCl_2$-Sand System

Table 3.7 shows the zeta potential values for NaCl + $CaCl_2$ - sand systems at various salinities with varied proportions of monovalent and divalent salts. To determine the zeta potentials at specified lower salinity values, correlations were developed for 9:1, 8:2, 7:3, and 4:6 cases of mixed solutions of NaCl+$CaCl_2$ salts as presented in Figure 3.7, and Equation 3.7 to Equation 3.10.

$$\zeta\text{-}potential = 62.009 \times M - 22.131 \quad (3.7)$$

$$\zeta\text{-}potential = 52.099 \times M - 17.838 \quad (3.8)$$

$$\zeta\text{-}potential = 46.343 \times M - 15.767 \quad (3.9)$$

$$\zeta\text{-}potential = 40.677 \times M - 12.202 \quad (3.10)$$

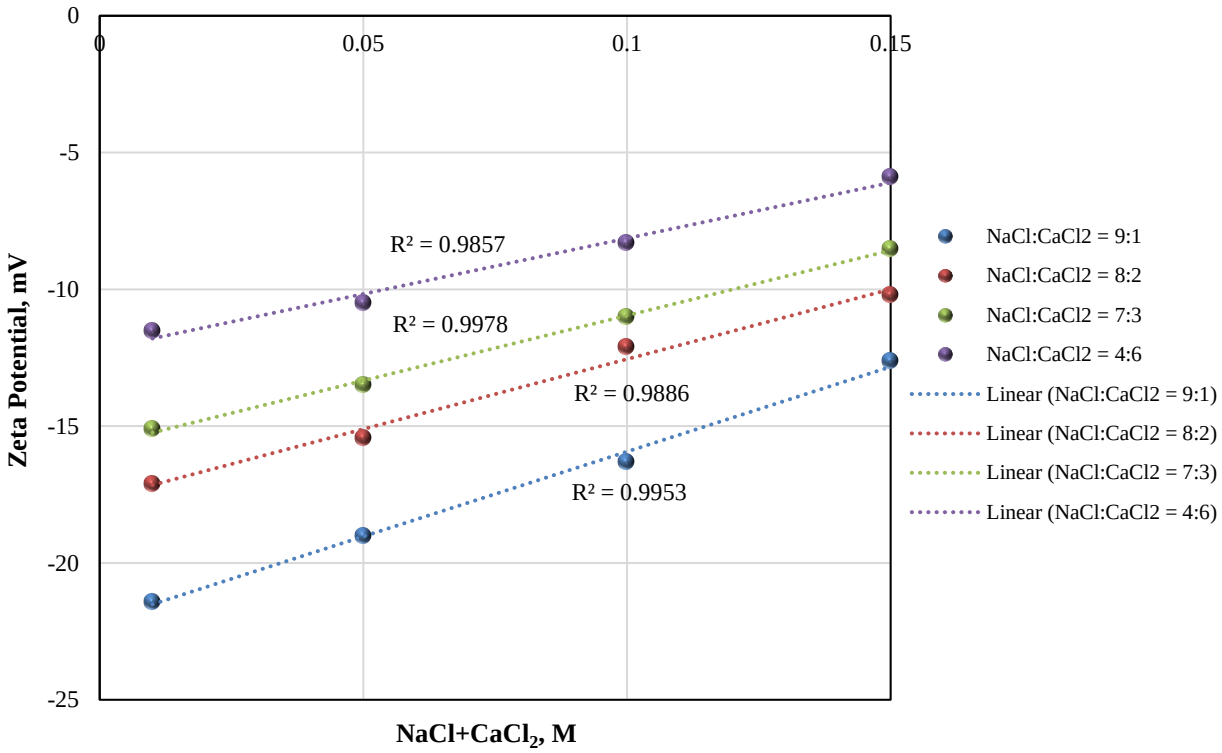

Figure 3.7 Zeta potential correlations of NaCl+$CaCl_2$–sand systems for proportions of 9:1, 8:2, 7:3, and 4:6.

3.3.7 DLVO Modeling and CSC Prediction for Monovalent and Divalent Salts

The following section presents the DLVO models for the prediction of CSC for NaCl, KCl, $CaCl_2$, $MgCl_2$, and combinations of NaCl+$CaCl_2$ brines.

3.3.7.1 DLVO Model CSC for NaCl Brine

The measured zeta potentials for dispersed sand particles, the salinity of each NaCl brine, and the average size of fine particles measured by scanning electron microscopy were used to quantify the attractive and repulsive surface forces between sand grains and fine particles using Equations 2.4, 2.10, and 2.13. The dimensionless total interaction energy of each system was then calculated using the principle of superposition and the DLVO model was developed using Equation 2.3, as shown in Figure 3.8.

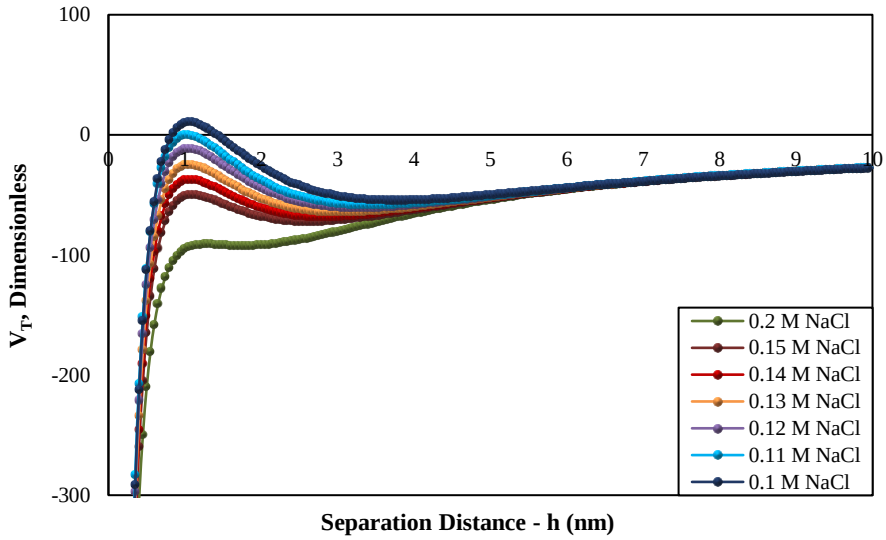

Figure 3.8 DLVO modeling to predict CSC for NaCl brine.

In the high salinity environment of 0.2M NaCl solution, the Debye length and electric double layers were compacted and van der Waals attractive forces dominated the repulsive forces, and the resultant total energy of the system remained negative, which implied that there was no fines migration in the system. Similar results were obtained for the 0.15M to 0.12M NaCl brine scenarios with the total interaction energy in the negative region with a minor increment in the Debye length as shown in Table 3.9.

Table 3.9 The Debye length and potential barrier as a function of different salinities.

Salinity (M)	k^{-1}*(nm)*	$V_{T_{Maximum}}$	$V_{T_{Barrier}}$
0.2	0.685	-93.02	--
0.15	0.791	-49.49	--
0.14	0.819	-36.94	--
0.13	0.850	-24.55	--
0.12	0.885	-11.10	--
0.11	0.924	0.18	0.18
0.1	0.969	7.21	7.21

However, for 0.11M brine, a further increase in Debye length was observed in the model and the total interaction energy moved from a negative to a positive value with a potential barrier of 0.18 dimensionless energy, indicating the dominance of repulsive forces in the system at a separation distance of 0.924 nm. This can be attributed to the expansion of the electric double layers around the fines and sand grains under low salinity conditions.

Based on the DLVO model results, it was inferred that 0.11M NaCl was the CSC for the SFB system under investigation.

3.3.7.2 DLVO Model CSC for KCl Brine

Zeta potentials at desirable salinities were determined by applying Equation 3.2 for the low-salinity KCl-sand system. Using the computed zeta potentials for dispersed sand particles in KCl solutions, the attractive and repulsive surface forces between sand grains and fine particles were evaluated using a similar scenario of the NaCl-sand system presented in the Section. The dimensionless total interaction energy of each case was estimated, and the DLVO model was constructed as illustrated in Figure 3.9.

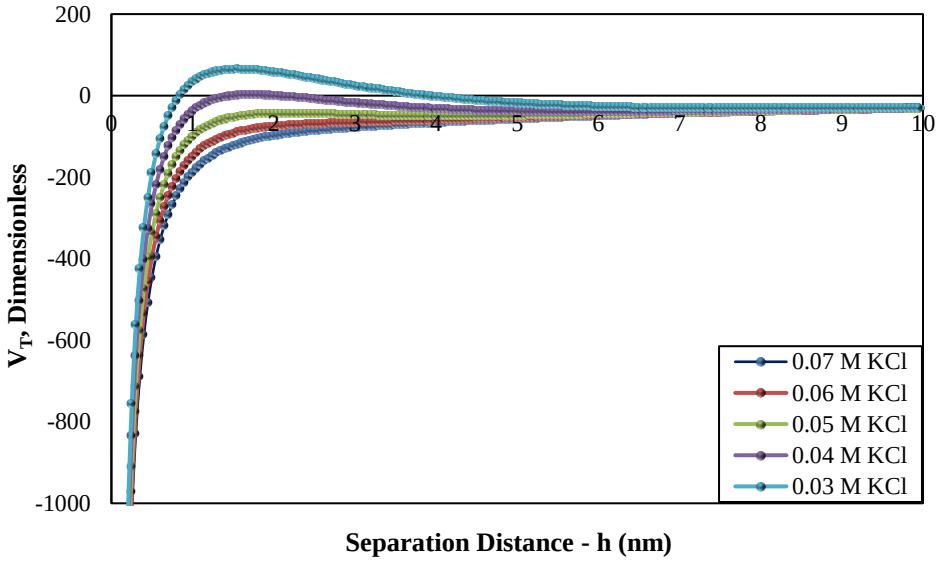

Figure 3.9 DLVO modeling to predict CSC for KCl brine.

The DLVO model displays the overall interaction energy (V_T) in the negative region at 0.07M KCl-system salinity, showing the dominance of attractive forces between fines and sand grains. However, as the system salinity decreased in steps, the E_T value shifted from negative to positive at a salinity of 0.04M KCl due to the expansion of electric double layers, indicating that the repulsion forces had overcome the attraction forces and fines release could occur in the system at a salinity of 0.04M, which is the CSC for the KCl-sand system.

3.3.7.3 DLVO Model CSC for $CaCl_2$ and $MgCl_2$ Brines

The zeta potentials of the $CaCl_2$-sand and $MgCl_2$-sand systems were calculated

individually under low salinity conditions (0.005, 0.0005, and 0.0001M) using Equations 3.4 and 3.6. As shown in Figures 3.10 and 3.11, the DLVO models were developed to characterize the overall interaction energy of the system (V_T) in each situation to determine the CSC for divalent salts. The V_T for separate brines of $CaCl_2$ and $MgCl_2$ salts with salinities of 0.005 and 0.0005M remained in the negative zone. The reason for this is that the ionic strength (I_s) of divalent salt solutions is larger than their salinity, and this higher ionic strength reduces the Debye length, resulting in contracted electric double layers and reduced repulsion even at lower salinities of 0.005 and 0005M. However, when the salinity was reduced further in both cases, the total system energy became positive at a salinity of 0.0001M, showing that both $CaCl_2$ and $MgCl_2$ brines have a CSC of 0.0001M.

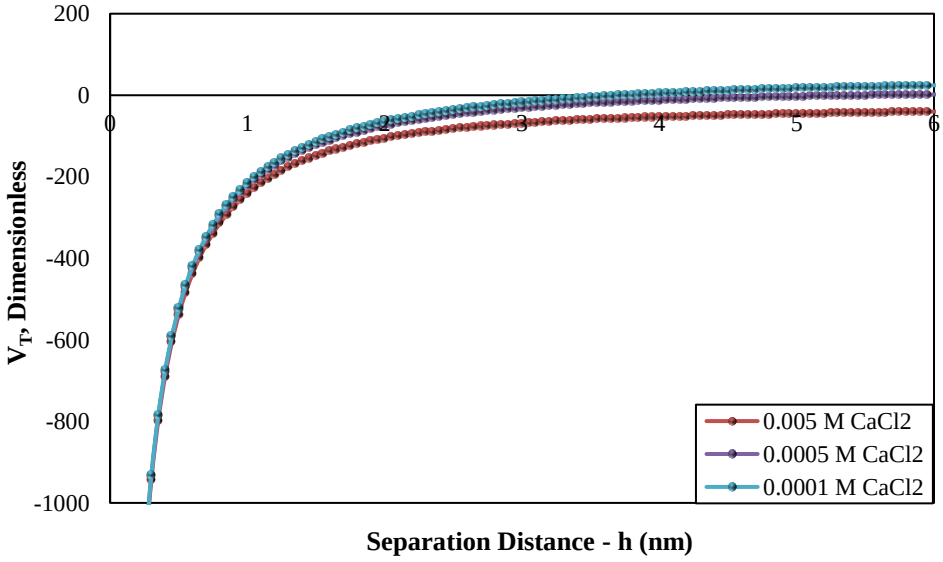

Figure 3.10 DLVO modeling to predict CSC for $CaCl_2$ brine.

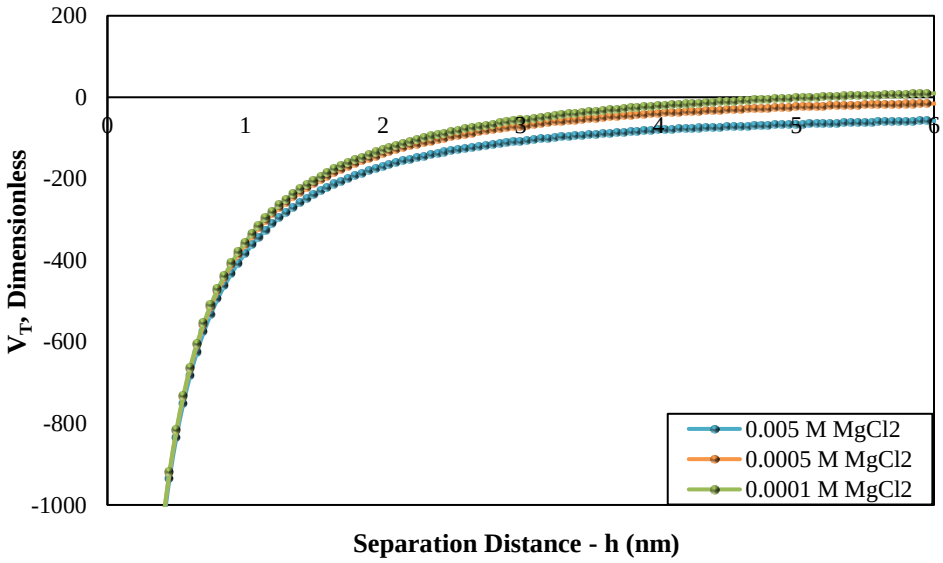

Figure 3.11 DLVO modeling to predict CSC for $MgCl_2$ brine.

As given in Equation 2.1, one of the input parameters used to compute Debye length is the brine's ionic strength. Because monovalent ions have a single charge, their salinity and ionic strength remain constant. On the other hand, due to the valence of two, the ionic strength of divalent brine is higher than its salinity, which prevents the expansion of EDLs. Figure 3.12 shows the comparison of Debye lengths for monovalent and divalent ions for the same salinity. In the presence of divalent ions, the Debye length remains shorter than in the presence of monovalent ions. A Debye length of 0.969 nm was obtained with a salinity of 0.1M for NaCl, whereas a Debye length of 0.560 nm was obtained with the same salinity of $CaCl_2$.

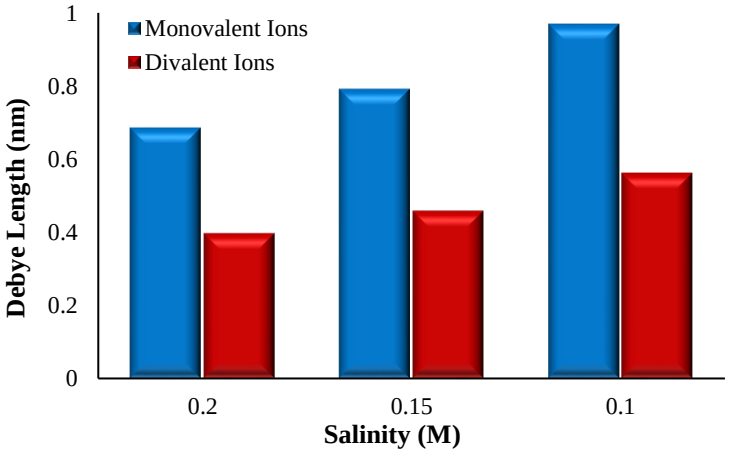

Figure 3.12 Comparison of Debye lengths in monovalent and divalent ions.

3.3.7.4 Model CSC for NaCl+$CaCl_2$ (9:1, 8:2, 7:3, and 4:6)

As illustrated in Figure 3.13, DLVO models were made to examine the combined influence of monovalent and divalent ions on fines migration and predict CSC using the measured zeta potentials for the NaCl+$CaCl_2$-sand system (9:1) provided in Table 3.7. According to the DLVO model, adding a small amount of $CaCl_2$ to a NaCl solution lowers the CSC from 0.1M for a pure NaCl - sand system to 0.01M for a combination of NaCl + $CaCl_2$ brine. This is because divalent ions can inhibit the expansion of electric double layers even at reduced salinity.

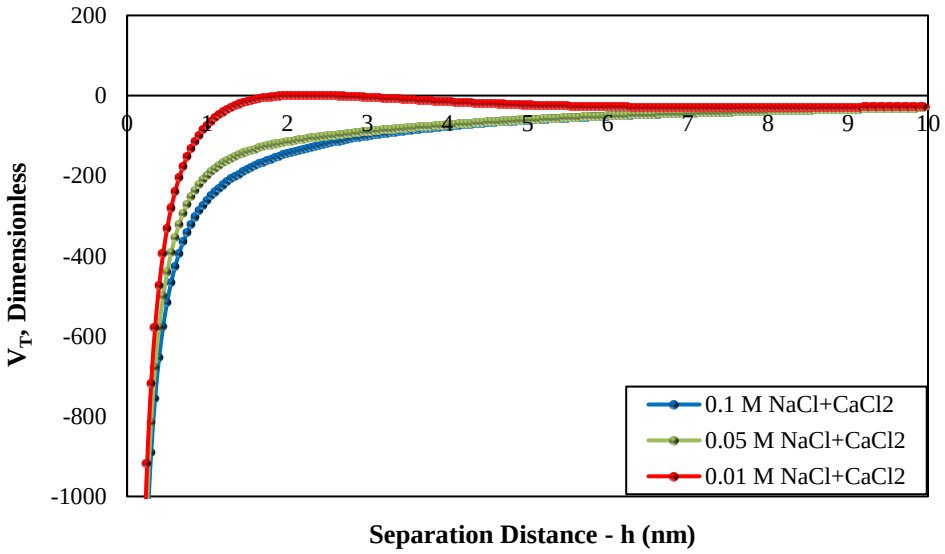

Figure 3.13 DLVO modeling to predict CSC for NaCl+$CaCl_2$ brine (9:1)

Similarly, zeta potentials for NaCl+$CaCl_2$-sand systems were determined using proportions of 8:2, 7:3, and 4:6, and three correlations were developed. Zeta potentials for reduced salinities were determined using Equations 3.7 to 3.10, and DLVO models were developed to determine CSCs for NaCl+$CaCl_2$ proportions of 8:2, 7:3, and 4:6, as shown in Figures 3.14–3.16. Based on surface force analysis and computation of total interaction energy of given systems, the CSCs were found to be 0.003M, 0.001M, and 0.0004M for NaCl+$CaCl_2$ proportions of 8:2, 7:3, and 4:6, respectively.

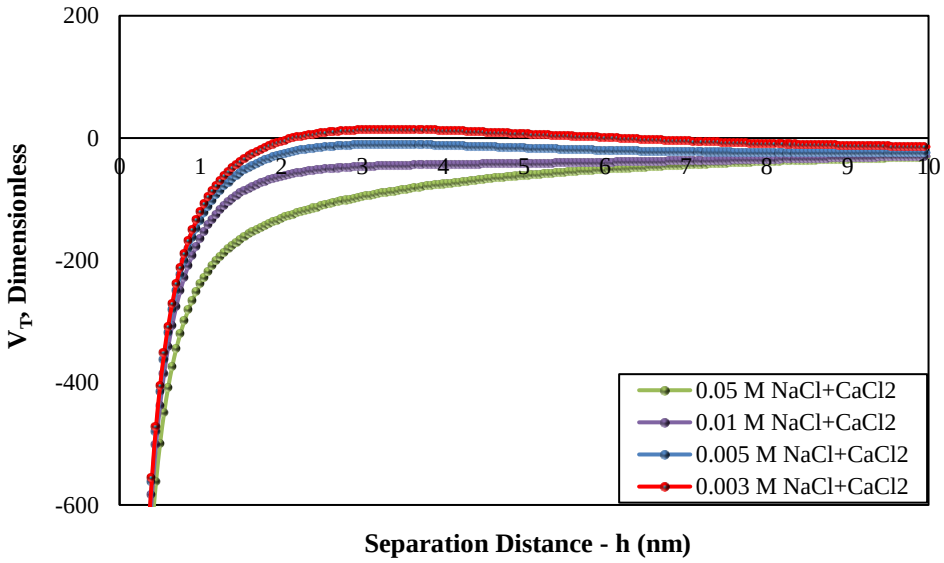

Figure 3.14 DLVO modeling to predict CSC for NaCl+$CaCl_2$ brine (8:2).

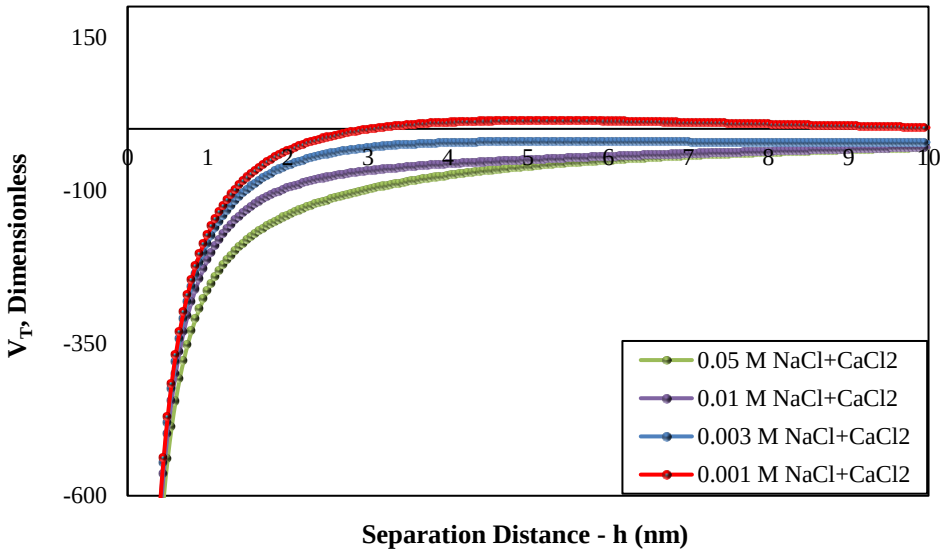

Figure 3.15 DLVO modeling to predict CSC for NaCl+$CaCl_2$ brine (7:3).

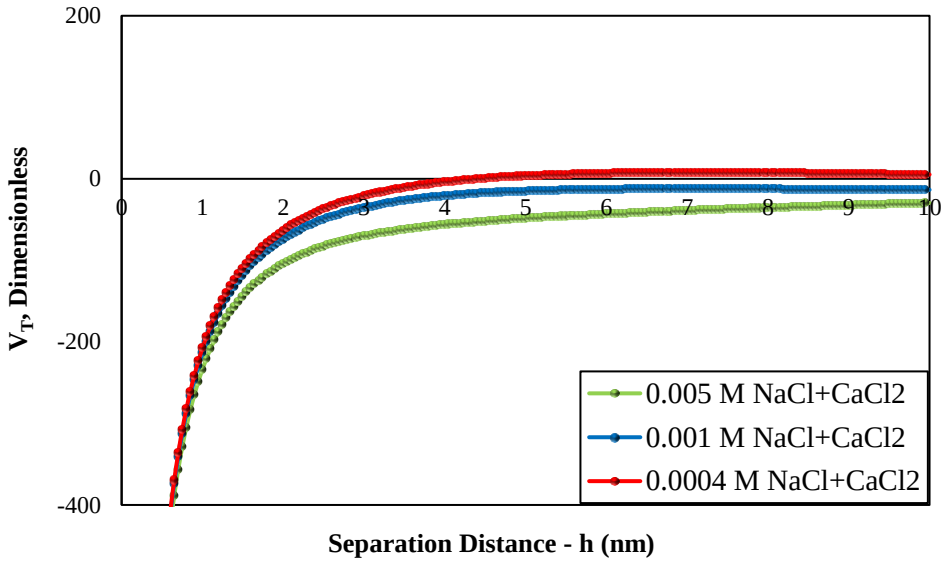

Figure 3.16 DLVO modeling to predict CSC for NaCl+$CaCl_2$ brine (4:6).

It was observed that increasing the divalent salt concentration in NaCl brine decreases the CSC because of a reduction in the electric double layers. A 100% NaCl brine has a higher CSC than a 100% $CaCl_2$ brine, which has a lower CSC. Based on the CSC results from Figure 3.8, as well as Figures 3.14–3.16, a trend has been established to describe how increasing divalent ions concentration reduces the CSC due to the gradual contraction of electric double layers, as shown in Figure 3.17.

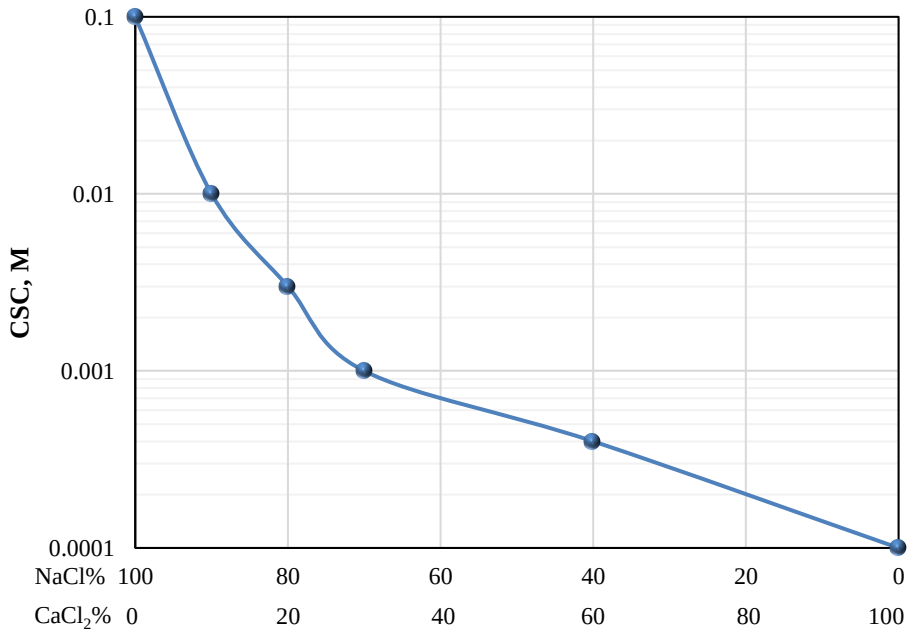

Figure 3.17 A trend between CSC and the concentration of monovalent and divalent ions.

3.3.7.5 Critical pH by DLVO Modeling

Surface forces between fine and sand grain were estimated using observed zeta potentials under various pH conditions and brine ionic strength from Table 3.8. The total interaction energy of each system was determined using DLVO modeling, as shown in Figure 3.18. Using the models presented in Chapter 2, surface forces were determined. The sum of attraction and repulsion potential is the total interaction energy of the system under consideration. Due to compacted electric double layers around fines and sand grains in a low pH environment, such as a pH=3 solution, forces of attraction dominate repulsion forces, and the total energy is negative, indicating that there will be no fines migration in the system. The same findings were achieved for the total interaction energy in the negative region for pH 4-7 environments. However, for brine of pH=8, the total interaction energy shifted from negative to positive indicating the dominance of repulsive forces in the system at a separation distance of around 0.25 nm. This can be attributed to the expansion of electric double layers around fines and sand grains under high pH conditions. Based on the DLVO model results, pH 8 was predicted to be the critical pH, and fines migration in the sand-fine-brine system may occur at or above this value.

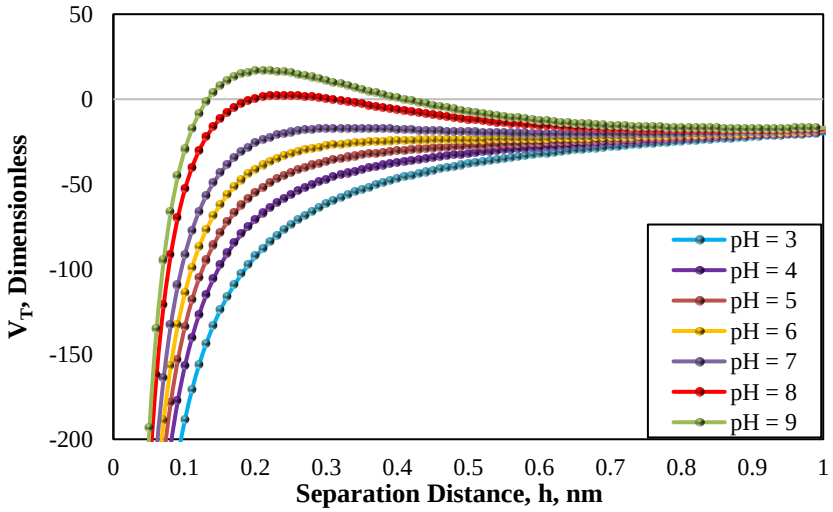

Figure 3.18 Prediction of critical pH using DLVO modeling.

Similarly, a DLVO model has been developed by using the data of Singh et al.[184] to analyze the effect of pH values ranging from 2 to 8.5 as shown in Figure 3.19. The critical pH value to initiate fines migration is between 6 and 6.5 for this case. Thus, maintaining the system pH below 6.5 can prevent fines migration. This calculation suggests

that the use of alkaline flooding can lead to fines migration, as the pH level during alkaline flooding exceeds 7.

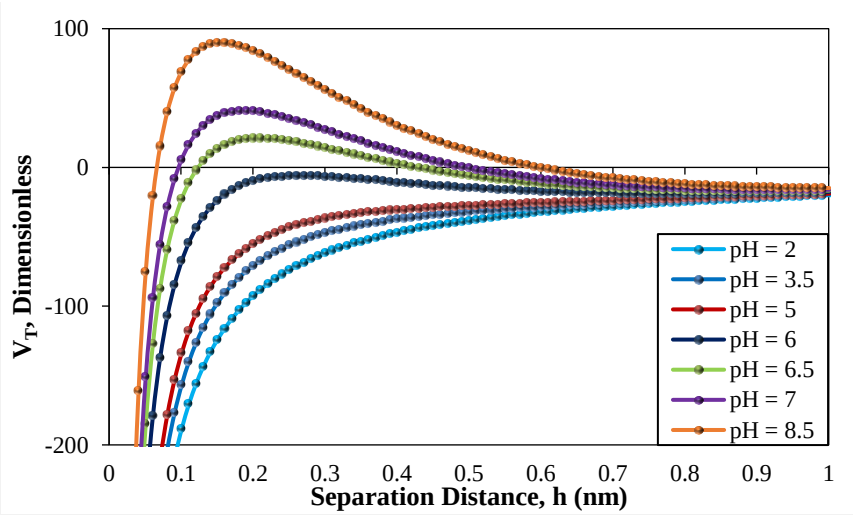

Figure 3.19 Prediction of critical pH using DLVO modeling.

3.3.8 Experimental Validation of DLVO Models

Three corefloods were performed on the Berea sandstone cores saturated with formation water to validate the DLVO modeling results. During the first coreflood, three pore volumes (PVs) of 0.2M NaCl brine were injected at a low rate of 0.2 cc/min, and the pressure drop across the core with effluent turbidity against each PV was measured as shown in Figure 3.20a. Later, 15 hours of soaking was provided to achieve equilibrium between the attractive and repulsive surface forces as the system salinity was reduced from 7.7 wt% (1.51M FW) to 1.2 wt% (0.2M NaCl). After the soaking period, the same 0.2M NaCl brine was injected to check the initiation of fines migration in the system. The effluent collected after the 4th PV showed turbidity of 1.35 NTU, which may be due to some mineral dissolution in the SFB system. The average turbidity and absorbance of the effluents were measured for each injection stage based on the set criteria and as given in Table 3.5. The pressure drop remained stable, implying that the attractive forces were dominant during the 0.2M NaCl injection scenario. Moreover, a low value of light absorbance also confirmed the absence of fines in the effluent.

For the second coreflood, the same methodology was followed, and the pressure drop, and effluent turbidity were measured as depicted in Figure 3.20b. The average turbidity and absorbance of the effluents before and after soaking were still low as shown

in Table 3.10, showing that no fines had been released and migrated in the system under the given conditions. Following the same procedure, the third core flood was carried out. The average turbidity was 1.05 NTU with a stable pressure drop. However, once the injection resumed after the soaking period, the pressure drop in the system spiked to a high value with considerable fluctuations, as shown in Figure 3.20c.

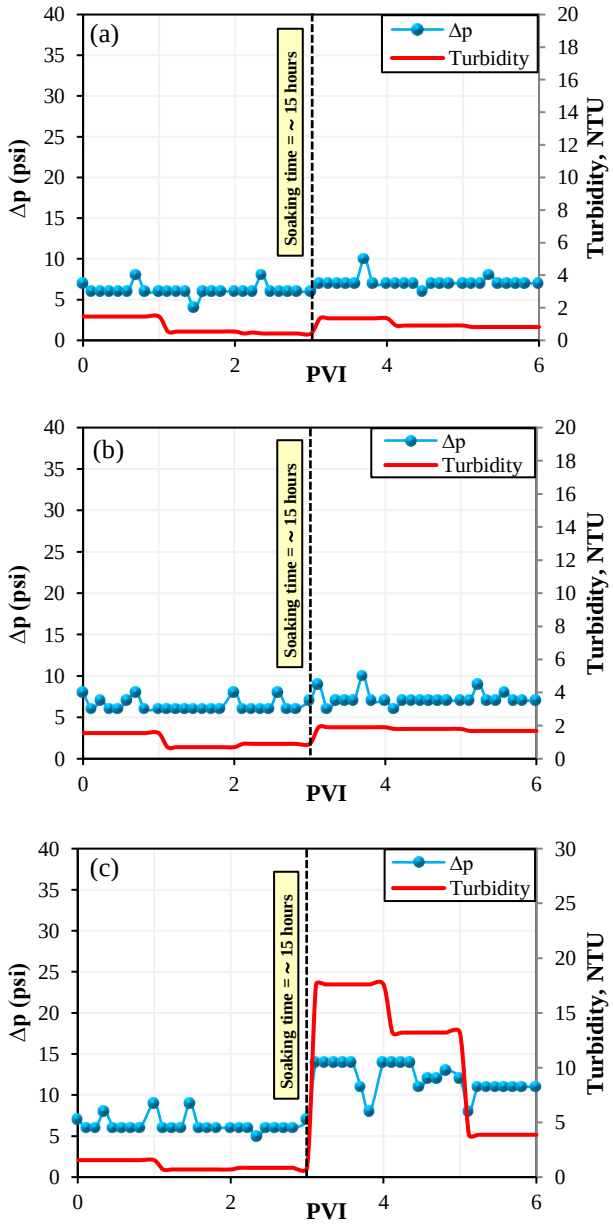

Figure 3.20 Pressure drops and effluent turbidity for (a) 0.2M, (b) 0.15M, and (c) 0.1M NaCl.

Table 3.10 Effluent turbidity and absorbance analysis for estimation of CSC.

Salinity (M)	*Turbidity (NTU)*	*Absorbance (ABS)*
0.20	1.35	0.025
0.15	1.90	0.167
0.10	17.6	0.415

The effluent recovered after the 4th PV had the highest turbidity of 17.6 NTU and light absorbance of 0.415 ABS, indicating the presence of fines in the effluent. In addition to effluent turbidity measurements, effluent absorbance was also measured using a UV-VIS Spectrometer to confirm the presence of fines in the effluent. The critical salt concentration for the SFB system was estimated to be between 0.15M and 0.1M NaCl based on the coreflood results. These results validated the developed DLVO models, and a close agreement was found between the DLVO prediction of 0.11M NaCl and the experimental results.

Furthermore, the CSCs for the brines of KCl, $CaCl_2$, and $MgCl_2$ were validated using the results of the experimental study by Khilar & Fogler.[17] They measured the CSCs for monovalent and divalent ions in several experiments on sandstone samples. Table 3.11 illustrates the experimental data of the CSCs that are consistent with the predictions of the DLVO models. Our DLVO modeling technique is straightforward and has low error since it accurately predicts the CSC without requiring extensive experimentation.

Table 3.11 Experimental validation of CSC predicted by DLVO models.

Salt type	*CSC predicted by the DLVO model*	*Experimental CSC*	*Validation source*
NaCl	0.11 M	0.1 M	Muneer et al.[185]
KCl	0.04 M	0.044 M	Khilar and Fogler.[17]
$CaCl_2$	0.0001 M	<0.0001 M	
$MgCl_2$	0.0001 M	<0.0001 M	

3.4 Summary

Fines migration in sandstones is a well-known phenomenon during drilling and completion operations, conventional waterflooding, alkaline flooding, water aquifer recharging from an external water source, and formation water disposal in underground formations. In this context, the prediction of the CSC and critical pH is crucial to control

fines migration to prevent formation damage. The following conclusions are made:

- Sand-fine-brine systems were defined, and important input parameters such as fine particle size, zeta potentials, and system pH and temperature were carefully measured to minimize the error.
- The CSC of monovalent brines was higher than that of divalent brines. This is because monovalent brine has the same salinity and ionic strength whereas the ionic strength in divalent brine is greater than the salinity due to the double charge.
- In standalone cases, the electric double-layer expansion in the presence of monovalent ions is greater than that of divalent ions. The greater expansion of EDLs in the presence of monovalent brine is attributed to the single charge on ions, which leads to the rapid generation of a repulsion force when salinity is reduced.
- For monovalent brines, the DLVO models predicted CSCs of 0.11M, and 0.04M for NaCl and KCl, respectively, and experimental CSCs were found comparable to predicted values.
- The presence of divalent ions in the formation water and injection brine is beneficial in the retention of fines and results in a lower CSC. The DLVO model predicted a CSC of 0.0001M for the $CaCl_2$ and $MgCl_2$ brines, which was confirmed by experimental results.
- Monovalent and divalent ions are always present in the formation water and injection brines in different concentrations. For different scenarios of combined NaCl+CaCl2 brines in proportions of 9:1, 8:2, 7:3, and 4:6, the DLVO model predicted CSCs of 0.01M, 0.003M, 0.001, and 0.0004M, respectively.
- A critical pH for a sand-fine-brine system was also predicted using the DLVO modeling technique. The DLVO model predicted a critical pH of 8 at which the total interaction energy of the SFB system moved from negative to positive, indicating the dominance of repulsion forces in the system.
- Based on the quantification of surface forces, DLVO modeling is a useful tool for estimating the CSCs in the presence of monovalent and divalent ions, both individually and in combinations, as well as the critical pH under varying pH conditions.

CHAPTER 4: Application of Nanoparticles to Control Fines Migration

The application of nanoparticles is one of the emerging technologies used to fix the fines migration problem in sandstone reservoirs. Silica nanoparticles, due to their unique properties and surface characteristics, have shown promising potential in mitigating fines migration-related problems. The mechanisms behind this mitigation can involve the adsorption of nanoparticles on the sand surface and reduction in electric double-layer repulsion force. Silica nanoparticles typically carry a net negative charge, which can interact with the negatively charged fine particles present in the reservoir or porous media. This electrostatic attraction helps immobilize the fines and prevents them from moving with the flow of fluids, thereby reducing the risk of pore blockage and formation damage. This chapter presents the incorporation of the effect of silica nanoparticles in the DLVO model and demonstrates the application of nanotechnology to control fines migration in sandstone reservoirs. This chapter is based on the results published in the referenced articles[e,f].

4.1 Introduction

The DLVO theory finds its application in the petroleum industry for assessing the surface forces between fine particles and sand grains when dealing with nanofluid injection scenarios. DLVO-based interactions have been found to agree closely with experimental results. Habibi et al. used NPs in synthetic cores to tackle fines migration, calculating total interactions. MgO NPs reduced the repulsion force between fines and grain surfaces.[90,186] Arab et al. tested various nanoparticles to control fines migration during low-salinity flooding on glass beads. ZnO and γ-Al_2O_3 NPs were the most effective. They also measured zeta potentials, using a DLVO sphere-plate model to calculate interactive energy, which became attractive after nanoparticle application.[187] In another study, Arab et al. used SiO_2 and MgO NPs in pre-flush mode, with 0.03% MgO NPs being the most successful in

[e] Muneer, R.; Hashmet, M. R.; Pourafshary, P. DLVO Modeling to Predict Critical Salt Concentration to Initiate Fines Migration Pre-and Post-Nanofluid Treatment in Sandstones. SPE J. 2022, 1–15.
[f] Muneer, R.; Pourafshary, P.; Hashmet, M. R. Application of DLVO Modeling to Predict Critical pH for Fines Migration Pre-and Post-SiO2 and MgO Nanofluid Treatments in Sandstones. J. Fluid Flow, Heat Mass Transf. 2022, 9 (1), 106.

controlling fines migration.[76] Assef et al. used MgO NPs to mitigate colloidal particle movement, achieving 97% retention of fines using the extended DLVO (X-DLVO) theory.[188] Zou et al. applied X-DLVO theory to study anionic polyacrylamide adsorption onto coal and kaolinite particles, showing repulsive interactions between kaolinite and coal particles after polymer adsorption, demonstrating coal purification efficacy.[189]

Similarly, in sandstone reservoirs, the migration of fines can be greatly influenced by the pH level of the injection water. Moreover, the pH of the SFB system may rise after water injection due to the solubilization and dissolution of rock minerals such as calcite and siderite. This has a considerable impact, particularly in the processes of alkaline flooding and waterflooding, on the release of fine particles in sandstones above a specific pH called a critical pH. The release of fines, because of an increase in the system pH, can be attributed to an increase in the repulsive forces and can be modeled using the DLVO approach.[190] The application of nanoparticles in the form of nanofluids provided promising results in controlling fines migration, reducing the CSC, and improving the critical pH. The DLVO models effectively incorporated the effects of silica nanoparticles, and all model results were validated experimentally.

4.2 Materials and Methods

This work is divided into two phases. Initially, surface interactions were modeled using the DLVO theory to predict the CSC and critical pH after nanoparticle application. Subsequently, the developed models were validated experimentally. The materials and methods utilized for each phase are discussed in the following sections.

4.2.1 DLVO Modeling

The objective of employing the DLVO theory in this study was to predict the CSC and critical pH for initiating fines migration in Upper Berea outcrop samples following the application of nanoparticles. The effectiveness of nanoparticles in reducing the CSC, mitigating fines migration in sandstones, and enhancing the critical pH was assessed using the developed DLVO models. To achieve this, the zeta potentials for the sand-NPs-brine system under varying pH were utilized as input for the model, resulting in predictions of reduced CSC and improved critical pH in the presence of nanoparticles.

4.2.2 Nanofluid Preparation

To study the effect of nanoparticles on controlling fines migration, dispersed silica nanoparticles were used in the form of nanofluid. The silica nanoparticles were selected because they are hydrophilic, more stable, less toxic, readily available, and effective in mitigating fines migration in sandstone formations.[48,67,77,78,191,192] The silica nanoparticles were of 20 nm size and obtained from Glantreo Innovative Scientific Solutions Ireland as a concentrated dispersion with a concentration of 25 wt%. This dispersion was diluted by adding 0.15M NaCl brine to prepare 0.05 wt% and 0.1 wt% silica nanofluids.

4.2.3 Zeta Potentials

For sand-NPs-brine zeta potential measurements, the Upper Berea sandstone core sample was crushed and sieved to obtain a fine sand powder. The sand was thoroughly cleaned with n-hexane, acetone, and distilled water, then dried and washed in hydrochloric acid and distilled water until the pH matched the source water. Cleaned sand was dispersed in 0.05 wt% and 0.1 wt% silica nanofluids using a magnetic stirrer and ultrasonic homogenizer. Zeta potentials were measured with a Malvern Zetasizer after 24 hours of equilibration to ensure sufficient interactions between particles.

4.2.4 Coreflood Tests

Coreflood tests were conducted to estimate the reduction in CSC after the application of nanoparticles. Two corefloods were designed with the injection sequence given in Table 4.1. A soaking period of 15–24 hours was provided after each injection stage to achieve equilibrium and ensure sufficient contact between the injected brine, fine particles, sand surface, and nanoparticles where used.

Table 4.1 Injection sequence for coreflood tests.

Test No.	*Injection Design*
1	0.15M NaCl →15 hrs. soaking → 0.05 wt% SiO_2 NF → 0.1M NaCl → 0.09M NaCl → 0.08M NaCl→ 0.07M NaCl → 0.06M NaCl
2	0.15M NaCl →15 hrs. soaking → 0.1 wt% SiO_2 NF → 0.1M NaCl → 0.09M NaCl → 0.08M NaCl → 0.075M NaCl → 0.07M NaCl

In the first experiment, a 0.05 wt% silica nanofluid was injected into the core sample at a rate of 0.02 cc/min for 5–6 PVs. This was necessary to provide sufficient time for the silica nanoparticles to be in contact with the sand and fines surface and alter the

surface properties. Afterward, the injection of nanofluid was stopped and 24 hours of soaking time was given. The reduced CSC was then determined by successively injecting brines having ionic strength below CSC, giving 15 hours of soaking time at each step and again flooding with the same brine for a couple of PVs until the production of the fines was observed in the effluent. The same steps were followed in the second test with the only difference in the nanofluid concentration. 0.1 wt% silica nanofluid was used in this experiment and the reduced critical salt concentration was experimentally determined. Experiments were conducted to determine the CSC with and without NPs. By knowing the actual CSC, it would be clear at what salinity the total surface force shifts from attractive to repulsive. The experimental results were then used to validate the DLVO modeling results.

4.2.5 Effluent Analysis

Effluents from coreflood tests were analyzed for fines using turbidity and UV-VIS Spectrophotometer. The CSC after the application of nanoparticles was determined based on the sudden increase in effluent turbidity. Higher absorbance values confirmed fines presence, validating DLVO models for nanotechnology effectiveness.

4.3 Results and Discussion

4.3.1 Zeta Potential Measurements

Using a magnetic stirrer and an ultrasonic homogenizer, clean and washed sand particles were dispersed in silica nanofluids, and the zeta potentials were measured for each case. The application of nanofluids decreases the repulsion between fine particles and sand grains which results in increased zeta potential corresponding to the contracted electric double layers around sand grains and fine particles. The measured zeta potentials are given in Table 4.2.

Table 4.2 Measured zeta potentials with nanofluid.

NaCl Salinity (M)	*Measured Zeta Potential after 0.05 wt% Nano (mV)*	*Measured Zeta Potential after 0.1 wt% Nano (mV)*
0.10	-28.2	-27.0
0.09	-28.5	-27.3
0.085	-28.9	-27.5
0.08	-29.0	-27.7

0.075	-29.1	-28.1
0.07	-29.1	-28.2
0.06	-29.4	-28.5
0.05	-30.5	-28.6

The zeta potentials of dispersed sand particles were measured before and after the application of SiO_2 nanofluid as shown in Table 4.3. As the pH of the solution increases, the electric double layer expands, and the corresponding zeta potential decreases. On the other hand, the application of silica nanoparticles decreases the expansion of the EDL and increases zeta potential. To further assess the effects of pH level changes in a high-salinity system, consisting of crushed sandstone grains with kaolinite particles and a 0.2M solution of 8 wt% NaCl with 2 wt% $CaCl_2$, zeta potential data were collected from relevant literature. Moreover, the zeta potential data for 0.0075wt% MgO nanoparticles were also obtained from the literature.

Table 4.3 Measured and collected zeta potential data with NPs.

Medium and ionic strength	*pH*	*Zeta with NPs*	*Source*
0.2M NaCl, and with 0.1wt% SiO_2 NPs	2	-3	Measured by Zetasizer with a titrator
	3	-7	
	4	-10	
	5	-12	
	6	-14.5	
	7	-16.1	
	8	-18.6	
	9	-20.2	
	10	-21.9	
	11	-23.7	
	12	-24.9	
0.02 M NaCl with 0.0075wt% MgO NPs	9	-1.5	Assef et al. [188]
	10	-8.2	
	11	-9.1	
	12	-9.7	

4.3.2 DLVO Modeling for Nanofluid Application to Predict CSC

Silica nanoparticles adsorb on the surface of sand grains via nanofluid, changing the surface potential and increasing the system's attractive potential by reducing repulsive forces. A DLVO model with 0.05 wt% (500 ppm) silica nanofluid and NaCl brine salinity descending from 0.1M to 0.05M was prepared using the measured fine particle size,

measured zeta potentials, and calculated Hamaker constant for the given system. It is evident from Figure 4.1 and Table 4.4 that the total interaction energy of the system shifts from negative to positive at a salinity of 0.085M NaCl, corresponding to an increase in Debye length from 0.96 to 1.05 nm. Therefore, the electric double layers around the fine particle and sand grain have expanded and overlapped each other under low salinity conditions of 0.085M, causing increased repulsive forces and generating an energy barrier of 0.11 V_T that dominated the attractive forces. In addition, decreasing the salinity from 0.08M to 0.05M caused a further increase in Debye lengths and strong repulsion, with the given potential barriers in Table 4.4.

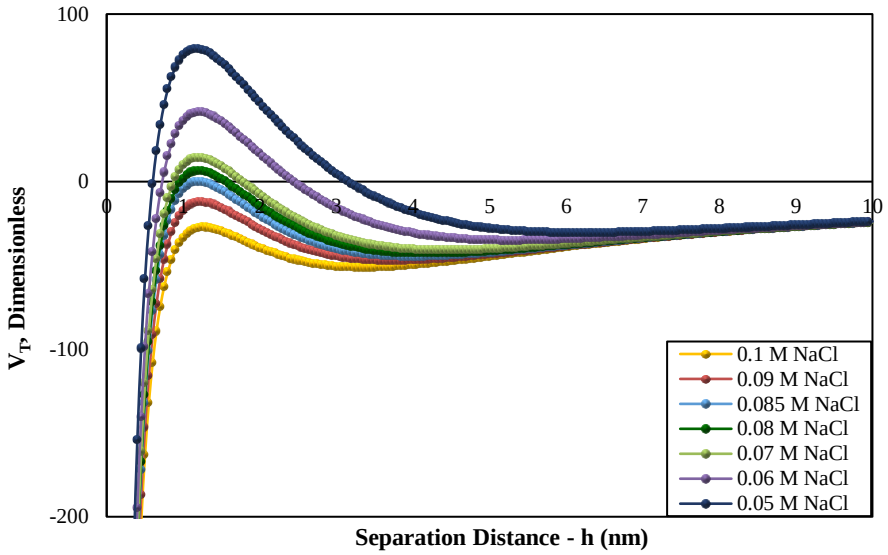

Figure 4.1 DLVO model showing the effectiveness of 0.05 wt% silica nanofluid.

Table 4.4 The Debye length and potential barriers post 0.05 wt% nanofluid treatment.

Salinity (M)	k^{-1} *(nm)*	$V_{T_{Maximum}}$	$V_{T_{Barrier}}$
0.1	0.97	-27.03	--
0.09	1.02	-11.91	--
0.085	1.05	0.11	0.11
0.08	1.08	3.75	3.75
0.07	1.16	14.56	14.56
0.06	1.25	49.64	49.64
0.05	1.37	79.47	79.47

The DLVO model predicted a 23% reduction in CSC following the application of 0.05 wt% silica nanofluid and a new CSC was forecasted to be 0.085M NaCl brine. The

increase in the attractive surface potential was attributed to the adsorption of silica nanoparticles onto sand grains which caused fine particles to firmly attach to the rock surface in even a reduced salinity environment. The increased zeta potential value indicated a reduction in repulsive surface forces of sand grains, which eventually controlled the fines migration in the sand-fine-brine system.

To analyze the effect of the nanoparticles concentration on controlling fines migration, another DLVO model was developed with 0.1 wt% (1000 ppm) silica nanofluid considering the similar case of NaCl brine with a gradually decreasing salinity from 0.1M to 0.05M as shown in Figure 4.2. Silica nanofluid of 0.1 wt% proved to be more effective because it reduced the CSC by 32% compared to the base case, and the DLVO model predicted it to be 0.075M NaCl brine. The attractive energy shifted to repulsive in a 0.075M brine environment with a barrier of 0.10 V_T, as shown in Table 4.5. These findings are explained by the high concentration of nanoparticles in the nanofluid, which caused a higher silica nanoparticle adsorption on the sand surface, resulting in a strong attraction that kept fine particles in the system.

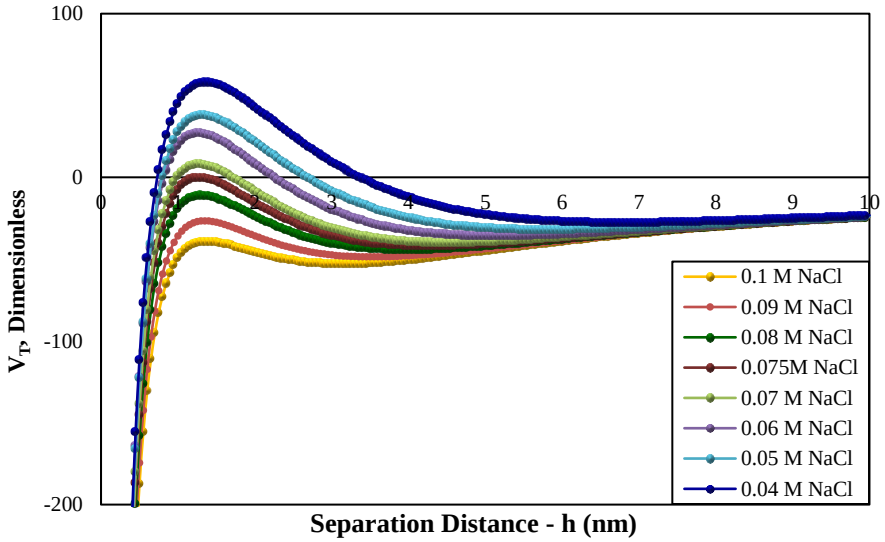

Figure 4.2 DLVO model showing the effectiveness of 0.1 wt% silica nanofluid.

Table 4.5 The Debye length and potential barriers post 0.1 wt% nanofluid treatment.

Salinity (M)	k^{-1}*(nm)*	$V_{T_{Maximum}}$	$V_{T_{Barrier}}$
0.1	0.969	-38.97	--
0.09	1.02	-26.41	--
0.08	1.08	-10.88	--

0.075	1.12	0.10	0.10
0.07	1.16	6.89	6.89
0.06	1.25	27.33	27.33
0.05	1.37	38.13	38.13

4.3.3 Effect of SiO_2 Nanofluid on Critical pH

The surface forces between fines and sand grains were quantified using zeta potentials under different pH conditions with the utilization of 0.1 wt% SiO_2 nanofluid, brine ionic strength, and average fine particle size, and the total interaction energy of each system was calculated using DLVO modeling, as shown in Figure 4.3. By altering the surface charge of sand grains, silica nanoparticles assisted in limiting the expansion of electric double layers in high pH environments. Forces of attraction dominate repulsion forces in the presence of compacted electric double layers around fines and sand grains in the pH range of 6-10, and the total energy is negative without any fines migration in the system. The overall interaction energy shifted from negative to positive for brine with pH=11, suggesting the dominance of repulsive forces in the system. This occurs because of nanoparticles' adsorption on the surface of the sand grains, which causes the electric double layers to contract even under higher pH values. The results of the DLVO model indicated that pH 11 would be the new critical pH, and it was projected that fines migration in the SFB system would take place at this value or higher after the application of SiO_2 nanofluid.

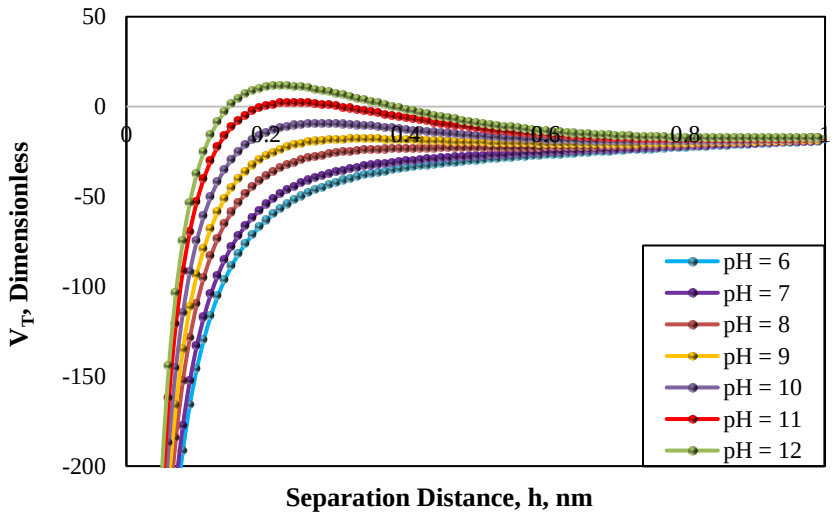

Figure 4.3 Prediction of a new critical pH after the application of SiO_2 nanofluid.

4.3.4 Effect of MgO Nanofluid on Critical pH

The zeta potential data obtained from Table 4.3 for a 0.0075 wt% MgO nanofluid with different pH values were utilized to construct the DLVO model. This was done to determine the critical pH value and to compare it with the case of SiO_2 nanofluid. The surface forces between fines and sand grains were measured using zeta potentials at various pH levels with MgO nanofluid, brine ionic strength, and average fine particle size, and the total interaction energy of each system was computed using DLVO modeling, as shown in Figure 4.4. It is noticeable that forces of attraction outweigh forces of repulsion when compacted electric double layers are present surrounding fines and sand grains in the pH range of 9 to 11, and the total energy remains negative with no fines migration in the system. However, for brine with pH=12, the total interaction energy changed from negative to positive, indicating that repulsive forces dominated the system. As predicted, fines migration in the SFB system would occur at pH 12 or higher after the application of 0.0075 wt% MgO nanofluid, according to the results of the presented DLVO model.

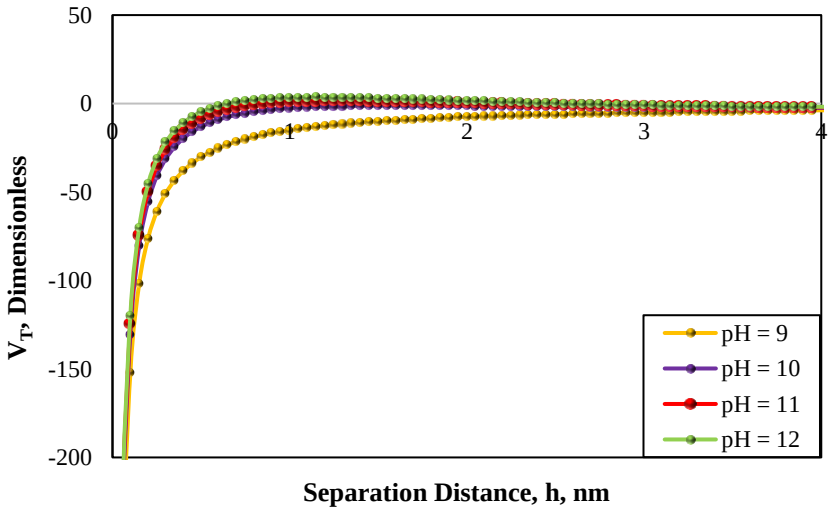

Figure 4.4 Prediction of a critical pH after the application of MgO nanofluid.

4.3.5 Experimental Validation of Silica Nanofluid Application

The first coreflood was performed to validate the DLVO prediction after the application of nanofluid. The formation water-saturated core was first flooded with 3 PVs of 0.15M NaCl brine, and an average turbidity of 0.72 NTU was measured with a stable pressure drop. Later, 6 PVs of a designed nanofluid (0.05/0.1 wt% silica nanoparticles +

0.15M NaCl brine) were injected at the lowest rate of 0.02 cc/min, providing maximum contact time for the nanoparticles to adsorb on sand grains and fine particles. 24 hours of soaking was also provided to ensure proper interaction between the nanoparticles and rock to change the surface potential of the sand grains. After the adsorption of silica nanoparticles and soaking period, a flooding sequence of post-nanofluid treatment was started with 0.1M NaCl brine injection, and 3 PVs were injected at 0.2 cc/min following a 15-hour soaking period. Following the same methodology, the injection was continued in steps with 0.09M and then 0.08M NaCl brines, measuring stable pressure drops with low turbidities. However, when the injection of 0.08M NaCl brine was resumed after the soaking period, pressure fluctuations and an increased pressure drop were observed as shown in Figure 4.5. The effluent collected for the 21st PV showed the first peak of turbidity, indicating that the critical salt concentration was between 0.09M and 0.08M NaCl, which is in agreement with the DLVO estimation (0.085M). To verify the fines detachment under the 0.08M salinity condition, the next injection was carried out with 0.075M NaCl brine, and after the soaking period, the turbidity and absorbance reached even higher values, confirming that fines migration had already been initiated under 0.08M salinity injection as shown in Table 4.6.

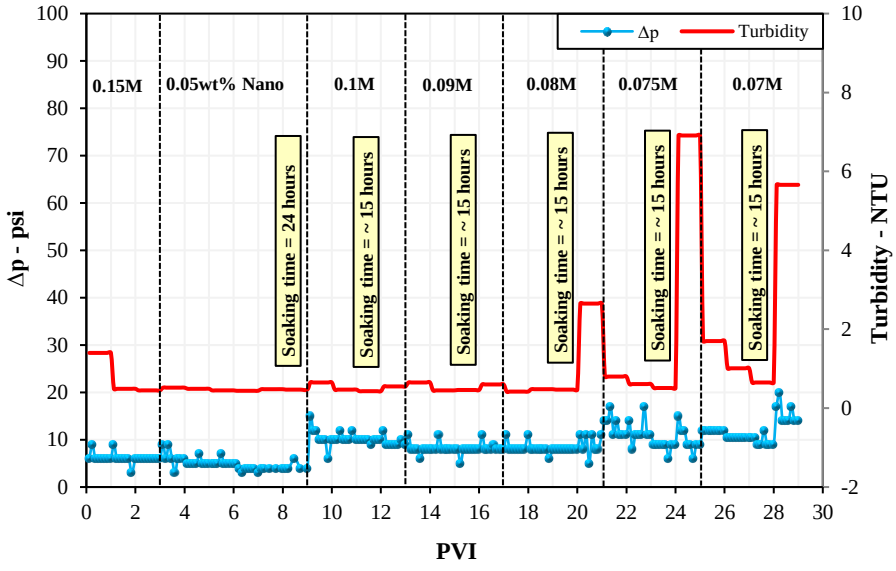

Figure 4.5 Pressure drop and effluent turbidity results show a reduction in CSC after 0.05 wt% nanofluid application.

The second coreflood was run with the same flooding sequence as in the previous

test, with the only difference in the concentration of silica nanoparticles, which was 0.1 wt% in this case. The turbidities and pressure drop against each PV were measured and are presented in Figure 4.6. The turbidity and absorbance values for each flooding stage are given in Table 4.6. Based on the high turbidity and absorbance values and pressure drop fluctuations, the new reduced CSC after 0.1 wt% nanofluid treatment was found to be between 0.08M and 0.07M NaCl, showing a 9% greater reduction compared to the case with 0.05 wt% NPs. The experimental critical salt concentration was found to be in close agreement with the DLVO model's predicted CSC of 0.075M NaCl.

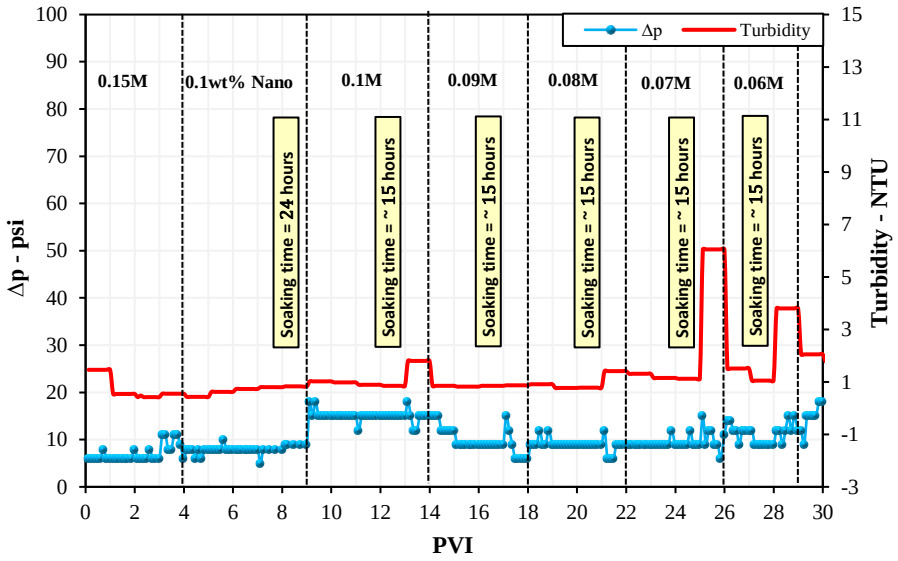

Figure 4.6 Pressure drops and effluent turbidity results show a reduction in CSC after 0.1 wt% nanofluid application.

Table 4.6 Effluent turbidity and absorbance analysis for estimation of CSC post-NF treatment.

NPs Concentration (wt%)	*Salinity (M)*	*Turbidity (NTU)*	*Absorbance (ABS)*
0.05	0.15	0.52	0.153
	0.10	0.55	0.086
	0.09	0.60	0.088
	0.08	2.65	0.105
	0.075	6.91	0.251
	0.07	5.66	0.198
0.1	0.15	1.46	0.167
	0.10	1.80	0.136
	0.09	0.87	0.089
	0.08	1.41	0.176

	0.07	6.05	0.214

4.4 Summary

- This research focused on the use of silica nanoparticles, but our proposed method is equally applicable to other types of nanoparticles. The measurement of zeta potential will differ because different nanoparticles have different charges and the ability to change the surface potential of sand grains.
- Based on the quantification and analysis of surface forces of attraction and repulsion between fine particles and sand grains, the concept of DLVO modeling was applied in the presence of silica nanoparticles, and it predicted the CSCs of 0.085M (4900 ppm) and 0.075M (4400 ppm) NaCl for 0.05 wt% and 0.1 wt% nanofluid treatments, respectively, showing the effectiveness of nanoparticles in reducing the repulsion forces.
- In comparison to the case without nanofluid, the use of silica nanofluid increased the zeta potential (more positive) of sand grains, resulting in less repulsion between fines and sand. As a result, the critical salt concentration was reduced by 23 to 32%.
- Coreflooding was performed systematically, with the effluent collected after each pore volume. The predictions of the DLVO models have been validated experimentally through turbidity and spectrophotometry analysis of effluents, and this tool can be used to estimate the CSC without requiring extensive coreflood experiments.
- In addition, after the application of 0.1 wt% SiO_2 nanofluid, the DLVO model predicted a new critical pH of 11. The DLVO model predicted a new critical pH of 12 after the application of 0.0075 wt% MgO nanofluid. Even at extremely low concentrations, MgO nanofluid application was shown to be more effective than SiO_2 nanofluid application.
- The DLVO approach can model the CSC and critical pH and explain how nanoparticles effectively reduce repulsive forces and therefore limit fines migration.

CHAPTER 5: Development of an Updated DLVO Model for High-Rate Fluid Flow in Sandstone Reservoir

Fines migration causes formation damage in sandstone reservoirs and water-bearing subsurface formations. Several factors affect fines migration such as composition and salinity of permeating brine, flow rate, and system pH. Electrostatic forces of van der Waals attraction and electric double-layer repulsion, and gravitational force all contribute to the detachment of fines and migration under certain conditions. On the other hand, hydrodynamic force plays an important role in a high flow rate injection or production operations and can trigger fine migration. An integrated model of electrostatic, gravitational, and hydrodynamic forces has been developed to estimate the critical injection rate of NaCl brine for fines migration initiation in subsurface formations. The DLVO modeling approach was modified by considering electrostatic, hydrodynamic, and gravitational forces. Parameters such as injection brine salinity, average fine particle size, and zeta potential of sand-brine systems were used, and effective forces were quantified. A microscopic force and torque balance approach was applied to model hydrodynamic forces to modify the DLVO model. The developed models were validated with experimental results. The profiles of injection velocity versus fine particle radius were generated and the models predicted critical flow rates of 0.9, 2.6, and 3.8 cc/min for 0.15 M, 0.2 M, and 0.25 M NaCl, respectively. For model validation, the coreflood experiments were performed on Berea sandstone core samples under given salinities, and critical flow rates were determined. Comparable experimental results were obtained with critical flow rates of 1, 3, and 4 cc/min for 0.15 M, 0.2 M, and 0.25 M NaCl, respectively. In addition, sensitivity analysis assesses the impact of different forces on the fines migration phenomenon. Regulating the injection/ permeating fluid rate and salinity can avoid fines migration and associated permeability impairment. The following sections present a novel approach incorporating electrostatic, gravitational, and hydrodynamic forces to accurately predict fines mobilization in fine-containing subsurface formations. This chapter is based on the results published in the referenced article[g].

[g] Muneer, R.; Pourafshary, P.; Hashmet, M. R. An Integrated Modeling Approach to Predict Critical Flow Rate for Fines Migration Initiation in Sandstone Reservoirs and Water-Bearing Formations. J. Mol. Liq. 2023, 121462.

5.1 Introduction

Based on the formation and composition of these porous and permeable rocks, fine particles are present and remain in equilibrium under the formation water environment. The electric double layers around fine and sand grains contract as a result of the high charge density in the sand-find-brine system, keeping the fine particles in equilibrium in a high salinity environment.[193] However, this equilibrium is disturbed and fines migration is triggered when the formation water salinity goes below a threshold value known as a CSC, system pH rises above a critical pH value, and injection/production or permeating fluid rate exceeds the critical rate.[116] In sandstone petroleum reservoirs, formation water salinity is reduced or pH is increased by injecting low salinity water, or high pH water during waterflooding and alkaline flooding processes, respectively. On the other hand, in aquifers, salinity may reduce due to recharging with fresh water, and pH may increase owing to in-situ chemical reactions caused by minerals.[194]

Adhesion and hydrodynamic forces produce torques on fine particles that are attached to the rock surface. The adhesion forces between particles and the rock surface include electrostatic and gravity forces. The electrostatic forces include van der Waals attraction and electric double-layer repulsion force. The flow rate of injection fluid controls the hydrodynamic forces, while the particle and permeating fluid densities control the gravity forces. Water injection in petroleum and geothermal reservoirs may cause in-situ fines detachment from the rock surface under the shearing effect of injection fluid. Particularly in reservoirs with weak cementation, the unequal torques may cause pore blockage and reduce formation permeability.[68] Ochi et al. looked into the impact of flow rates on fines migration and found that there is a threshold fluid velocity above which permeability reduces due to the detachment of fine particles. They deduced from their observations that formation permeability was influenced by injection velocity.[69] Bedrikovetsky et al. utilized the concept of maximum retention and successfully modeled it considering the effect of injection fluid velocity. Their model showed that after raising the fluid velocity to a threshold level, particles might be quickly dislodged from the sand surface. Conversely, lowering the velocity results in a greater retention concentration up to a maximum owing to given hydrodynamic conditions.[70] Numerous imaging studies carried out on the synthetic core of glass beads have supported the velocity-dependent fines

detachment. The shearing force increases with velocity, and particle detachment and mobilization may happen when hydrodynamic force is greater than adhesion forces.[71–73] Despite the imposed flow rate causing a hydrodynamic shearing exceeding the critical threshold, Torkzaban et al. determined that a single layer of attached fine particles is partly removed rather than fully. Due to the variability of pore structure, surface charge, and roughness, hydrodynamic and adhesion forces vary spatially.[74]

For injection at low rates and below the critical rate, the effect of the electric double-layer repulsion force is more dominant to initiate fines migration. Therefore, as all previous models were developed at low rates, the effect of hydrodynamic force was neglected. However, at higher rates, hydrodynamic force plays a significant role in detaching the fines from the rock surface. In this context, the conventional DLVO approach is not valid at high rates and does not incorporate the effects of hydrodynamic force. This chapter presents a novel integrated model considering electrostatic and hydrodynamic forces and predicts critical rates for different salinity NaCl brines. The new model was validated with experimental critical rates and comparable results were obtained.

5.1.1 Fines Detachment Model

Figure 5.1 depicts a schematic of a fine particle on a sand grain, together with the drag, lift, gravitational, and effective electrostatic forces that are at play. A microscopic force balancing method works with forces and torques acting on a particle depending on the configuration. The hypothesis states that if electrostatic and gravitational forces prevail over hydrodynamic forces, a fine particle will remain attached to the sand grain. On the other hand, if the overall electrostatic force holding a particle close to a surface is less than the hydrodynamic shear, the particle is mobilized by the flow.[195–199] As a result, the migration and deposition of a single colloid rely on the equilibrium between the forces of attraction and repulsion acting on it. Various studies used the microscopic force balancing method extensively to forecast the deposition and migration of fine particles.[200–203] As depicted in Figure 5.1, a single particle will remain attached to the sand surface until the attaching torques are balanced out by the ones required to detach it. The fine particle may be mobilized by the drag force when there is a decrease in ionic strength and an increase in corresponding electrostatic repulsion.

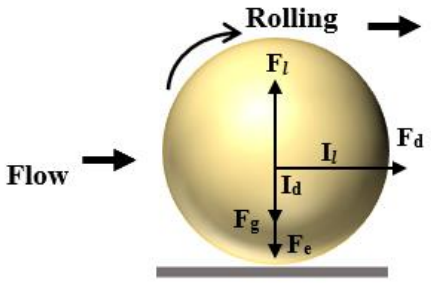

Figure 5.1 Schematic of acting forces and moment arms of a single particle on the sand surface.

The torque balance is shown in Equation 5.1 where drag, lift, gravitational and electrostatic forces, as well as an external moment of viscous stress "M_d", are taken into account.[197,204,205]

$$F_d I_d + F_l I_l + M_d = \left(F_g + F_e\right) I_l \tag{5.1}$$

$$\therefore I_d = r_s, \quad and \quad I_l = r_f$$

The forces F_d, F_l, F_g, and M_d are given by Equations 5.2-5.5, respectively.[71,206–208]

$$F_d = 1.7009 \times 6\pi\mu r_f v_s \tag{5.2}$$

$$F_l = 81.2\sqrt{\rho\mu}\left(r_f v_s\right)^{1.5} \tag{5.3}$$

$$F_g = \frac{4}{3}\pi r_f^3\left(\rho_f - \rho\right)g \tag{5.4}$$

$$M_d = 0.943993 \times 8\pi\mu r_f v_s \tag{5.5}$$

and,

$$v_s = 2v\left(1 - \frac{\left(r_p - r_f\right)^2}{r_p^2}\right) \tag{5.6}$$

Incorporating Equations 5.2-5.5 in Equation 5.21 and replacing I_d and I_l with "r_s" to get Equation 5.7.

$$1.7009 \times 6\pi\mu r_f v_s I_d + 81.2\sqrt{\rho\mu}(r_s v_s)^{1.5} I_l + 0.943993 \times 8\pi\mu r_s v_s = \left(F_g + F_e\right) I_l$$

$$10.21\pi\mu v_s {r_f}^2 + 81.2\sqrt{\rho\mu}\left(r_f v_s\right)^{1.5} r_f + 7.55\pi\mu r_f v_s = \left(F_g + F_e\right) r_f \tag{5.7}$$

Given the conditions that fine particles will detach and move when the injection velocity exceeds the critical velocity, as shown in Equation 5.8.

$$10.21\pi\mu r_f v_{s,crit} + 81.2\sqrt{\rho\mu}\left(r_f v_{s,crit}\right)^{1.5} + 7.55\pi\mu v_{s,crit} > F_g + F_e \tag{5.8}$$

When the injection velocity is low, the lift force is relatively insignificant in comparison to the drag force. In this case, Equations 5.6 and 5.7 are used to derive the final model presented in Equation 5.9, which is used to generate velocity profiles for brines with different salinity. The derivation of Equation 5.9 is given in Appendix -A.

$$v = \left(F_g + F_e\right)\left[\frac{2r_f\left(2r_p - r_f\right)\left(17.76\pi\mu r_f\right)}{r_p^2}\right]^{-1} \tag{5.9}$$

When the salinity is less than CSC, the electric double layer repulsion becomes significant and fines migration starts even at a low rate indicating the hydrodynamic force is insignificant. However, at high rates, the hydrodynamic force becomes significant and fines migration begins in the porous medium even at salinity above the CSC. Equation 5.9 presents an integrated model that incorporates the effect of hydrodynamic, effective electrostatic, and gravitational forces.

5.2 Materials and Methods

The materials and methods used have been discussed in the following sections.

5.2.1 Berea Sandstone Sample Preparation

To estimate the critical flow rate for NaCl brines in sandstone reservoirs, Berea sandstone outcrop samples containing fine particles were used. Three core samples in total were cut, each with a diameter of 3.8 cm and an average length of 7.6 cm. The cores were saturated with 77000 ppm formation water with a manual saturator provided by Vinci Technologies after the dry weights were measured. After the core saturation, porosities were determined by measuring the wet weight of each sample. The average porosity of the core samples was in the range of 19.4–19.5%.

5.2.2 Brines

To determine the experimental critical velocity/ flow rate, injection brines of 0.15 M, 0.2 M, and 0.25 M NaCl were prepared. To make the brines, reagent-grade sodium

chloride (NaCl) supplied by Sigma Aldrich was combined with the required quantity of distilled water and stirred with a magnetic stirrer. For the experimental phase of the research, core samples were saturated with formation water (FW) that had a salinity of 77,000 ppm. To prevent precipitation and contamination, the brines were kept in airtight containers. Table 5.1 shows the composition and concentration of formation water as well as each injection brine.

Table 5.1 Composition and concentration of formation water and injection brine.

Ions	*FW*	*NaCl injection brines*		
		0.25M	*0.2M*	*0.15M*
	[ppm]			
Na^{+}	23426	5747	4596	3447
Ca^{2+}	4448	-	-	-
Mg^{2+}	1300	-	-	-
Cl^{-}	47781	8863	7093	5320
Total	76955	14610	11693	8770

5.2.3 Zeta Potential Measurements

The Zeta potential of sand grains is one of the key input parameters for DLVO modeling. The cleaned sand was then dried and mixed in the various molarity brines listed in Table 5.1 using a magnetic stirrer for 30 minutes and an ultrasonic homogenizer at 70% power for 45 minutes. A Malvern Zetasizer was used to measure the zeta potential of each sample after the sand particles had been properly dispersed in the given brines.

5.2.4 Integrated Fines Detachment Modeling

An integrated fines detachment model was developed incorporating hydrodynamic, electrostatic, and gravitational forces, as presented in Equation 5.9. The derivative of potential energy with respect to separation distance is equal to the force. Therefore, the derivative of Equations 2.4 and 2.10 from Chapter 2 with respect to separation distance converted potential energy into force and the summation of attraction and repulsion forces was the effective electrostatic force (F_e) acting on a fine particle. V_T was converted to F_e so that it could be compared to other forces such as F_g, F_l, and F_d with consistent units. Later, the developed fines detachment model was utilized to generate velocity profiles for brines of different salinity.

5.2.5 Coreflooding Experiments

To validate the integrated model, coreflooding tests were performed. In all the tests, the brine salinity was set above the CSC and each test was started with a low rate of 0.2 cc/min and increased to higher rates in steps until the fine particles were observed in the effluent. Pressure drop data were recorded to observe any pressure changes caused by fines release, mobilization, and production. Furthermore, turbidity measurements were made for each pore volume to confirm the presence of fines in the effluent. Corefloods were conducted to estimate the experimental value of the critical velocity at a specific salinity. A total of three coreflooding tests were designed for different salinities with the increasing injection rates given in Table 5.2.

Table 5.2 Brine injection design for corefloods.

Coreflood No.	*Brine Injection Design*
1	0.15 M NaCl injection at 0.2 cc/min → 1 cc/min → 2 cc/min → 3 cc/min → 4 cc/min → 5 cc/min
2	0.20 M NaCl injection at 0.2 cc/min → 1 cc/min → 2 cc/min → 3 cc/min → 4 cc/min → 5 cc/min
3	0.25 M NaCl injection at 0.2 cc/min → 1 cc/min → 2 cc/min → 3 cc/min → 4 cc/min → 5 cc/min

5.2.6 Effluent Analysis

The effluents collected during coreflooding experiments were tested for the presence of fine particles using two methods. Firstly, for each PV collected, the turbidity was measured using a digital turbidity meter. A UV-visible spectrophotometer was also used to assess the effluents' light absorption to verify the turbidity data.

5.2 Materials and Methods

5.3.1 Zeta Potential Data Measurement and Collection

Zeta potentials of dispersed sand particles in NaCl brine of 0.25 M, 0.2 M, and 0.15 M were measured, as shown in Table 5.3. The measured zeta potentials of the dispersed sand particles were also compared to the developed correlations from our earlier work[178], and the values were observed to be quite close to each other within the permissible error range. The expansion of the electric double layer (EDL), increase in the Debye length, and the corresponding increase in the repulsive force for sand grains are all associated with a reduction in zeta potential values as the salinity of the NaCl solution decreases from 0.25 M to 0.15 M.

Table 5.3 Measured zeta potential data for sand.

NaCl salinity (M)	*Measured zeta potential*	*Zeta potential using correlation*	*Error (%)*
0.25	-27.3	-27.6	-1.1
0.20	-29.5	-28.9	2.0
0.15	-30.6	-30.2	1.3

5.3.2 Fines Detachment Model Results

At low flow rate injection of brine, electrostatic forces control the fines detachment. Surface force models were utilized to estimate the attraction and repulsion surface forces between sand grains and fine particles using the observed zeta potentials for dispersed sand particles, the salinity of each NaCl brine, and the average size of fine particles assessed by SEM. Following this, the total dimensionless interaction energy was estimated for each case using the superposition principle, using Equation 2.3 from Chapter 2, as shown in Figure 5.2. The Debye length and electric double layers were compressed in the high salinity environment of 0.25 M NaCl brine and the van der Waals attraction force exceeded the repulsive forces. As a result, the system's overall interaction energy remained negative, indicating that there had been no fines migration in the sand-fine-brine system. Similar outcomes were observed for 0.2 M and 0.15 M NaCl brines, with the total interaction energy in the negative zone with a slight increase in the Debye length, as shown in Table 5.4. This was because all of these salinities were higher than the CSC for NaCl, which was determined to be 0.11 M NaCl in our previous research.[185] Since total interaction energy (V_T) is in the negative region as illustrated in Figure 5.2 and Table 5.4, there is no potential barrier ($V_{TBarrier}$) predicted by the DLVO model. The potential barrier is the height of total interaction energy in the positive region ($V_T>0$) corresponding to the dominance of repulsion forces in the sand-fine-brine system. It exists when the system salinity is below CSC and the repulsion force exceeds the attraction force. There is no potential barrier when the salinity is above CSC as presented in Figure 5.2. This potential barrier may rise or decrease depending on how the salinity or pH of the injected water affects the surface charge of the sand grains.

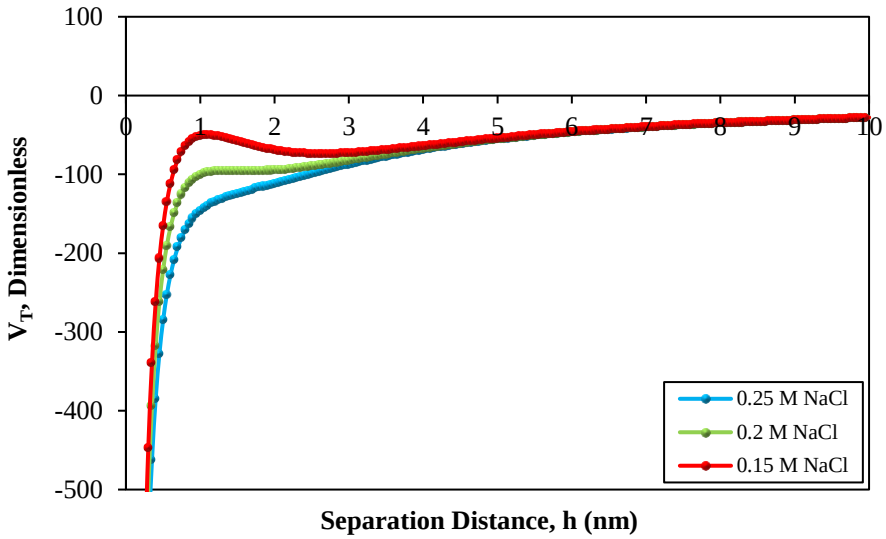

Figure 5.2 DLVO models for different salinities.

Table 5.4 Effect of brine salinity on Debye length and potential barrier.

Salinity (M)	k^{-1}*(nm)*	$V_{T_{Maximum}}$	$V_{T_{Barrier}}$
0.25	0.613	-137.8	Does not exist
0.2	0.685	-93.02	Does not exist
0.15	0.791	-49.49	Does not exist

At higher injection rates, detachment may occur even when the salinity is above CSC, as hydrodynamic force becomes important. Hence Equation 5.9 should be applied as the integrated model to consider both electrostatic and hydrodynamic forces. Table 5.5 provides the estimated effective electrostatic forces for each salinity. It is evident that the effective electrostatic force for 0.15 M is less than 0.25 M, and as a result, increasing the injection rate under a reduced salinity environment would cause fines migration sooner compared to high salinity conditions.

Table 5.5 Relevant parameters for velocity profiles.

Parameters	*Brine salinity (M)*		
	0.25	*0.20*	*0.15*
Effective electrostatic force, F_e (kg-m/s^2)	4.50×10^{-11}	1.80×10^{-11}	1.04×10^{-12}
Brine viscosity, μ (kg/m-s)	0.000965	0.001005	0.001057
Pore radius, r_p (m)	5×10^{-5}		

Using Equation 5.9 and relevant data from Table 5.5, the velocity versus fine particle radius profiles were developed as shown in Figure 5.3. It explains how the fines

detachment velocity varies with fine particle radius and salinity. It is observed that all fines of any size detach easier at lower salinity due to the higher repulsion electrostatic force. Figure 5.3 also shows that more hydrodynamic force is required to detach smaller fines, as the attraction van der Waals force is high. However, the detachment hydrodynamic force becomes high when the fine particle radius is over 1000 nm (1×10^{-6} m) due to the gravitational force. Considering the fine size, the critical velocity can be determined. For instance, for 0.15 M and 0.25 M cases, fine particles of 400 nm (4×10^{-7} m) radius are detached at injection velocities of 1×10^{-3} m/s and 6×10^{-2} m/s, respectively.

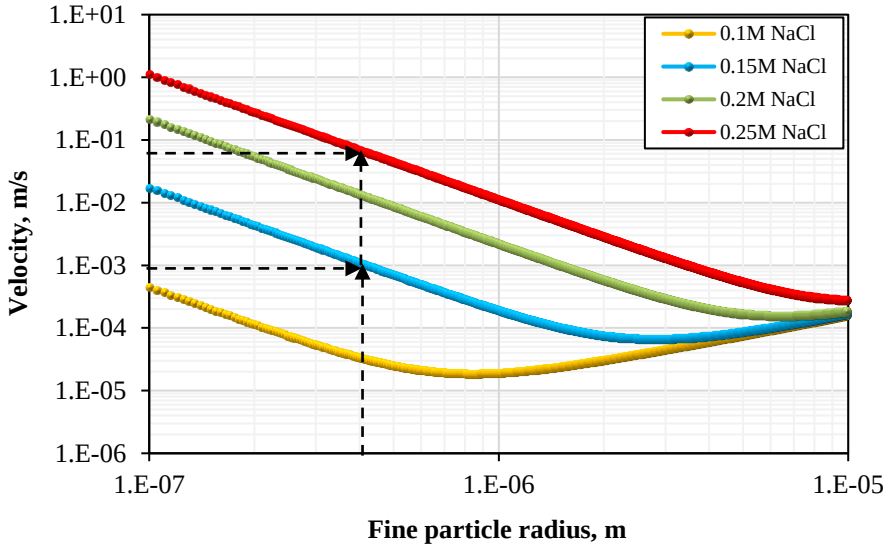

Figure 5.3 Effect of brine salinity on velocity profiles.

5.3.3 Critical Velocity Prediction at Different Salinities

Figure 5.3 has been split and separate results are presented in Figure 5.4 (a-c) for 0.25 M, 0.2 M, and 0.15 M NaCl brines, respectively. For 0.25 M salinity, the critical velocity was predicted to be 3.8 cc/min above which the injection brine velocity line intersected the developed velocity profile suggesting that above this injection velocity, fine particles will detach and migrate in the porous media, as described in Figure 5.4 (a). The velocity profile intersection ($F_d > F_g+F_e$) implies that hydrodynamic forces are greater than electrostatic and gravitational forces in the porous media. The same methodology was applied to 0.2 M and 0.15 M cases, and critical velocity was predicted to be 2.6 cc/min and 0.9 cc/min, respectively, as presented in Figures 5.4 (b) and 5.4 (c). The decrease in critical

velocity was attributed to the expanded electric double layer due to a reduction in salinity from 0.25 M to 0.2 M and onward, resulting in a higher repulsion force. Fine particles of 1700 nm and above would be detached and moved under a salinity range of 0.15 M to 0.25 M NaCl and the corresponding predicted critical rate and critical velocity are given in Table 5.6. The detached fine size distribution at different injection rates is comparable to what is available in the literature.[209,210]

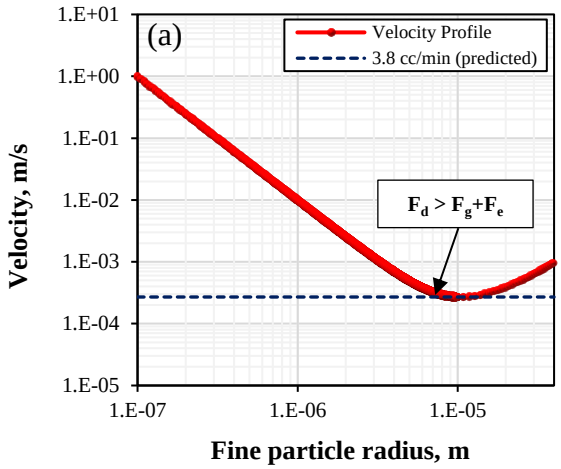

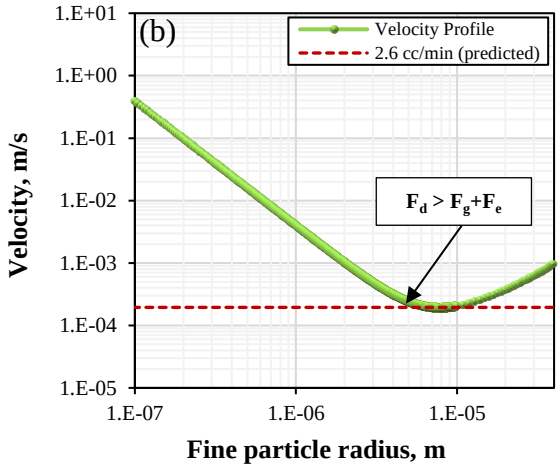

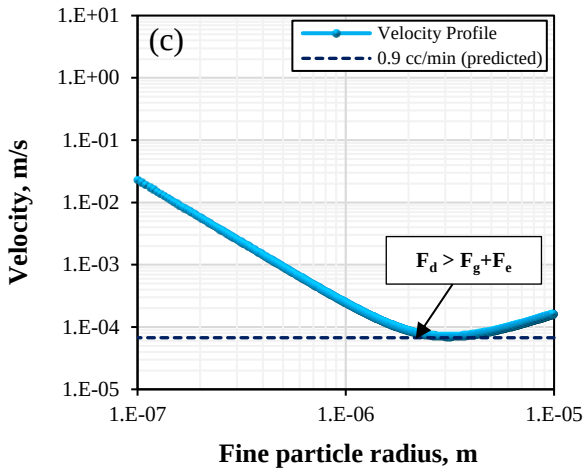

Figure 5.4 Velocity profiles and critical velocity prediction for (a) 0.25 M (b) 0.2 M (c) 0.15 M.

Table 5.6 Predicted critical velocity against each salinity.

NaCl brine salinity (M)	*Critical Injection Rate (cc/min)*	*Corresponding Critical Velocity (m/s)*
0.25	3.8	2.85×10^{-4}
0.20	2.6	1.95×10^{-4}
0.15	0.9	6.74×10^{-5}

5.3.4 Coreflooding Results

Three corefloods were performed on FW-saturated Berea sandstone cores to assess the effect of hydrodynamic forces and to determine the critical velocities based on different brines to validate the developed models. During the first coreflood, three pore volumes (PVs) of 0.25 M NaCl brine were injected at a low rate of 0.2 cc/min, and pressure drop (Δp) across the core was measured with effluent turbidity against each pore volume injected (PVI) as shown in Figure 5.5. The system salinity was reduced from 1.51 M to 0.25 M, and 15 hours of soaking were given to guarantee adequate contact between the injected brine, sand surface, and fine particles for surface potential changes, and to achieve equilibrium between attraction and repulsion forces. After the soaking period, the same 0.25 M NaCl brine was injected at a high rate of 1 cc/min to check the initiation of fines migration in the system due to hydrodynamic forces. For the injection rates of 1, 2, and 3 cc/min, no fines were observed in effluents and the turbidity value remained low. However, when the injection was increased to 4 cc/min, a high-pressure drop with fluctuations was observed, the collected effluent indicated fine particles and turbidity measurement showed a high

value of 75.4 NTU confirming the presence of fines. The results concluded that the 4 cc/min injection rate was a critical rate that triggered fines migration in the porous media owing to increased hydrodynamic forces. Two more corefloods were conducted using the same methodology for salinities lesser than 0.25 M NaCl. The tests were carried out with a step-by-step increase in injection rate, pressure drop, and effluent turbidity were measured. The critical rates were determined to be 3 cc/min and 1 cc/min for 0.2 M and 0.15 M salinity, respectively, as shown in Figures 5.6 and 5.7. Similar to the 0.25 M scenario, at the critical rates, the effluent turbidity spiked confirming the presence of fines triggered by hydrodynamic forces. Based on these results, the developed models were validated with the experimental critical velocities for given salinities, and the results are summarized in Table 5.7.

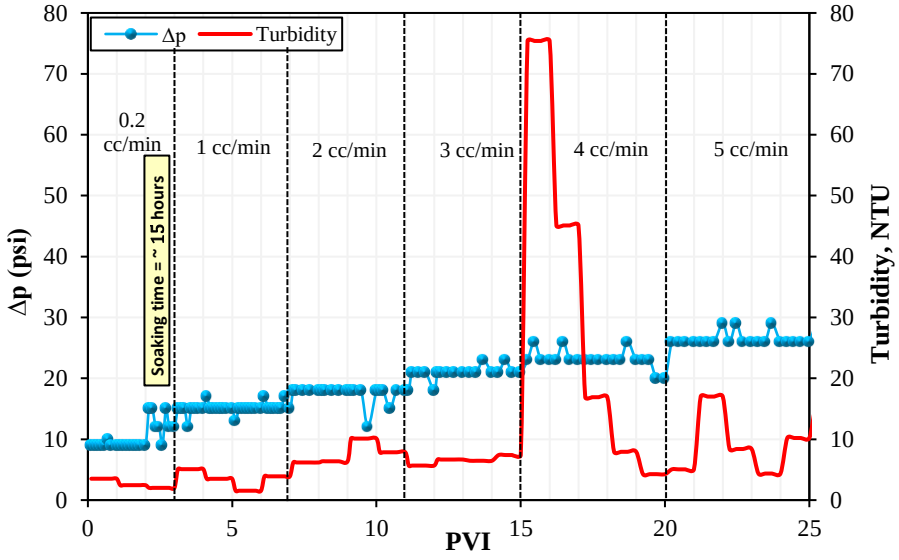

Figure 5.5 Δp and effluent turbidity showing critical rate for 0.25 M NaCl injection.

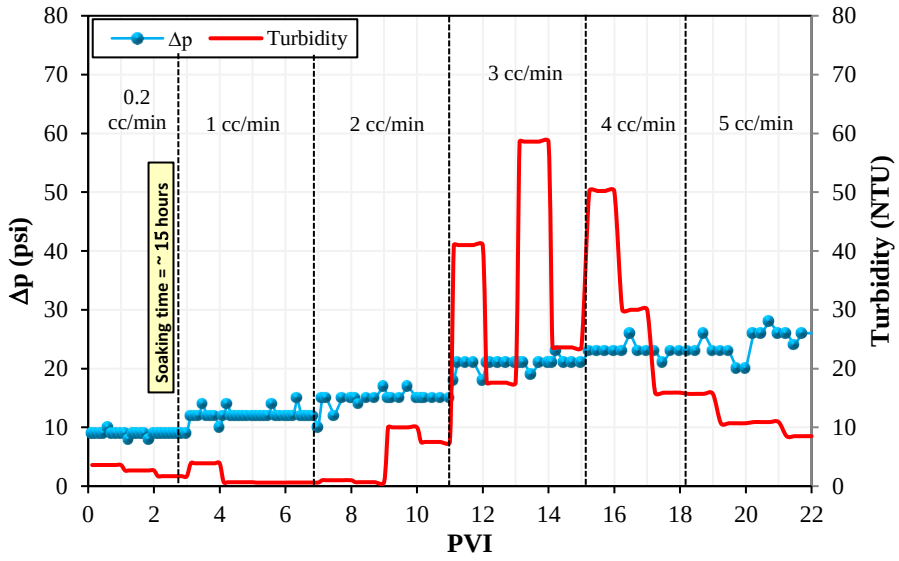

Figure 5.6 Δp and effluent turbidity showing critical rate for 0.2 M NaCl injection.

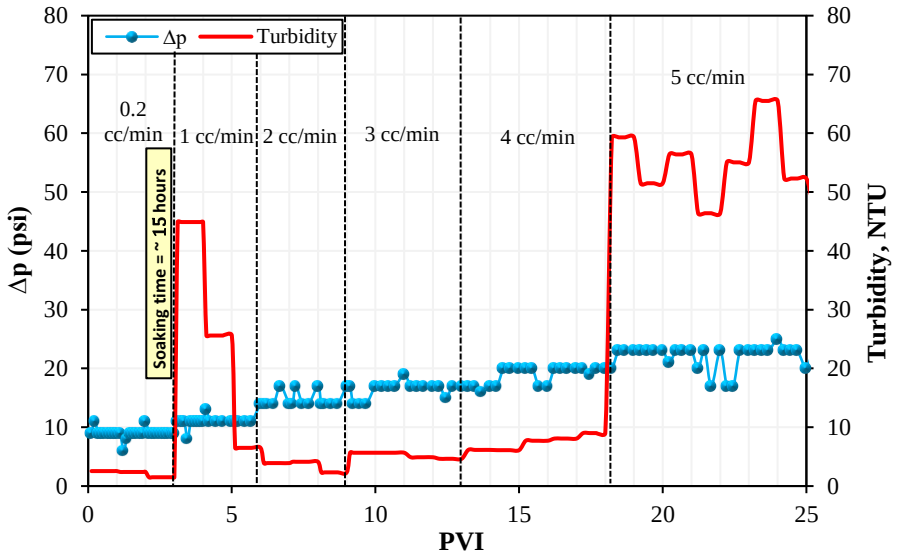

Figure 5.7 Δp and effluent turbidity showing a critical rate for 0.15 M NaCl injection.

During the coreflood tests, the turbidity measurements were carried out for each PV to confirm the presence of fines. Before the critical rate was achieved, the effluent average turbidity remained low and close to the turbidity of the injection brine. However, at the critical rate, the change in pressure drop increased, the effluent turned hazy, and turbidity spiked to a high value indicating the presence of fines. The percentage increase in pressure drop and peak turbidity values at the critical rate for each brine are given in Table 5.7. Furthermore, to validate turbidity results, effluent absorbance was measured using a UV-

vis Spectrometer confirming the presence of fines at given velocities. The experimental critical rates based on coreflood pressure data, effluent turbidity, and absorbance were found in close agreement with the model prediction.

Table 5.7 Effluent turbidity and absorbance analysis for given NaCl brine.

NaCl brine salinity (M)	*Critical Injection Rate (cc/min)*	*Δp change (psi)*	*Turbidity (NTU)*	*Absorbance (ABS)*
0.25	4	10 – 25% increase	75.4	0.377
0.20	3	20 – 40% increase	58.6	0.293
0.15	1	20 – 40% increase	44.9	0.225

5.4 Experimental Validation

Predictions of the critical rate for each salinity using the fines detachment model were validated by coreflood experiments and a close match was found with less than a 10% error. Figure 5.8 with R^2 = 0.9918 indicates an acceptable agreement between model predictions and actual results. Hence, the developed fines detachment model can be used to predict the critical rate for a given salinity.

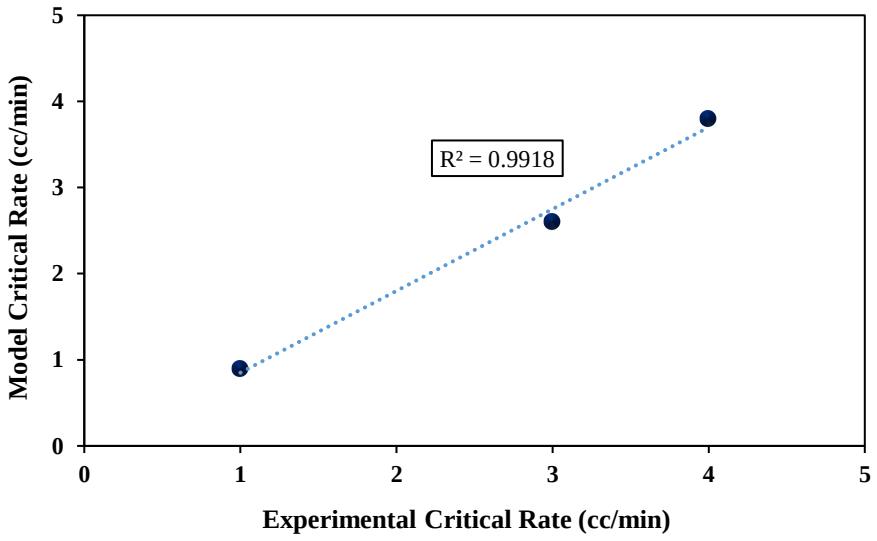

Figure 5.8 Close agreement between model predictions and experimental results.

Inaccurate measurements of input parameters such as injection brine density, viscosity and salinity, zeta potential measurement, and fine particle size might all be sources of error in the model. The accuracy of the model and its predictions depend on the accuracy of the measured input parameters. Brines with the desired level of salinity were

prepared by following the prescribed procedure and using only pure chemicals purchased from Sigma-Aldrich. After that, the density and viscosity of the brine were measured with a calibrated Anton Paar's viscometer, and the salinity was confirmed with a salinity meter. Zeta potentials were measured using the Malvern Zetasizer Nano ZS after preparing sand-brine dispersions following standard procedure. Three measurements were taken for each dispersion to guarantee the data's accuracy, and the model utilized the average value. Furthermore, the average fine particle size was measured using a high-precision Zeiss 540 crossbeam scanning electron microscope. In order to minimize error and get reliable predictions, these accurately measured parameters were employed in modeling.

5.4.1 Limitations of the Model

The fines detachment model is a useful tool for predicting critical flow rate considering NaCl brine, however, it has some limitations, which are given below:

i. The model can forecast the beginning of fines migration in the porous medium, but it is unable to estimate the number of fines that will detach and migrate.
ii. It does not show anything regarding the reattachment of detached fines.
iii. The model cannot predict sudden changes in surface charges and the accompanying surface forces.

5.4.2 Sensitivity Analysis of Affecting Parameters

The velocity profiles presented in Figure 5.3 are dependent on van der Waals attraction, electric double-layer repulsion, hydrodynamic force, and gravitational force. The following section shows the importance of each force under different conditions and the sensitivity of input parameters.

5.4.2.1 Effect of Electrostatic Attraction and Repulsion Forces

Both electrostatic forces of van der Waals attraction and electric double-layer repulsion affect the detachment of fines from the sand surface and critical velocity under high and low salinity conditions, as can be seen in Figure 5.9. The attraction force attaches the fines to the sand surface while the repulsion force tends to detach them. The net effect of these electrostatic forces determines what the critical velocity would be for a given salinity. Figure 5.9 shows that when attraction dominates and repulsion is insignificant in

an extremely high salinity environment, the critical velocity is higher compared to a low salinity case. When the attraction force is significant, the hydrodynamic force of the permeating liquid must overcome the existing force, resulting in a higher critical velocity. However, in a low salinity condition, the dominance of the repulsion force results in a reduced critical velocity. For instance, considering a constant fine particle radius of 400 nm, the critical velocity is predicted to be 1.7×10^{-3} m/s in the presence of a dominating attraction force in a high salinity environment. However, it decreases to 3×10^{-5} m/s in a low salinity environment with substantial repulsion force, as described in Figure 5.9. To avoid underestimating or overestimating the critical velocity, it is essential to take both attraction and repulsion forces into account.

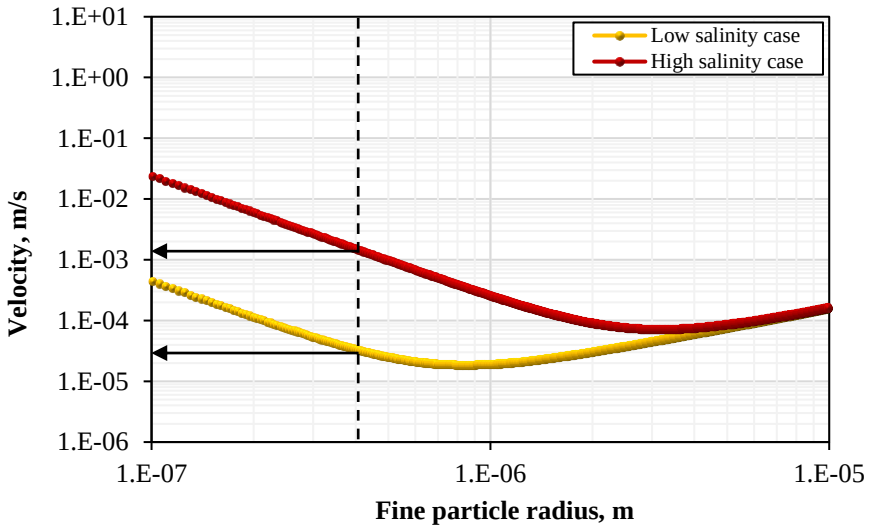

Figure 5.9 Effect of electrostatic attraction and repulsion forces on critical velocity.

5.4.2.2 Effect of Gravitational Force

Gravitational force is another influential parameter in the velocity profile, and it increases with the fine particle radius. Considering Figure 5.10 (a), for the smallest fine particles on the left side, the gravitational force is insignificant, and the velocity profile is governed by effective electrostatic force. The critical velocity decreases gradually in the region where $F_e > F_G$ because the electrostatic forces are decreased as the fine particle radius increases triggering fines migration even at low hydrodynamic force. However, for bigger fine particles, the gravitational force dominates the effective electrostatic force, and the velocity profile shows an upward trend with higher critical velocity in the region where

$F_G > F_e$. The bigger fine particles exert high gravitational force and require higher velocity to move. On the other hand, Figure 5.10 (b) shows a comparison of velocity profiles with and without considering gravitational force with effective electrostatic force. It is observed that the velocity profile neglecting F_G shows a linear trend with a negative slope indicating that bigger fine particles are easy to roll with a low critical velocity. However, this observation does not comply with the theory since bigger fine particles require high drag to move. Therefore, the effect of gravitational force must be included in the velocity profile to achieve realistic and accurate results.

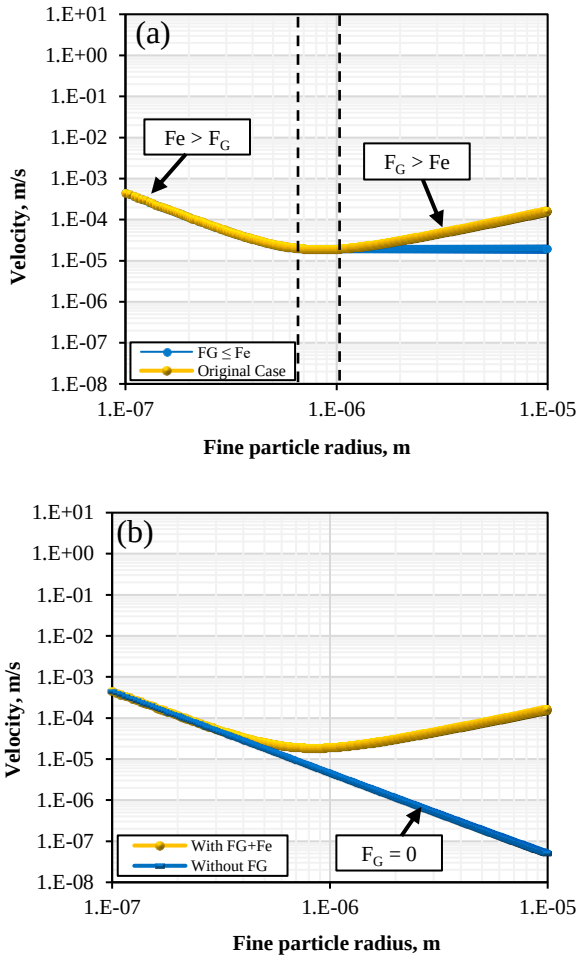

Figure 5.10 (a) Effect of both F_G and F_e on velocity profile (b) for $F_G = 0$.

5.4.2.3 Effect of Pore Radius and Injection Brine Viscosity

Pore radius and injection brine viscosity are also influential parameters and impact velocity profiles are described in Figures 5.11 (a) and (b), respectively. When the pore

radius increases, the velocity profile shifts downward indicating that at a given fine particle radius, the critical velocity will be lower. This is because injection brine can easily flow through larger pores exerting stress on pore walls and available fines resulting in a lower critical velocity. On the other hand, smaller pores have more constrictions requiring extra stress on pore walls, high-pressure drop, and a lower critical velocity, as shown in Figure 5.11 (a). Also, increasing injection brine viscosity shifts the velocity profile downward indicating that extra drag/hydrodynamic stress provided by high viscosity brine may result in a lower critical velocity, as described in Figure 5.11 (b).

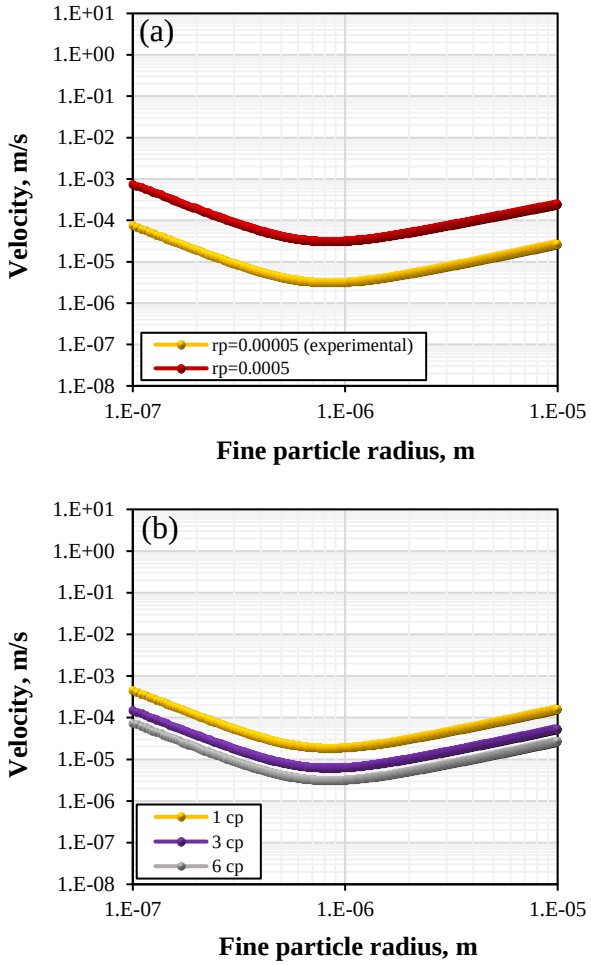

Figure 5.11 (a) Effect of pore radius (b) effect of permeating brine viscosity on velocity profiles.

5.5 Summary

Under certain conditions, fines migration and straining are well-documented problems in sandstone reservoirs and water-bearing formations. In this context, the estimation of critical rate/ velocity is imperative in predicting fines migration and avoiding formation damage.

- Electrostatic, gravitational, and hydrodynamic forces act on fine particles, and a balance among these forces is required to keep fines attached to the rock surface.
- Van der Waals' attraction and gravitational forces keep fine particles attached to the rock surface, whereas electric double-layer repulsion and hydrodynamic forces tend to detach and move them in the porous medium.
- A microscopic balance between attraction and repulsion forces determines the conditions for fines migration initiation based on system salinity and injection rate.
- Under a high salinity of 0.25 M NaCl, the van der Waals attraction force dominates the EDL repulsion force and results in a higher critical rate whereas reduced salinity results in an increased repulsion force and a lower critical rate.
- The developed fines detachment model can predict the critical rate for a specific salinity environment and help avoid fines migration.

CHAPTER 6: Upscaling of Core-Scale Results to Reservoir-Scale

The current chapter presents the upscaling of DLVO modeling and coreflooding results in terms of permeability impairment due to fines migration after the critical salt concentration (CSC) has been reached. In Chapter 2, the DLVO model predicted a CSC of 0.11M for NaCl brine, and the coreflood test validated it with a 40% decline in permeability due to fines migration and straining. An exponential model based on the pressure difference (Δp) from coreflooding and the injection brine salinity (0.2M, 0.15M, and 0.1M NaCl) has been developed. The model predicted the Δp within the acceptable error range of $\pm$10%. The core permeability before and after the soaking period was determined, and the developed exponential model was used to calculate the model permeability (k_{model}). Using experimental data, the skin factor for the core was calculated. For upscaling purposes, it was assumed that the skin factor remained constant for the core and the reservoir. Using the radial Darcy law, pressure profiles as a function of drainage radius were developed for NaCl salinities of 0.2M, 0.15M, and 0.1M, considering the permeability before and after the soaking period to upscale core data to reservoir data.

6.1 Introduction

The decrease in ionic strength and change in ionic composition of formation water may lead to fines migration and permeability reduction in subsurface porous and permeable sandstone reservoirs containing various types of clay minerals. Fines migration has been reported by many researchers to have adverse effects on fluid productivity and injectivity, and their release, migration, and straining can significantly impair the hydraulic connectivity of the reservoir because they plug the actual path for fluid flow.[2,3,17,52,80,178,211] Russell et al. performed several flooding experiments on unconsolidated cores made of silica sand and kaolinite and investigated permeability loss when injection fluid ionic strength decreased from high to low salinity under a constant flow rate. They observed a substantial decrease in permeability from 500 mD to ~20 mD when injection fluid NaCl salinity decreased from 0.6M to 0.0001M.[47] Yu, M. et al. conducted coreflood experiments on sandstone samples and an 80% to 99% reduction in permeability was observed during LSW injection while an increase in pressure drop of 200-250 psi was observed. This translates into a pressure gradient of ~600 psi/ft. Such a high-pressure drop is not practical

on a field scale as it will certainly fracture the rock.[35] In another study performed by Mansouri M. et al., around threefold increase in pressure drop was observed during LSW flooding which was attributed to fines detachment and migration in the sand pack.[48] Similarly, the permeability of Berea sandstone cores was decreased from 120 mD to 0.03024 mD in flooding tests performed by A. Al-Sarihi et al. when the injection fluid was switched from high salinity NaCl to deionized water. This huge decrease in permeability was due to an extremely high-pressure drop across a 05 cm core sample. The fines migration not only causes permeability impairment but also adversely affects the oil recovery during low salinity or alkaline flooding by blocking the pore throats. A considerable increase in pressure drop across the core samples during brine injection is a clear indication of the productivity decline. They also utilized $CaCl_2$ brine to stabilize fines by Ca^{2+} ions and investigated its effect on low-salinity water injection.[33]

Upscaling coreflooding results to reservoir scale brings forth numerous advantages in the field of reservoir engineering and management. The primary benefit lies in its cost-effective nature, as it eliminates the need for extensive and costly field tests while still providing valuable insights into large-scale sandstone reservoir behavior under different salinity injection brines. By utilizing data from laboratory-based coreflooding experiments, engineers can enhance the accuracy of reservoir performance predictions and reduce uncertainties within reservoir models. Furthermore, upscaling allows for the integration of fine-scale geological and petrophysical properties, resulting in more realistic reservoir simulations and a deeper understanding of fluid flow dynamics. This, in turn, facilitates better decision-making concerning reservoir development and strategies for injection brine salinity during enhanced oil recovery.[212,213]

6.2 Materials and Methods

This work is divided into two phases. The first phase involved data collection from Chapter 2, and the development of a pressure drop versus injection brine salinity model. The second phase comprised the generation of pressure drop profiles against drainage radius for permeability before and after the soaking period to upscale core data to reservoir data.

6.2.1 Data Collection

The data collection involved gathering detailed information on core and fluid properties, as well as injection rates, for a series of coreflood experiments conducted using 0.2M, 0.15M, and 0.1M NaCl brine solutions. The primary goal of this data collection process was to determine the permeability values before and after a designated soaking period, allowing for comparative analysis. Additionally, the aim was to develop a salinity model that could accurately predict pressure drop with varying levels of salinity of NaCl brine.

6.2.2 Pressure drop-Salinity Model Development

The model for pressure-drop versus brine salinity was developed using pressure-drop data from each coreflood experiment involving 0.2M, 0.15M, and 0.1M NaCl brine injections. By analyzing the collected data points, a best-fit model was derived, and the resulting equation was utilized for prediction purposes.

6.2.3 Core Data to Reservoir Upscaling

For upscaling, core and fluid properties, as well as hypothetical reservoir data, were used. Radial Darcy's law was employed to generate pressure drop profiles against drainage radius using permeability before and after the soaking period. The comparative analysis of these profiles indicated how the pressure drop spiked when the CSC was reached at 0.1M NaCl injection.

6.3 Results and Discussion

6.3.1 Data Collection

The core and fluid properties, along with injection rate data, were collected for a series of coreflood experiments conducted using 0.2M, 0.15M, and 0.1M NaCl brine solutions. Additionally, permeability values before and after soaking were calculated for the respective corefloods. These permeability measurements were crucial for upscaling the core data to the reservoir scale. Core-3 results demonstrate around 40% reduction in permeability at a CSC of 0.1M NaCl. The complete dataset is provided in Table 6.1.

Table 6.1 Core and fluid properties.

Parameters	*Core-1*	*Core-2*	*Core-3*
Injection brine salinity, M	0.2	0.15	0.1
Average Δp before soaking, psi	6.30	7.31	7.25
Average Δp after soaking, psi	6.61	7.62	12.11
Core diameter = core thickness, d, cm	3.81	3.81	3.81
Core length, L, cm	7.62	8	7.9
Area, A, cm2	11.40	11.40	11.40
μ-brine, cp	1.001	0.9802	0.9311
Injection rate, q, cc/sec	0.0033	0.0033	0.0033
Permeability, k before soaking, mD	5.02	4.57	4.36
Permeability, k after soaking, mD	4.97	4.39	2.61

6.3.2 Pressure-drop versus Salinity Model

The pressure drop versus brine salinity model was developed using pressure drop data from Table 6.1. These experiments involved injecting brine solutions with salinities of 0.2M, 0.15M, and 0.1M NaCl into the cores. The pressure-drop values measured during these injections were recorded and used as data points for the model development. By analyzing the collected data points, a best-fit model was formulated to accurately represent the relationship between pressure drop and brine salinity as shown in Figure 6.1. This model was developed using regression analysis and exponential equation to determine the most suitable equation that describes the observed patterns. Equation 6.1 presents the model for pressure drop as a function of salinity in Upper Berea Gray sandstone cores.

$$\Delta p = 1.5102 \times (NaCl\ salinity)^{-0.891} \tag{6.1}$$

Once the best-fit model was established, it was then utilized for predictive purposes. This means that the developed equation can be used to predict the pressure drop for NaCl brine injections in Upper Berea Gray sandstone with salinities outside the tested range. By inputting the salinity value into the equation, the model can provide a reasonably accurate prediction of the expected pressure drop under specific conditions.

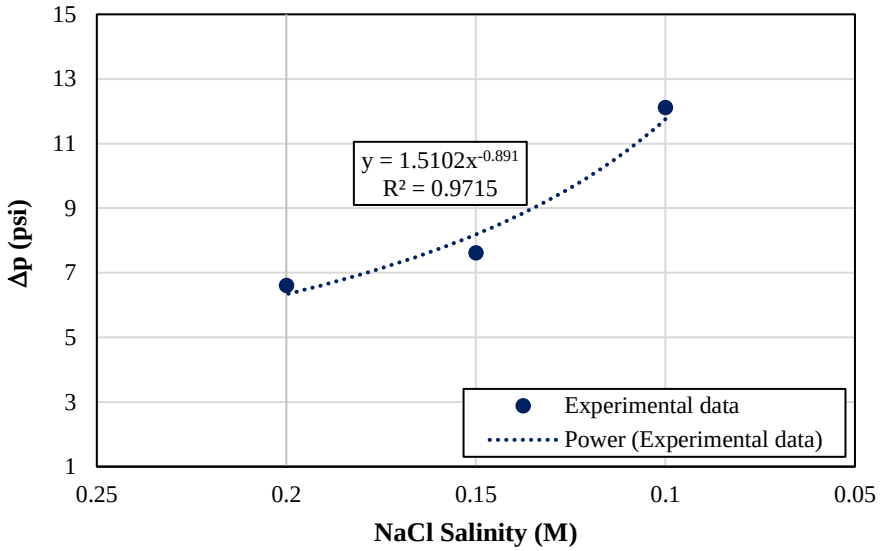

Figure 6.1 Pressure-drop versus NaCl brine salinity in Upper Berea Gray sandstone core.

Based on the developed model in Equation 6.1, the Darcy Equation has been modified to incorporate the effect of injection brine salinity on permeability for the Upper Berea Gray Sandstone reservoir. The modified Darcy equation is presented as Equation 6.2, with the permeability in this equation termed as k_{model}. Using Equation 3.2, the k_{model} for 0.2M, 0.15M, and 0.1M NaCl brine injection was estimated to be 5.17 mD, 4.08 mD, and 2.69 mD, respectively, after the soaking period. These results are in close agreement with the actual results obtained during coreflooding, as presented in Table 6.1. By considering the impact of injected brine salinity on permeability, reservoir and production engineers can make more informed decisions related to fines migration control, reservoir management, and fluid injection strategies for enhanced oil recovery.

$$k_{model} = \frac{14700q\mu L}{A(1.5102 \times (NaCl\ salinity)^{-0.891})} \tag{6.2}$$

Using Equation 3.2, the k_{model} for 0.2M, 0.15M, and 0.1M NaCl brine injection was estimated to be 5.17 mD, 4.08 mD, and 2.69 mD after the soaking period, respectively. These results are in close agreement with the actual results obtained during coreflooding as presented in Table 6.1.

6.3.3 Core Scale Skin Factor Calculation

Considering the concept of radial Darcy law as shown in Equation 6.2 and based on Δp_{ideal} (at 0.2M NaCl) and Δp_{actual} (at 0.1M NaCl) from Figure 6.1, the core-scale skin factor is calculated using the following steps.

$$\Delta p = \frac{141.2 q \mu B \left[\ln\left(\frac{r_e}{r_w}\right) + S\right]}{kh} \tag{6.3}$$

$$\Delta p_{actual} - \Delta p_{ideal} = \frac{141.2 q \mu B \left[\ln\left(\frac{r_e}{r_w}\right) + S\right]}{kh} - \frac{141.2 q \mu B \left[\ln\left(\frac{r_e}{r_w}\right)\right]}{kh}$$

$$\Delta p_{actual} - \Delta p_{ideal} = \frac{141.2 q \mu B \left[\ln\left(\frac{r_e}{r_w}\right)\right]}{kh} + \frac{141.2 q \mu B S}{kh} - \frac{141.2 q \mu B \left[\ln\left(\frac{r_e}{r_w}\right)\right]}{kh}$$

$$\Delta p_{actual} - \Delta p_{ideal} = \frac{141.2 q \mu B S}{kh}$$

$$S = \frac{kh(\Delta p_{actual} - \Delta p_{ideal})}{141.2 q \mu B} \tag{6.4}$$

Using Equation 6.4 and core properties from Table 6.1, the skin factor is calculated.

$$S = \frac{5.02 \times 0.125 (12.11 - 6.61)}{141.2 \times 0.00181 \times 1.001 \times 1} = 13.5$$

6.3.4 Core Data to Reservoir Upscaling

It is assumed that the skin factor is the same for both the core and reservoir scales. Figure 6.2 presents the schematic of the reservoir, illustrating the drainage radius, wellbore radius, initial reservoir pressure, wellbore flowing pressure, and formation thickness. For upscaling, core and fluid properties were utilized alongside hypothetical reservoir data as presented in Table 6.2. The radial Darcy law, a fundamental equation governing fluid flow through porous media, was employed to model the pressure drop phenomenon. Applying Equation 6.3, pressure drop profiles against drainage radius were generated using skin factor to examine the variation in Δp before and after fines migration.

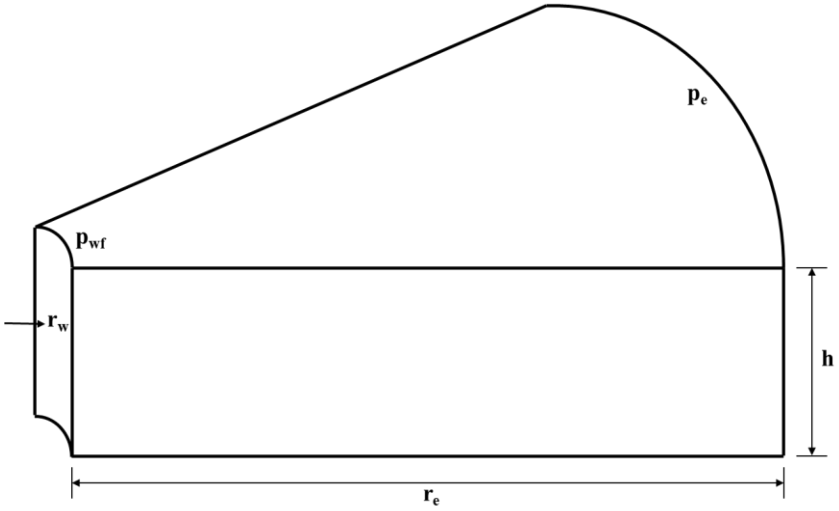

Figure 6.2. Schematic of a reservoir.

Table 6.2 Reservoir data.

Parameter	*Value*
Drainage radius, r_e, ft	3000
Wellbore radius, r_w, ft	0.5
Formation volume factor, B, RB/STB	1
Initial reservoir pressure, p_e, psi	3700
Wellbore flowing pressure, p_{wf}, psi	2500
Formation thickness, h, ft	30

$$\Delta p = \frac{141.2 q \mu B \left[\ln\left(\frac{r_e}{r_w}\right) + S\right]}{kh} \tag{6.3}$$

Figures 6.3 through 6.5 illustrate pressure drop profiles against drainage radius for 0.2M, 0.15M, and 0.1M NaCl brine injections, respectively. The comparative analysis of these profiles revealed a significant increase in pressure drop once the CSC was reached during the injection of 0.1M NaCl.

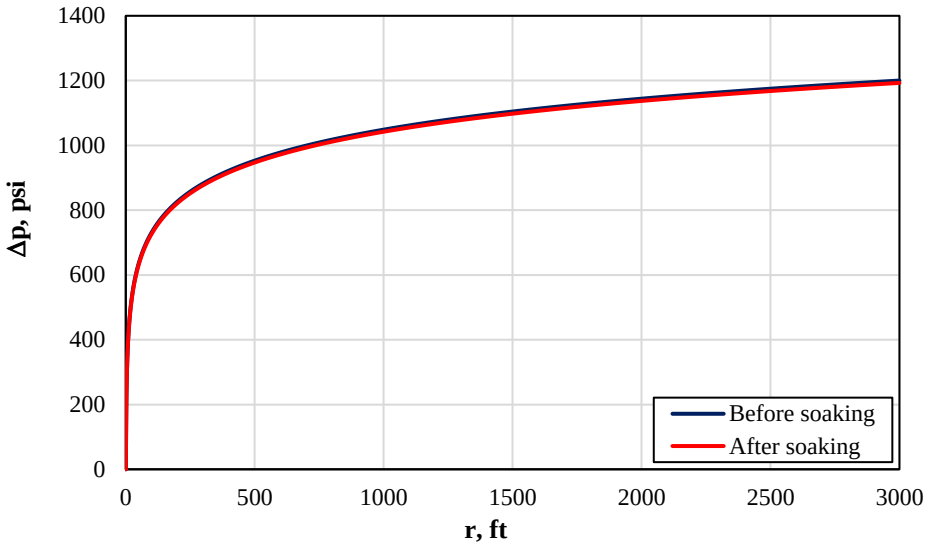

Figure 6.3 Δp as a function of drainage radius for 0.2M NaCl brine injection.

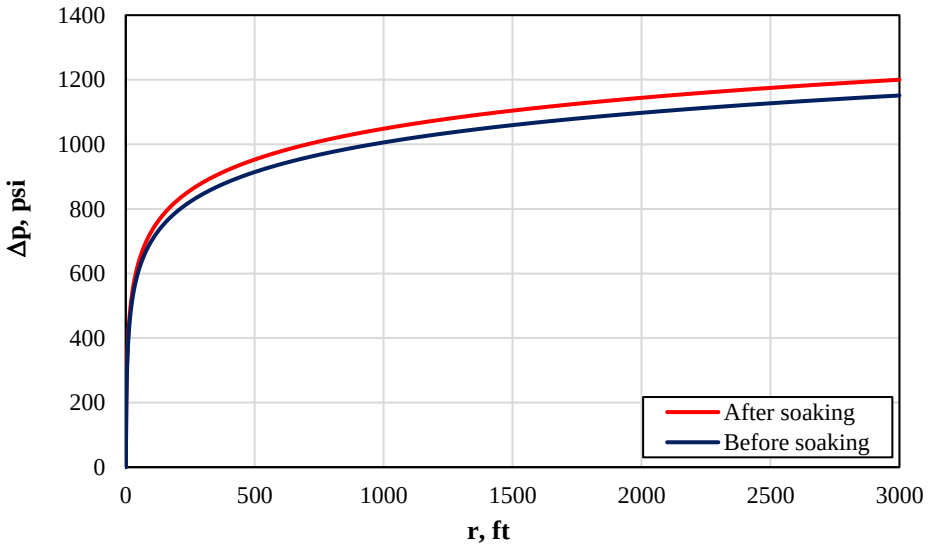

Figure 6.4 Δp as a function of drainage radius for 0.15M NaCl brine injection.

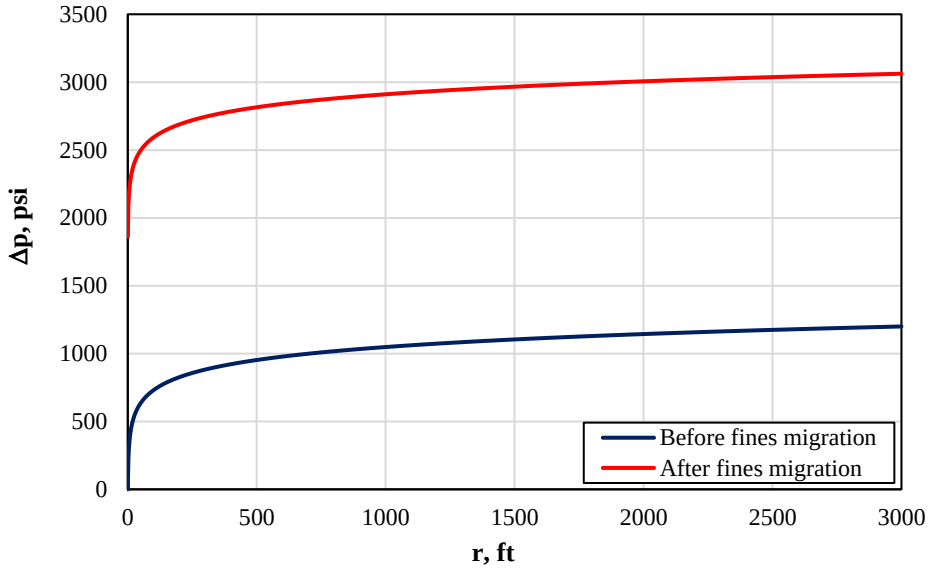

Figure 6.5 Δp as a function of drainage radius for 0.1M (CSC) NaCl brine injection.

The generated pressure-drop profiles provided valuable insights into the behavior of the reservoir based on upscaling. Figures 6.3 and 6.4 suggest that brine injection with 0.2M and 0.15M NaCl did not trigger any fines migration within the reservoir before and after the soaking period. The soaking period allowed the injected fluid to interact with the sand grains and fine particles, altering the surface forces and consequently affecting the permeability due to fines migration. Upon analyzing the pressure drop profile in Figure 6.4, it was observed that before the soaking period, the pressure drop was comparable to Figures 6.2 and 6.3, indicating a consistent permeability distribution within the reservoir. However, after the soaking period for 0.1M NaCl injection, the pressure drop exhibited a noticeable spike once the CSC was achieved at this salinity. The sudden increase in pressure drop at the CSC suggested a significant fines detachment, migration, and straining, which altered the flow behavior of the fluid within the reservoir. This increase in pressure drop could be attributed to the alteration of the pore structure and pore throat plugging, resulting in a reduction in permeability. Understanding such changes in pressure drop profiles is crucial for assessing the effect of the injected fluid's salinity on reservoir permeability due to fines migration and predicting its impact on reservoir performance.

6.4 Summary

In conclusion, this chapter has focused on the upscaling of coreflooding results to

reservoir scale to better understand the permeability impairment caused by fines migration after reaching the CSC. The data from coreflood tests demonstrated a significant 40% decline in permeability due to fines migration and straining.

- To gain further insights, an exponential model was developed based on the pressure drop (Δp) observed during coreflooding and the injection brine salinity (0.2M, 0.15M, and 0.1M NaCl). The model demonstrated satisfactory performance, accurately predicting the Δp within an acceptable error range of ±10%. Utilizing data on core permeability before and after the soaking period, the model permeability (k_{model}) was calculated using the developed exponential model.
- To extend these findings to the reservoir scale, pressure profiles as a function of drainage radius were generated using the radial Darcy law for NaCl salinities of 0.2M, 0.15M, and 0.1M. The upscaling process considered permeability changes before and after the soaking period, effectively translating core data into reservoir data using skin factor.
- Overall, the comprehensive approach employed in this chapter has provided valuable insights into the complex phenomenon of fines migration and its impact on permeability impairment in the context of reservoir engineering. The integration of DLVO modeling, coreflooding experiments, and the developed salinity model has contributed to a deeper understanding of reservoir behavior under varying salt concentrations. These findings have practical applications for enhanced oil recovery strategies and optimizing reservoir performance.

CHAPTER 7: Applications and Limitations

The following sections present the various applications of the DLVO modeling approach in predicting critical parameters. Specifically, the significance of this approach in predicting fines migration, which plays a pivotal role in mitigating formation damage in sandstone reservoirs, has been highlighted. Additionally, the limitations inherent in the current work are carefully outlined, shedding light on specific areas that warrant further investigation. This exploration of both the applications and constraints of the DLVO modeling approach serves as a crucial steppingstone, laying the groundwork for future research endeavors in this field.

7.1 Applications of Current Research

For the proof of concept, the DLVO modeling approach was employed to model the SFB system considering a single-phase system, and critical parameters such as critical salt concentration, critical pH, and critical flow rate were predicted and validated experimentally. The following section highlights the most significant applications of the proposed approach on a field scale.

- Current research has a direct application in water aquifer recharging into sandstone reservoirs where a change in salinity or pH of injecting liquid compared to formation water salinity and pH may trigger fines migration. Fines migration during aquifer recharging pertains to the movement of clay fine particles when water is introduced into an aquifer. This phenomenon can result in clogs, reduced water flow, and potential damage to the formation. Considering a single-phase system of water aquifer, the DLVO model can effectively be employed to predict CSC, critical pH, and critical flow rate to predict these critical parameters and avoid formation damage.
- The proposed approach can also be applied to water disposal in sandstone reservoirs. The fines migration issue encountered during the disposal of water into sandstone reservoirs poses a notable problem within the domains of petroleum engineering and hydrogeology. To prevent fines migration and ensure the sustained effectiveness of water disposal into sandstone reservoirs, the DLVO modeling

approach can be applied for the prediction of threshold values of salinity, pH, and injection rate.

- Similarly, the proposed approach has a direct application in water-bearing subsurface formations where fines migration can hinder groundwater flows and impair formation permeability.
- The proposed DLVO model can effectively incorporate the effects of monovalent and divalent ions to predict the mentioned critical parameters. Therefore, the proposed can be directly applied to optimize Smart Water injection in sandstone reservoirs.
- DLVO theory can be applied to study the stability and behavior of nanoparticles in nanofluids. Nanoparticles are used in various EOR techniques, and understanding their stability and interactions with reservoir fluids is essential for their effective application.

7.2 Recommendations

The DLVO model proved to be a useful tool for predicting critical parameters considering injection brine salinity, pH, and flow rate, however, it has some limitations, which are given below:

- The DLVO assumes fine particles of spherical shape, but in reality, fine particles of different shapes are present within the sandstone which might reduce the accuracy of the model.
- The model cannot incorporate any mineral dissolution within the sandstone.
- DLVO theory does not account for the surface roughness of particles, which can significantly influence particle interactions.
- The model can forecast the beginning of fines migration in the porous medium, but it is unable to estimate the number of fines that will detach and migrate.
- It does not show anything regarding the reattachment of detached fines.
- The biggest limitation is the inability to know how many fines are candidates for mobilization.
- The model cannot predict sudden changes in surface charges and the accompanying surface forces.

- In reality, almost all the variables such as surface charge and particle size consist of distributions, however, the DLVO model does not have the ability to incorporate the distributions of these parameters, rather it uses the average values of these input parameters.

CHAPTER 8: Conclusion and Recommendations

In this thesis, the DLVO modeling approach has been utilized as a prediction tool to estimate critical parameters such as CSC, critical pH, and critical flow rate in sandstone core samples. This approach is based on the analysis of surface forces between sand grains and fine particles in an SFB system. To evaluate the applicability of the DLVO modeling approach and to demonstrate proof of concept, all modeling and experimentation were conducted in the context of single-phase flow and at ambient temperature. Notably, the DLVO model predictions were found to be in close agreement with the experimental results, falling within an acceptable range of error. By measuring the required parameters under field conditions, the presented approach in this research can be applied to design waterflooding and alkaline flooding operations for enhanced oil recovery and improved reservoir management, without the need for extensive experimentation.

8.1 Conclusions

The following points highlight the most significant findings of this research:

- The quantification of attraction and repulsion forces in the SFB system using significant parameters such as zeta potential, brine salinity, pH, and fine particle size allowed for the development of DLVO models. These models accurately predicted the critical salt concentration (CSC) for monovalent brines such as NaCl and KCl based on the analysis of the total interaction energy of the given system.
- The DLVO model incorporated the effect of divalent brines such as $CaCl_2$ and $MgCl_2$ and predicted lower CSCs than monovalent brines.
- A critical pH was predicted using the DLVO model with fixed salinity varying pH brines.
- The DLVO model integrated the effect of silica nanoparticles (SNPs) to reduce repulsion force by changing the sand surface potential and suppressing the electric double layer. The application of 0.1wt% SNPs reduced the CSC by 32% and improved the critical pH by 37%.
- A new model was developed by integrating DLVO and hydrodynamic forces to model high-rate injection scenarios under varying salinity conditions. The model

predicted the critical flow rates under the influence of electrostatic and hydrodynamic forces.

- The DLVO model predictions were validated experimentally using single-phase corefloods and acceptable results were obtained. This indicates the reliability of the DLVO model in predicting the behavior of fine particles in SFB systems.

8.2 Recommendations

Despite the DLVO modeling approach's remarkable predictive ability and its close agreement with experimental results, it is important to acknowledge that there are certain limitations inherent in this approach that have not been fully addressed in this work. Therefore, it is crucial to outline the prospects for future research to overcome these limitations and advance the field. The following points define the key areas that should be addressed in future work:

- The current research is primarily concentrated on investigating single-phase systems to establish proof of concept and assess the prediction capabilities of the DLVO model. While this approach has provided valuable insights, it is crucial to recognize that real field scenarios always involve the presence of multiple phases. Consequently, future research should aim to incorporate the influence of these additional phases to achieve more accurate predictions.
- Measuring the zeta potential of sand grains in the presence of oil using a Zetasizer can pose significant challenges, primarily due to the tendency of oil to detach the sand surface within the sample cup. This detachment can lead to misleading results and hinder accurate zeta potential measurements. Therefore, it is imperative to explore new approaches that can overcome these challenges and enable reliable zeta potential measurements for sand samples with oil. These approaches include but are not limited to streaming potential, electroacoustic spectroscopy, and electrokinetic sonic amplitude.
- In the context of the DLVO model, it is crucial to consider temperature-dependent zeta potential measurements. The DLVO theory relies on accurate zeta potential values to estimate the interaction forces between colloidal particles. Since temperature can significantly affect the zeta potential of materials, it becomes

essential to account for the actual reservoir temperature when measuring the zeta potential of sandstone reservoirs.

- In this thesis, the zeta potentials of the samples were measured under ambient conditions using a Zetasizer. To ensure the reliability of the modeling process, it becomes necessary to consider the actual temperature and pressure conditions encountered in the reservoir. Although Zetasizer has advanced over time and can now accommodate higher temperatures, allowing measurements up to 120 °C, the challenge lies in measuring zeta potentials at high pressures. Currently, there is a dearth of known apparatuses available to measure zeta potentials under high-pressure conditions. This limitation poses a significant hurdle in accurately representing real-field situations, particularly in reservoir environments where pressures are substantial. To overcome this limitation, further research is required to develop suitable apparatuses and methodologies that enable zeta potential measurements at elevated pressures.
- The integration of the DLVO modeling approach with reservoir simulators holds immense potential in the design and optimization of various fluid flow scenarios in sandstone reservoirs and subsurface sandstone aquifers. By combining the predictive power of the DLVO model with the comprehensive capabilities of reservoir simulators, engineers and researchers can gain valuable insights into the fluid–particle interactions within these complex systems. Furthermore, the integration of DLVO modeling with reservoir simulators has applications beyond oil recovery. It can also be instrumental in understanding and managing water flows in subsurface sandstone aquifers. Sandstone aquifers are important sources of groundwater, and accurately predicting the movement and transport of water through these porous formations is crucial for sustainable water resource management.

Nomenclature

A = core cross-sectional area, cm^2

A_H = Hamaker constant, = 1.52×10^{-20} J

B = formation volume factor, RB/STB

e = electron charge, = 1.60×10^{-19} C

d = core diameter, cm

F_d = drag force, kg-m/s^2

F_e = effective electrostatic force, kg-m/s^2

F_g = gravitational force, kg-m/s^2

$F\ (k_a)$ = Henry's function

F_l = lift force, kg-m/s^2

h = formation thickness, ft

h = separation distance, nm

h_o = minimum equilibrium distance, m

H = dimensionless distance = h/r_f

I_l = lift lever arm, m

I_d = drag lever arm, m

I_s = ionic strength of permeating fluid, M

k = formation permeability, mD

k = inverse Debye length, m^{-1}

k_B = Boltzmann constant, = 1.38×10^{-23} JK^{-1}

k_s = damage permeability, mD

L = core length, cm

M = molarity, mol/liter

M_d = viscous surface stress, kg-m^2/s^2

N_A = Avogadro's number = 6.02214×10^{23} $mole^{-1}$

pH = pH of injection fluid = 6.5 – 7.5

p_e = external boundary pressure, psi

p_{wf} = wellbore flowing pressure, psi

q = flow rate, cc/sec

r_e = drainage radius, ft

r_f = fine particle radius, m

r_p = pore radius = 0.00005 m

r_w = wellbore radius, ft

S = skin factor

T = absolute temperature, = 297.15 K

U_E = electrophoretic mobility, V

v = injection velocity, m/s

V_{AB} = acid-base interaction energy, J

V_{AB}^{o} = hydrophobic/hydrophilic interaction, J

V_{BR} = Born repulsion energy, J

V_{EDL} = Electrical double-layer energy, J

V_{LVW} = London-van der Waals energy, J

V_T = total interaction energy, J

z = valence of the ion

ζ = zeta potential, mV

μ = fluid viscosity, kg/m-s

σ = atomic collision diameter, = 5×10^{-10} m

ε_m = dielectric constant of water = 80

ε_o = permittivity of the vacuum, = 8.85×10^{-12} $F.m^{-1}$

η = viscosity of the solution, $kg.m^{-1}s^{-1}$

λ = decay length of liquid molecules, m

π = pi = 3.1416

Δp = pressure drop, psi

References

(1) Chrysikopoulos, C. V; Masciopinto, C.; La Mantia, R.; Manariotis, I. D. Removal of Biocolloids Suspended in Reclaimed Wastewater by Injection into a Fractured Aquifer Model. *Environ. Sci. Technol.* **2010**, *44* (3), 971–977.

(2) Borazjani, S.; Chequer, L.; Russell, T.; Bedrikovetsky, P. Injectivity Decline during Waterflooding and PWRI Due to Fines Migration. In *SPE International Conference and Exhibition on Formation Damage Control*; OnePetro, 2018.

(3) You, Z.; Bedrikovetsky, P. Well Productivity Impairment Due to Fines Migration. In *SPE International Conference and Exhibition on Formation Damage Control*; OnePetro, 2018.

(4) Bjorlykke, K. *Petroleum Geoscience: From Sedimentary Environments to Rock Physics*; Springer Science & Business Media, 2010.

(5) Chavan, M.; Dandekar, A.; Patil, S.; Khataniar, S. Low-Salinity-Based Enhanced Oil Recovery Literature Review and Associated Screening Criteria. *Pet. Sci.* **2019**, *16* (6), 1344–1360.

(6) Austad, T.; RezaeiDoust, A.; Puntervold, T. Chemical Mechanism of Low Salinity Water Flooding in Sandstone Reservoirs. *Proc. - SPE Symp. Improv. Oil Recover.* **2010**, *1*, 679–695. https://doi.org/10.2118/129767-MS.

(7) Kaplan, D. A.; Muñoz-Carpena, R. Groundwater Salinity in a Floodplain Forest Impacted by Saltwater Intrusion. *J. Contam. Hydrol.* **2014**, *169*, 19–36.

(8) Mungan, N. Permeability Reduction through Changes in PH and Salinity. *J. Pet. Technol.* **1965**, *17* (12), 1449–1453.

(9) Gomaa, I.; Mahmoud, M.; Kamal, M. S. Novel Approach for Sandstone Acidizing Using in Situ-Generated Hydrofluoric Acid with the Aid of Thermochemicals. *ACS omega* **2020**, *5* (2), 1188–1197.

(10) Li, Z.; Du, C.; Tang, Y.; Li, X. Experimental and Statistical Investigation of Reservoir Properties with the Effect of Waterflooding Treatment. *ACS omega* **2020**, *5* (33), 20922–20931.

(11) McDowell-Boyer, L. M.; Hunt, J. R.; Sitar, N. Particle Transport through Porous Media. *Water Resour. Res* **1986**, *22* (13), 1901–1921.

(12) Sarkar, A. K.; Sharma, M. M. Fines Migration in Two-Phase Flow. *J. Pet. Technol.* **1990**, *42* (05), 646–652.

(13) Torkzaban, S.; Bradford, S. A.; Vanderzalm, J. L.; Patterson, B. M.; Harris, B.; Prommer, H. Colloid Release and Clogging in Porous Media: Effects of Solution Ionic Strength and Flow Velocity. *J. Contam. Hydrol* **2015**, *181*, 161–171.

(14) Chrysikopoulos, C. V; Katzourakis, V. E. Colloid Particle Size-Dependent Dispersivity. *Water Resour. Res* **2015**, *51* (6), 4668–4683.

(15) Sotirelis, N. P.; Chrysikopoulos, C. V. Heteroaggregation of Graphene Oxide Nanoparticles and Kaolinite Colloids. *Sci. Total Env.* **2017**, *579*, 736–744.

(16) Muecke, T. W. Formation Fines and Factors Controlling Their Movement in Porous Media. *J. Pet. Technol.* **1979**, *31* (02), 144–150.

(17) Khilar, K. C.; Fogler, H. S. *Migrations of Fines in Porous Media*; Springer Science & Business Media: New York, 1998; Vol. 12.

(18) Civan, F. *Reservoir Formation Damage-Fundamentals, Modeling, Assessment and Mitigation Gulf Pub*, 3rd ed.; Gulf Professional Publishing: Houston, TX, 2016.

(19) Morrow, N. R.; Tang, G. -q.; Valat, M.; Xie, X. Prospects of Improved Oil Recovery Related to Wettability and Brine Composition. *J. Pet. Sci. Eng.* **1998**, *20* (3–4), 267–276.

(20) Ashraf, A.; Hadia, N.; Torsaeter, O.; Tweheyo, M. T. *Laboratory Investigation of Low Salinity Waterflooding as Secondary Recovery Process: Effect of Wettability*; In SPE Oil and Gas India Conference and Exhibition: Mumbai, India, 2010.

(21) Hassenkam, T.; Mitchell, A. C.; Pedersen, C. S.; Skovbjerg, L.; Bovet, N.; Stipp, S. L. S. The Low Salinity Effect Observed on Sandstone Model Surfaces. *Colloids Surfaces A Physicochem. Eng. Asp.* **2012**, *403*, 79–86.

(22) Collini, H.; Li, S.; Jackson, M. D.; Agenet, N.; Rashid, B.; Couves, J. Zeta Potential in Intact Carbonates at Reservoir Conditions and Its Impact on Oil Recovery during Controlled Salinity Waterflooding. *Fuel* **2020**, *266* (11692), 16. https://doi.org/https://doi.org/10.1016/j.fuel.2019.116927.

(23) Takeya, M.; Shimokawara, M.; Elakneswaran, Y.; Nawa, T.; Takahashi, S. Predicting the Electrokinetic Properties of the Crude Oil/Brine Interface for Enhanced Oil Recovery in Low Salinity Water Flooding. *Fuel* **2019**, *235*, 822–831.

(24) Mahani, H.; Menezes, R.; Berg, S.; Fadili, A.; Nasralla, R.; Voskov, D.; Joekar-Niasar, V. Insights into the Impact of Temperature on the Wettability Alteration by Low Salinity in Carbonate Rocks. *Energy & Fuels* **2017**, *31* (8), 7839–7853.

(25) Kumar, M.; Fogden, A.; Morrow, N. R.; Buckley, J. S. Mechanisms of Improved Oil Recovery from Sandstone by Low Salinity Flooding. *Petrophysics* **2011**, *52* (06), 428–436.

(26) Takeya, M.; Ubaidah, A.; Shimokawara, M.; Okano, H.; Nawa, T.; Elakneswaran, Y. Crude Oil/Brine/Rock Interface in Low Salinity Waterflooding: Experiments, Triple-Layer Surface Complexation Model, and DLVO Theory. *J. Pet. Sci. Eng.* **2020**, *188* (10691), 13.

(27) Nasralla, R. A.; Alotaibi, M. B.; Nasr-El-Din, H. A. *Efficiency of Oil Recovery by Low Salinity Water Flooding in Sandstone Reservoirs*; In SPE Western North American Region Meeting: Anchorage, Alaska, USA, 2011.

(28) Xie, Q.; Liu, Y.; Wu, J.; Liu, Q. Ions Tuning Water Flooding Experiments and Interpretation by Thermodynamics of Wettability. *J. Pet. Sci. Eng.* **2014**, *124*, 350–358.

(29) Tang, G. Q.; Morrow, N. R. Salinity, Temperature, Oil Composition, and Oil Recovery by Waterflooding. *SPE Reserv. Eng.* **1997**, *12* (04), 269–276.

(30) Tang, G.-Q.; Morrow, N. R. Influence of Brine Composition and Fines Migration on Crude Oil/Brine/Rock Interactions and Oil Recovery. *J. Pet. Sci. Eng.* **1999**, *24* (2–4), 99–111.

(31) Morrow, N.; Buckley, J. Improved Oil Recovery by Low-Salinity Waterflooding. *J. Pet. Technol.* **2011**, *63* (05), 106–112.

(32) Lager, A.; Webb, K. J.; Black, C. J. J.; Singleton, M.; Sorbie, K. S. Low Salinity Oil Recovery-an Experimental Investigation1. *Petrophysics-The SPWLA J. Form. Eval. Reserv. Descr.* **2008**, *49* (01).

(33) Al-Sarihi, A.; Russell, T.; Bedrikovetsky, P.; Zeinijahromi, A. Fines Stabilization by Ca Ions and Its Effect on LSW Injection. *Energy Fuels* **2019**, *33* (11), 10775–10786.

(34) Yu, M.; Hussain, F.; Arns, J.-Y.; Bedrikovetsky, P.; Genolet, L.; Behr, A.; Kowollik, P.; Arns, C. H. Imaging Analysis of Fines Migration during Water Flow with

Salinity Alteration. *Adv. Water Resour.* **2018**, *121*, 150–161.

(35) Yu, M. An Experimental Investigation of Permeability Damage and Mobility Control During Fines-Assisted Waterflooding. *Ph. D. Thesis, Univ. New South Wales, Sydney NSW* **2018**, *2052*.

(36) Tangparitkul, S.; Saul, A.; Leelasukseree, C.; Yusuf, M.; Kalantariasl, A. Fines Migration and Permeability Decline during Reservoir Depletion Coupled with Clay Swelling Due to Low-Salinity Water Injection: An Analytical Study. *J. Pet. Sci. Eng.* **2020**, *194* (107448), 13.

(37) Prempeh, K. O. K.; Chequer, L.; Badalyan, A.; Bedrikovetsky, P. Effects of the Capillary-Entrapped Phase on Fines Migration in Porous Media. *J. Nat. Gas Sci. Eng.* **2020**, *73* (10304), 16.

(38) Bedrikovetsky, P.; Zeinijahromi, A.; Badalyan, A.; Ahmetgareev, V.; Khisamov, R. *Fines-Migration-Assisted Low-Salinity Waterflooding: Field Case Analysis (Russian)*; In SPE Russian petroleum technology conference: Moscow, Russia, 2015.

(39) Hussain, F.; Zeinijahromi, A.; Bedrikovetsky, P.; Badalyan, A.; Carageorgos, T.; Cinar, Y. An Experimental Study of Improved Oil Recovery through Fines-Assisted Waterflooding. *J. Pet. Sci. Eng.* **2013**, *109*, 187–197.

(40) Al-Sarihi, A.; Zeinijahromi, A.; Genolet, L.; Behr, A.; Kowollik, P.; Bedrikovetsky, P. Effects of Fines Migration on Residual Oil during Low-Salinity Waterflooding. *Energy & Fuels* **2018**, *32* (8), 8296–8309.

(41) Ahmetgareev, V.; Zeinijahromi, A.; Badalyan, A.; Khisamov, R.; Bedrikovetsky, P. Analysis of Low Salinity Waterflooding in Bastrykskoye Field. *Pet. Sci. Technol.* **2015**, *33* (5), 561–570.

(42) Izuwa, N.; Onwukwe, S.; Akinbamini, O. Evaluation of Fines Assisted Low Salinity Water Flooding in Edge Water Drive Reservoirs. *J. Pet. Environ. Biotechnol.* **2018**, *9* (1000381), 7.

(43) Yua, M.; Hussaina, F.; Bedrikovetskyb, P. *Low-Salinity Waterflood with Non-Polar Oil: The Effects of Fines Migration Excluding the Wettability Alteration Effects*; In International Symposium of the Society of Core Analysts: Vienna, Austria, 2017.

(44) Hussain, F.; Zeinijahromi, A.; Bedrikovetski, P.; Badalyan, A.; Carageorgos, T.;

Cinar, Y. *Enhanced Oil Recovery through Low Salinity Fines-Assisted Waterflooding: Laboratory and Mathematical Modelling*; In SPE Asia Pacific Oil & Gas Conference and Exhibition: Adelaide, Australia, 2014.

(45) Barkman, J.; Abrams, A.; Darley, H.; Hill, H. An Oil-Coating Process to Stabilize Clays in Fresh Waterflooding Operations (Includes Associated Paper 6405). *J. Pet. Technol.* **1975**, *27* (09), 1053–1059.

(46) Asghari, K.; Kharrat, R.; Vossoughi, S. Alteration of Permeability by Fine Particle Movement - A Water Injectivity Problem; In SPE International Symposium on Oilfield Chemistry, Society of Petroleum Engineers: San Antonio, Texas, 1995.

(47) Russell, T.; Pham, D.; Neishaboor, M. T.; Badalyan, A.; Behr, A.; Genolet, L.; Kowollik, P.; Zeinijahromi, A.; Bedrikovetsky, P. Effects of Kaolinite in Rocks on Fines Migration. *J. Nat. Gas Sci. Eng.* **2017**, *45*, 243–255.

(48) Mansouri, M.; Nakhaee, A.; Pourafshary, P. Effect of SiO2 Nanoparticles on Fines Stabilization during Low Salinity Water Flooding in Sandstones. *J. Pet. Sci. Eng.* **2019**, *174*, 637–648.

(49) Bennion, D. B. An Overview of Formation Damage Mechanisms Causing a Reduction in the Productivity and Injectivity of Oil and Gas Producing Formations. *J. Can. Pet. Technol.* **2002**, *41* (11), 29–36. https://doi.org/10.2118/02-11-DAS.

(50) Sharma, M. M.; Yortsos, Y. C. Transport of Particulate Suspensions in Porous Media: Model Formulation. *AIChE J* **1987**, *33* (10), 1636–1643. https://doi.org/10.1002/aic.690331007.

(51) Martin, J. C. The Effects of Clay on the Displacement of Heavy Oil by Water. In *Venezuelan annual meeting*; OnePetro, 1959.

(52) Khilar, K. C.; Fogler, H. S. The Existence of a Critical Salt Concentration for Particle Release. *J. Colloid Interface Sci.* **1984**, *101* (1), 214–224.

(53) Guo, Z.; Hussain, F.; Cinar, Y. Physical and Analytical Modelling of Permeability Damage in Bituminous Coal Caused by Fines Migration during Water Production. *J. Nat. Gas Sci. Eng.* **2016**, *35*, 331–346.

(54) Fogden, A.; Kumar, M.; Morrow, N. R.; Buckley, J. S. Mobilization of Fine Particles during Flooding of Sandstones and Possible Relations to Enhanced Oil Recovery. *Energy & Fuels* **2011**, *25* (4), 1605–1616.

(55) Galal, S. K.; Elgibaly, A. A.; Elsayed, S. K. Formation Damage Due to Fines Migration and Its Remedial Methods. *Egypt. J. Pet* **2016**, *25* (4), 515–524.

(56) Al-Yaseri, A.; Zhang, Y.; Ghasemiziarani, M.; Sarmadivaleh, M.; Lebedev, M.; Roshan, H.; Iglauer, S. Permeability Evolution in Sandstone Due to CO2 Injection. *Energy & Fuels* **2017**, *31* (11), 12390–12398.

(57) Othman, F.; Yu, M.; Kamali, F.; Hussain, F. Fines Migration during Supercritical CO2 Injection in Sandstone. *J. Nat. Gas Sci. Eng.* **2018**, *56*, 344–357.

(58) Wang, Q.; Yang, S.; Han, H.; Wang, L.; Qian, K.; Pang, J. Experimental Investigation on the Effects of CO2 Displacement Methods on Petrophysical Property Changes of Ultra-Low Permeability Sandstone Reservoirs near Injection Wells. *Energies* **2019**, *12* (2), 327.

(59) Sokama-Neuyam, Y. A.; Ginting, P. U. R.; Timilsina, B.; Ursin, J. R. The Impact of Fines Mobilization on CO2 Injectivity: An Experimental Study. *Int. J. Greenh. Gas Control* **2017**, *65*, 195–202.

(60) Xie, Q.; Saeedi, A.; Piane, D.; Esteban, C. .; Brady, L. .; V., P. Fines Migration during CO2 Injection: Experimental Results Interpreted Using Surface Forces. *Int. J. Greenh. Gas Control* **2017**, *65*, 32–39.

(61) Sokama-Neuyam, Y. A.; Forsetløkken, S. L.; Lien, J. -e.; Ursin, J. R. The Coupled Effect of Fines Mobilization and Salt Precipitation on CO2 Injectivity. *Energies* **2017**, *10* (8), 1125.

(62) Pate, K.; Safier, P. *Advances in Chemical Mechanical Planarization (CMP)*; Babu, S., Ed.; 86; Woodhead Publishing: Cambridge, UK, 2016.

(63) Chequer, L.; Bedrikovetsky, P.; Carageorgos, T.; Badalyan, A.; Gitis, V. Mobilization of Attached Clustered Colloids in Porous Media. *Water Resour. Res* **2019**, *55* (7), 5696–5714.

(64) Xie, Q.; Saeedi, A.; Pooryousefy, E.; Liu, Y. Extended DLVO-Based Estimates of Surface Force in Low Salinity Water Flooding. *J. Mol. Liq.* **2016**, *221*, 658–665.

(65) Shehata, A. M.; Nasr-El-Din, H. A. Zeta Potential Measurements: Impact of Salinity on Sandstone Minerals. In *SPE International Symposium on Oilfield Chemistry*; SPE: The Woodlands, Texas, USA, 2015.

(66) Gulgonul, I. Zeta Potential of Teflon in Presence of Monovalent and Divalent Ions.

Physicochem. Probl. Miner. Process. **2019**, *55* (3), 792–801.

(67) Assef, Y.; Arab, D.; Pourafshary, P. Application of Nanofluid to Control Fines Migration to Improve the Performance of Low Salinity Water Flooding and Alkaline Flooding. *J. Pet. Sci. Eng.* **2014**, *124*, 331–340.

(68) Civan, F. *Reservoir Formation Damage*; Gulf Professional Publishing, 2015.

(69) Ochi, J.; Vernoux, J.-F. Permeability Decrease in Sandstone Reservoirs by Fluid Injection: Hydrodynamic and Chemical Effects. *J. Hydrol.* **1998**, *208* (3–4), 237–248.

(70) Bedrikovetsky, P.; Siqueira, F. D.; Furtado, C. A.; Souza, A. L. S. Modified Particle Detachment Model for Colloidal Transport in Porous Media. *Transp. porous media* **2011**, *86* (2), 353–383.

(71) Sharma, M. M.; Chamoun, H.; Sarma, D. S. H. S. R.; Schechter, R. S. Factors Controlling the Hydrodynamic Detachment of Particles from Surfaces. *J. Colloid Interface Sci.* **1992**, *149* (1), 121–134.

(72) Ryan, J. N.; Gschwend, P. M. Effects of Ionic Strength and Flow Rate on Colloid Release: Relating Kinetics to Intersurface Potential Energy. *J. Colloid Interface Sci.* **1994**, *164* (1), 21–34.

(73) Li, T.; Jin, Y.; Huang, Y.; Li, B.; Shen, C. Observed Dependence of Colloid Detachment on the Concentration of Initially Attached Colloids and Collector Surface Heterogeneity in Porous Media. *Environ. Sci. Technol.* **2017**, *51* (5), 2811–2820.

(74) Torkzaban, S.; Kim, H. N.; Simunek, J.; Bradford, S. A. Hysteresis of Colloid Retention and Release in Saturated Porous Media during Transients in Solution Chemistry. *Environ. Sci. Technol.* **2010**, *44* (5), 1662–1669.

(75) Arab, D.; Pourafshary, P. Nanoparticles-Assisted Surface Charge Modification of the Porous Medium to Treat Colloidal Particles Migration Induced by Low Salinity Water Flooding. *Colloids Surfaces A Physicochem. Eng. Asp.* **2013**, *436*, 803–814.

(76) Arab, D.; Pourafshary, P.; Ayatollahi, S.; Habibi, A. Remediation of Colloid-Facilitated Contaminant Transport in Saturated Porous Media Treated by Nanoparticles. *Int. J. Environ. Sci. Technol.* **2014**, *11* (1), 207–216.

(77) Ahmadi, M.; Habibi, A.; Pourafshary, P.; Ayatollahi, S. An Experimental Study of

Interaction between Nanoparticles'deposition on a Sintered Porous Medium and Migratory Fines. *J. Porous Media* **2013**, *16* (5), 459–467.

(78) Habibi, A.; Ahmadi, M.; Pourafshary, P.; Al-Wahaibi, Y. Reduction of Fines Migration by Nanofluids Injection: An Experimental Study. *SPE J.* **2012**, *18* (02), 309–318.

(79) Hasannejad, R.; Pourafshary, P.; Vatani, A.; Sameni, A. Application of Silica Nanofluid to Control Initiation of Fines Migration. *Pet. Explor. Dev.* **2017**, *44* (5), 850–859. https://doi.org/10.1016/S1876-3804(17)30096-4.

(80) Khilar, K. C.; Vaidya, R. N.; Fogler, H. S. Colloidally-Induced Fines Release in Porous Media. *J. Pet. Sci. Eng.* **1990**, *4* (3), 213–221.

(81) Gregory, J. Approximate Expressions for Retarded van Der Waals Interaction. *J. Colloid Interface Sci.* **1981**, *83* (1), 138–145.

(82) Israelachvili, J. N. Van Der Waals Forces between Particles and Surfaces. *Intermol. Surf. forces* **2011**, *3*, 253–289.

(83) Mahmood, T.; Amirtharajah, A.; Sturm, T. W.; Dennett, K. E. A Micromechanics Approach for Attachment and Detachment of Asymmetric Colloidal Particles. *Colloids Surfaces A Physicochem. Eng. Asp.* **2001**, *177* (2–3), 99–110.

(84) Musharova, D.; Mohamed, I. M.; Nasr-El-Din, H. A. *Detrimental Effect of Temperature on Fines Migration in Sandstone Formations*; In SPE International Symposium and Exhibition on Formation Damage Control: Lafayette, Louisiana, USA, 2012.

(85) Mansa, R.; Piegang, N.; B., G.; Detellier, C. Kaolinite Aggregation in Book-Like Structures from Non-Aqueous Media. *Clays Clay Miner.* **2017**, *65* (3), 193–205. https://doi.org/10.1346/CCMN.2017.064059.

(86) Żbik, M. S.; Raftery, N. A.; Smart, R. S. C.; Frost, R. L. *Kaolinite Platelet Orientation for XRD and AFM Applications*; 2010.

(87) Letaief, S.; Leclercq, J.; Liu, Y.; Detellier, C. Single Kaolinite Nanometer Layers Prepared by an in Situ Polymerization-Exfoliation Process in the Presence of Ionic Liquids. *Langmuir* **2011**, *27* (24), 15248–15254.

(88) Awad, M. E.; López-Galindo, A.; Setti, M.; El-Rahmany, M. M.; Iborra, C. V. Kaolinite in Pharmaceutics and Biomedicine. *Int. J. Pharm.* **2017**, *533* (1), 34–48.

(89) Samyn, P.; Schoukens, G.; Stanssens, D. Kaolinite Nanocomposite Platelets Synthesized by Intercalation and Imidization of Poly (Styrene-Co-Maleic Anhydride). *Materials (Basel).* **2015**, *8* (7), 4363–4388.

(90) Habibi, A.; Heidari, M. A.; Al-Hadrami, H.; Al-Ajmi, A.; Al-Wahaibi, Y.; Ayatollahi, S. Effect of Nanofluid Treatment on Water Sensitive Formation to Investigate Water Shock Phenomenon, an Experimental Study. *J. Dispers. Sci. Technol.* **2014**, *35* (7), 889–897.

(91) Yang, Y.; Siqueira, F. D.; Vaz, A. S.; You, Z.; Bedrikovetsky, P. Slow Migration of Detached Fine Particles over Rock Surface in Porous Media. *J. Nat. Gas Sci. Eng.* **2016**, *34*, 1159–1173.

(92) Huang, F.; Kang, Y.; You, L.; Li, X.; You, Z. Massive Fines Detachment Induced by Moving Gas-Water Interfaces during Early Stage Two-Phase Flow in Coalbed Methane Reservoirs. *Fuel* **2018**, *222*, 193–206.

(93) Gomez-Flores, A.; Bradford, S. A.; Hwang, G.; Choi, S.; Tong, M.; Kim, H. Shape and Orientation of Bare Silica Particles Influence Their Deposition under Intermediate Ionic Strength: A Study with QCM--D and DLVO Theory. *Colloids Surfaces A Physicochem. Eng. Asp.* **2020**, *599* (124921), 10.

(94) El-Monier, E. A.; Nasr-El-Din, H. A. Mitigation of Fines Migration Using a New Clay Stabilizer: A Mechanistic Study; SPE European Formation Damage Conference: Noordwijk, The Netherlands, 2011.

(95) Sanaei, A.; Tavassoli, S.; Sepehrnoori, K. Investigation of Modified Water Chemistry for Improved Oil Recovery: Application of DLVO Theory and Surface Complexation Model. *Colloids Surfaces A Physicochem. Eng. Asp.* **2019**, *574*, 131–145.

(96) Jung, J.; Cao, S.; Al-Raoush, R.; Alshibli, K. Fines Migration and Clogging Behavior in Methane Hydratebearing Sediments. In *Qatar Foundation Annual Research Conference Proceedings*; Hamad bin Khalifa University Press (HBKU Press): Ar-Rayyan, Qatar, 2018.

(97) Jung, J.; Kang, H.; Cao, S. C.; Al-Raoush, R. I.; Alshibli, K.; Lee, J. Y. Effects of Fine-Grained Particles' Migration and Clogging in Porous Media on Gas Production from Hydrate-Bearing Sediments. *Geofluids* **2019**, *2019* (5061216), 11.

https://doi.org/10.1155/2019/5061216.

(98) Cao, S. C.; Jang, J.; Jung, J.; Waite, W. F.; Collett, T. S.; Kumar, P. 2d Micromodel Study of Clogging Behavior of Fine-Grained Particles Associated with Gas Hydrate Production in NGHP-02 Gas Hydrate Reservoir Sediments. *Mar. Pet. Geol.* **2019**, *108*, 714–730. https://doi.org/10.1016/j.marpetgeo.2018.09.010.

(99) Yuan, B.; Moghanloo, R. G. Analytical Modeling Nanoparticles-Fines Reactive Transport in Porous Media Saturated with Mobile Immiscible Fluids. *AIChE J* **2019**, *65* (10), 15. https://doi.org/10.1002/aic.16702.

(100) Shuang, C.; Jung, J.; Kwon, T. The Characteristics of Fines Migration and Clogging of Sediments Recovered from the Gas Hydrate Deposits from the Ulleng Basin, East Sea, Korea; Proceedings of the XVII ECSMGE: Reykjavík, Iceland, 2019.

(101) Derjaguin, B.; Landau, L. The Theory of Stability of Highly Charged Lyophobic Sols and Coalescence of Highly Charged Particles in Electrolyte Solutions. *Acta Physicochim. URSS* **1941**, *14* (633–52), 58.

(102) Verwey, E. J. W. *Theory of the Stability of Lyophobic Colloids: The Interaction of Sol Particles Having an Electric Double Layer*; Elsevier Pub. Co.: New York, 1948.

(103) Loeb, A. L.; Overbeek, J. T. G.; Wiersema, P.; King, C. The Electrical Double Layer around a Spherical Colloid Particle. *J. Electrochem. Soc.* **1961**, *108* (12), 269C.

(104) Zou, W.; Zhao, J.; Sun, C. Adsorption of Anionic Polyacrylamide onto Coal and Kaolinite Calculated from the Extended DLVO Theory Using the van Oss-Chaudhury-Good Theory. *Polymers (Basel).* **2018**, *10* (2), 113.

(105) *Encyclopedic Dictionary of Polymers*; Gooch, J. W., Ed.; Springer New York: New York, NY, 2010.

(106) Brewer, J.; Hunter, A. *Multimethod Research: A Synthesis of Styles*; Sage Publications Inc.: New York, USA., 1989.

(107) Elimelech, M.; Gregory, J.; Williams, R. ; Particle Deposition and Aggregation. *Elsevier: Amsterdam, The Netherlands* **1995**, 113–156.

(108) Evans, D. F.; Wennerstrom, H. *Colloidal Domain*; Wiley-Vch, 1999.

(109) Abramson, H.; Moyer, L.; Gorin, M. : *Electrophoresis of Proteins*; Reinhold Publishing Corporation: New York, NY, 1942.

(110) Hogg, R.; Healy, T. W.; Fuerstenau, D. W. Mutual Coagulation of Colloidal

Dispersions. *Trans. Faraday Soc.* **1966**, *62*, 1638–1651.

(111) Gregory, J. Interaction of Unequal Double Layers at Constant Charge. *J. Colloid Interface Sci.* **1975**, *51* (1), 44–51.

(112) Ruckenstein, E.; Prieve, D. C. Adsorption and Desorption of Particles and Their Chromatographic Separation. *AIChE J* **1976**, *22* (2), 276–283.

(113) Schumacher, G. A.; van de Ven, T. G. M. Brownian Motion of Charged Colloidal Particles Surrounded by Electric Double Layers. *Faraday Discuss. Chem. Soc.* **1987**, *83*, 75–85.

(114) Chheda, P.; Grasso, D.; van Oss, C. J. Impact of Ozone on Stability of Montmorillonite Suspensions. *J. Colloid Interface Sci.* **1992**, *153* (1), 226–236.

(115) Israelachvili, J. N. *Intermolecular and Surface Forces*, 3rd ed.; Elsevier Academic press: Waltham, USA, 2015.

(116) Khilar, K. C.; Fogler, H. S. *Migrations of Fines in Porous Media*; Springer Science & Business Media, 1998; Vol. 12.

(117) Masliyah, J. H.; Bhattacharjee, S. *Electrokinetic and Colloid Transport Phenomena*; John Wiley & Sons, 2006.

(118) Badawy, E.; M., A.; Scheckel, K. G.; Suidan, M.; Tolaymat, T. The Impact of Stabilization Mechanism on the Aggregation Kinetics of Silver Nanoparticles. *Sci. Total Env.* **2012**, *429*, 325–331.

(119) Peng, M.; Duignan, T. T.; Nguyen, A. V. Significant Effect of Surfactant Adsorption Layer Thickness in Equilibrium Foam Films. *J. Phys. Chem. B* **2020**, *124* (25), 5301–5310.

(120) Elimelech, M.; Gregory, J.; Jia, X.; Williams, R. *Modelling of Particle Deposition onto Ideal Collectors, Particle Deposition and Aggregation: Measurement, Modelling and Simulation*; Butterworth–Heinemann: Woburn, UK, 1995.

(121) Xie, Q.; Chen, Y.; You, L.; Hossain, M. M.; Saeedi, A. Drivers of Wettability Alteration for Oil/Brine/Kaolinite System: Implications for Hydraulic Fracturing Fluids Uptake in Shale Rocks. *Energies* **2018**, *11* (7), 1666.

(122) Hunter, R. J. *Principles and Applications. Zeta Potential in Colloid Science*; Academic press: New York, 1981.

(123) Oldham, K. B. A. Gouy–Chapman–Stern Model of the Double Layer at a

(Metal)/(Ionic Liquid) Interface. *J. Electroanal. Chem.* **2008**, *613* (2), 131–138.

(124) Rouxel, D.; Hadji, R.; Vincent, B.; Fort, Y. Effect of Ultrasonication and Dispersion Stability on the Cluster Size of Alumina Nanoscale Particles in Aqueous Solutions. *Ultrason. Sonochem* **2011**, *18* (1), 382–388.

(125) Priya, K. R.; Suganthi, K.; Rajan, K. Transport Properties of Ultra-Low Concentration CuO–Water Nanofluids Containing Non-Spherical Nanoparticles. *Int. J. Heat Mass Transf.* **2012**, *55* (17–18), 4734–4743.

(126) Suganthi, K.; Rajan, K. Temperature Induced Changes in ZnO–Water Nanofluid: Zeta Potential, Size Distribution and Viscosity Profiles. *Int. J. Heat Mass Transf.* **2012**, *55* (25–26), 7969–7980.

(127) Bayat, A. E.; Junin, R.; Shamshirband, S.; Chong, W. T. Transport and Retention of Engineered Al2O3, TiO2, and SiO2 Nanoparticles through Various Sedimentary Rocks. *Sci. Rep* **2015**, *5* (14264).

(128) Alomair, O. A.; Matar, K. M.; Alsaeed, Y. H. Experimental Study of Enhanced-Heavy-Oil Recovery in Berea Sandstone Cores by Use of Nanofluids Applications. *SPE Reserv. Eval. Eng.* **2015**, *18* (03), 387–399.

(129) Sabiha, M.; Mostafizur, R.; Saidur, R.; Mekhilef, S. Experimental Investigation on Thermo Physical Properties of Single Walled Carbon Nanotube Nanofluids. *Int. J. Heat Mass Transf.* **2016**, *93*, 862–871.

(130) Adil, M.; Zaid, H. M.; Chuan, L. K.; Latiff, N. R. A. Effect of Dispersion Stability on Electrorheology of Water-Based ZnO Nanofluids. *Energy & Fuels* **2016**, *30* (7), 6169–6177.

(131) Lee, J.; Moesari, E.; Dandamudi, C. B.; Beniah, G.; Chang, B.; Iqbal, M.; Fei, Y.; Zhou, N.; Ellison, C. J.; Johnston, K. P. Behavior of Spherical Poly (2-Acrylamido-2-Methylpropanesulfonate) Polyelectrolyte Brushes on Silica Nanoparticles up to Extreme Salinity with Weak Divalent Cation Binding at Ambient and High Temperature. *Macromolecules* **2017**, *50* (19), 7699–7711.

(132) Al-Anssari, S.; Arif, M.; Wang, S.; Barifcani, A.; Iglauer, S. Stabilising Nanofluids in Saline Environments. *J. Colloid Interface Sci.* **2017**, *508*, 222–229.

(133) Abdelfatah, E.; Kang, K.; Pournik, M.; Shiau, B.; Harwell, J.; Haroun, M.; Rahman, M. Study of Nanoparticle Adsorption and Release in Porous Media Based on the

DLVO Theory. In *SPE Latin America and Caribbean Petroleum Engineering Conference*; OnePetro: Buenos Aires, Argentina, 2017.

(134) Skoglund, S.; Blomberg, E.; Wallinder, I. O.; Grillo, I.; Pedersen, J. S.; Bergström, L. M. A Novel Explanation for the Enhanced Colloidal Stability of Silver Nanoparticles in the Presence of an Oppositely Charged Surfactant. *Phys. Chem. Chem. Phys.* **2017**, *19* (41), 28037–28043.

(135) Choudhary, R.; Khurana, D.; Kumar, A.; Subudhi, S. Stability Analysis of Al2O3/Water Nanofluids. *J. Exp. Nanosci.* **2017**, *12* (1), 140–151.

(136) Upendar, S.; Mani, E.; Basavaraj, M. G. Aggregation and Stabilization of Colloidal Spheroids by Oppositely Charged Spherical Nanoparticles. *Langmuir* **2018**, *34* (22), 6511–6521.

(137) Kuang, W.; Saraji, S.; Piri, M. A Systematic Experimental Investigation on the Synergistic Effects of Aqueous Nanofluids on Interfacial Properties and Their Implications for Enhanced Oil Recovery. *Fuel* **2018**, *220*, 849–870.

(138) Ma, L.; Luo, P.; He, Y.; Zhang, L.; Fan, Y.; Jiang, Z. Ultra-Stable Silica Nanoparticles as Nano-Plugging Additive for Shale Exploitation in Harsh Environments. *Nanomaterials* **2019**, *9* (12), 1683.

(139) Siddiqui, F.; Tso, C.; Chan, K.; Fu, S.; Chao, C. Y. On Trade-off for Dispersion Stability and Thermal Transport of Cu-Al2O3 Hybrid Nanofluid for Various Mixing Ratios. *Int. J. Heat Mass Transf.* **2019**, *132*, 1200–1216.

(140) Siddiqui, F. R.; Tso, C.; Chan, K. C.; Fu, S. C.; Chao, C. Y. Dataset on Critical Parameters of Dispersion Stability of Cu/Al2O3 Nanofluid and Hybrid Nanofluid for Various Ultra-Sonication Times. *Data Br.* **2019**, *22*, 863–865.

(141) Aramendiz, J.; Imqam, A. Water-Based Drilling Fluid Formulation Using Silica and Graphene Nanoparticles for Unconventional Shale Applications. *J. Pet. Sci. Eng.* **2019**, *179*, 742–749.

(142) Kumar, R. S.; Sharma, T. Stable SiO2--TiO2 Composite-Based Nanofluid of Improved Rheological Behaviour for High-Temperature Oilfield Applications. *Geosystem Eng.* **2020**, *23* (1), 51–61.

(143) Wang, Z.; Babadagli, T.; Maeda, N. Preliminary Screening and Formulation of New Generation Nanoparticles for Stable Pickering Emulsion in Cold and Hot Heavy-Oil

Recovery. *SPE Reserv. Eval. Eng.* **2020**, *24* (01), 66–79. https://doi.org/10.2118/200190-PA.

(144) Yousef, A. A.; Al-Saleh, S.; Al-Jawfi, M. S. The Impact of the Injection Water Chemistry on Oil Recovery from Carbonate Reservoirs. In *SPE EOR Conference at Oil and Gas West Asia*; OnePetro: Muscat, Oman, 2012.

(145) Nasralla, R. A.; Nasr-El-Din, H. A. Double-Layer Expansion: Is It A Primary Mechanism of Improved Oil Recovery by Low-Salinity Waterflooding? *SPE Reserv. Eval. Eng.* **2012**, *17* (01), 49–59.

(146) Chen, L.; Zhang, G.; Wang, L.; Wu, W.; Ge, J. Zeta Potential of Limestone in a Large Range of Salinity. *Colloids Surfaces A Physicochem. Eng. Asp.* **2014**, *450*, 1–8.

(147) Yao, J.; Han, H.; Hou, Y.; Gong, E.; Yin, W. A Method of Calculating the Interaction Energy between Particles in Minerals Flotation. *Math. Probl. Eng.* **2016**, *2016*.

(148) Alghamdi, A.; Ayirala, S.; Alotaibi, M.; Alyousef, A. Electro-Kinetic Induced Wettability Alteration for Enhanced Oil Recovery in Carbonates. In *International Petroleum Technology Conference*; OnePetro: Dhahran, Kingdom of Saudi Arabia, 2020.

(149) Ruan, B.; Wu, P.; Liu, J.; Jiang, L.; Wang, H.; Qiao, J.; Zhu, N.; Dang, Z.; Luo, H.; Yi, X. Adhesion of Sphingomonas Sp. GY2B onto Montmorillonite: A Combination Study by Thermodynamics and the Extended DLVO Theory. *Colloids Surfaces B Biointerfaces* **2020**, *192* (111085).

(150) Hibbeler, J.; Garcia, T.; Chavez, N. *An Integrated Long-Term Solution for Migratory Fines Damage*; In SPE Latin American and Caribbean Petroleum Engineering Conference: Port-of-Spain, Trinidad and Tobago, 2003.

(151) Al-Dahlan, M.; Nasr-El-Din, H.; Al-Qahtani, A. Evaluation of Retarded HF Acid Systems. In *SPE International Symposium on Oilfield Chemistry*; Houston, Texas, 2001.

(152) Kakadjian, S.; Zamora, F.; Venditto, J. J. Zeta Potential Altering System for Increased Fluid Recovery, Production, and Fines Control; In International Symposium on Oilfield Chemistry: Houston, Texas, U.S.A., 2007.

(153) Valdya, R. N.; Fogler, H. S. Fines Migration and Formation Damage: Influence of PH and Ion Exchange. *SPE Prod. Eng.* **1992**, *7* (04), 325–330.

(154) Diez, R.; Medina, O. E.; Giraldo, L. J.; Cortés, F. B. Development of Nanofluids for the Inhibition of Formation Damage Caused by Fines Migration: Effect of the Interaction of Quaternary Amine (CTAB) and MgO Nanoparticles. *Nanomaterials* **2020**, *10* (5), 928.

(155) Huang, T.; Crews, J. B.; Willingham, J. R.; Belcher, C. K. *Nano-Sized Particles for Formation Fines Fixation*; In U.S. Patent Application 13/415: 505, filed October 25, 2012.

(156) Franco, C. A.; Zabala, R.; Cortés, F. B. Nanotechnology Applied to the Enhancement of Oil and Gas Productivity and Recovery of Colombian Fields. *J. Pet. Sci. Eng.* **2017**, *157*, 39–55.

(157) Li, S.; Torsæter, O.; Lau, H. C.; Hadia, N. J.; Stubbs, L. P. The Impact of Nanoparticle Adsorption on Transport and Wettability Alteration in Water-Wet Berea Sandstone: An Experimental Study. *Front. Phys.* **2019**, *7*, 74.

(158) Zhang, T.; Murphy, M. J.; Yu, H.; Bagaria, H. G.; Yoon, K. Y.; Neilson, B. M.; Bielawski, C. W.; Johnston, K. P.; Huh, C.; Bryant, S. L. Investigation of Nanoparticle Adsorption during Transport in Porous Media. *SPE J.* **2015**, *20* (04), 667–677.

(159) Yu, J.; An, C.; Mo, D.; Liu, N.; Lee, R. Study of Adsorption and Transportation Behavior of Nanoparticles in Three Different Porous Media. In *SPE improved oil recovery symposium*; OnePetro, 2012.

(160) Yuan, B.; Wang, W.; Moghanloo, R. G.; Su, Y.; Wang, K.; Jiang, M. Permeability Reduction of Berea Cores Owing to Nanoparticle Adsorption onto the Pore Surface: Mechanistic Modeling and Experimental Work. *Energy & Fuels* **2017**, *31* (1), 795–804.

(161) Collini, H.; Li, S.; Jackson, M. D.; Agenet, N.; Rashid, B.; Couves, J. Zeta Potential in Intact Carbonates at Reservoir Conditions and Its Impact on Oil Recovery during Controlled Salinity Waterflooding. *Fuel* **2020**, *266*, 116927.

(162) HASANNEJAD, R.; Pourafshary, P.; Vatani, A.; Sameni, A. Application of Silica Nanofluid to Control Initiation of Fines Migration. *Pet. Explor. Dev.* **2017**, *44* (5),

850–859.

(163) Shehata, A. M.; Nasr-El-Din, H. A. Zeta Potential Measurements: Impact of Salinity on Sandstone Minerals. *Proc. - SPE Int. Symp. Oilf. Chem.* **2015**, *2*, 789–805. https://doi.org/10.2118/173763-MS.

(164) Walker, E.; Glover, P. W. J. Measurements of the Relationship between Microstructure, PH, and the Streaming and Zeta Potentials of Sandstones. *Transp. porous media* **2018**, *121*, 183–206.

(165) Sahai, N. Is Silica Really an Anomalous Oxide? Surface Acidity and Aqueous Hydrolysis Revisited. *Environ. Sci. Technol.* **2002**, *36* (3), 445–452.

(166) Jeelani, P. G.; Mulay, P.; Venkat, R.; Ramalingam, C. Multifaceted Application of Silica Nanoparticles. A Review. *Silicon* **2020**, *12* (6), 1337–1354. https://doi.org/10.1007/s12633-019-00229-y.

(167) Cerda, C. M. Mobilization of Kaolinite Fines in Porous Media. *Colloids and Surfaces* **1987**, *27* (1–3), 219–241.

(168) Bedrikovetsky, P.; Vaz, A.; Machado, F.; Zeinijahromi, A.; Borazjani, S. Well Productivity Decline Due to Fines Migration and Production:(Analytical Model for the Regime of Strained Particles Accumulation). In *SPE European Formation Damage Conference*; OnePetro, 2011.

(169) Chequer, L.; Nguyen, C.; Loi, G.; Zeinijahromi, A.; Bedrikovetsky, P. Fines Migration in Aquifers: Production History Treatment and Well Behaviour Prediction. *J. Hydrol.* **2021**, 126660.

(170) Civan, F. *Reservoir Formation Damage-Fundamentals, Modeling, Assessment and Mitigation*, 3rd ed.; Gulf Professional Publishing: Houston, TX, 2016.

(171) Wilson, M. J.; Wilson, L.; Patey, I.; Shaw, H. The Influence of Individual Clay Minerals on Formation Damage of Reservoir Sandstones: A Critical Review with Some New Insights. *Clay Miner.* **2014**, *49* (2), 147–164.

(172) Kamal, M. S.; Mahmoud, M.; Hanfi, M.; Elkatatny, S.; Hussein, I. Clay Minerals Damage Quantification in Sandstone Rocks Using Core Flooding and NMR. *J. Pet. Explor. Prod. Technol.* **2019**, *9* (1), 593–603.

(173) Zeinijahromi, A.; Nguyen, T. K.; Bedrikovetsky, P. Mathematical Model for Fines-Migration-Assisted Waterflooding with Induced Formation Damage. *Spe J.* **2013**,

18 (03), 518–533.

(174) Kanimozhi, B.; Rajkumar, P.; Kumar, R. S.; Mahalingam, S.; Thamizhmani, V.; Selvakumar, A.; Ravikumar, S.; Kesavakumar, R.; Pranesh, V. Kaolinite Fines Colloidal-Suspension Transport in High Temperature Porous Subsurface Aqueous Environment: Implications to the Geothermal Sandstone and Hot Sedimentary Aquifer Reservoirs Permeability. *Geothermics* **2021**, *89*, 101975.

(175) Shakeel, M.; Pourafshary, P.; Rehan Hashmet, M. Hybrid Engineered Water–Polymer Flooding in Carbonates: A Review of Mechanisms and Case Studies. *Appl. Sci.* **2020**, *10* (17), 6087.

(176) Shakeel, M.; Samanova, A.; Pourafshary, P.; Hashmet, M. R. Capillary Desaturation Tendency of Hybrid Engineered Water-Based Chemical Enhanced Oil Recovery Methods. *Energies* **2021**, *14* (14), 4368.

(177) Shakeel, M.; Samanova, A.; Pourafshary, P.; Hashmet, M. R. Experimental Analysis of Oil Displacement by Hybrid Engineered Water/Chemical EOR Approach in Carbonates. *J. Pet. Sci. Eng.* **2021**, 109297.

(178) Muneer, R.; Rehan Hashmet, M.; Pourafshary, P. Fine Migration Control in Sandstones: Surface Force Analysis and Application of DLVO Theory. *ACS Omega* **2020**, *5* (49), 31624–31639. https://doi.org/10.1021/acsomega.0c03943.

(179) Alkafeef, S. F.; Alajmi, A. F. Streaming Potentials and Conductivities of Reservoir Rock Cores in Aqueous and Non-Aqueous Liquids. *Colloids Surfaces A Physicochem. Eng. Asp.* **2006**, *289* (1–3), 141–148.

(180) Xie, Q.; Saeedi, A.; Pooryousefy, E.; Liu, Y. Extended DLVO-Based Estimates of Surface Force in Low Salinity Water Flooding. *J. Mol. Liq.* **2016**, *221*, 658–665.

(181) Li, S.; Collini, H.; Jackson, M. D. Anomalous Zeta Potential Trends in Natural Sandstones. *Geophys. Res. Lett.* **2018**, *45* (20), 11–68.

(182) Vinogradov, J.; Jackson, M. D. Zeta Potential in Intact Natural Sandstones at Elevated Temperatures. *Geophys. Res. Lett.* **2015**, *42* (15), 6287–6294. https://doi.org/10.1002/2015GL064795.

(183) Farooq, U.; Tweheyo, M. T.; Sjöblom, J.; Oye, G. Surface Characterization of Model, Outcrop, and Reservoir Samples in Low Salinity Aqueous Solutions. *J. Dispers. Sci. Technol.* **2011**, *32* (4), 519–531.

https://doi.org/10.1080/01932691003756936.

(184) Singh, R.; Mohanty, K. K. Nanoparticle-Stabilized Foams for High-Temperature, High-Salinity Oil Reservoirs. In *SPE Annual Technical Conference and Exhibition*; OnePetro, 2017.

(185) Muneer, R.; Hashmet, M. R.; Pourafshary, P. DLVO Modeling to Predict Critical Salt Concentration to Initiate Fines Migration Pre-and Post-Nanofluid Treatment in Sandstones. *SPE J.* **2022**, 1–15.

(186) Habibi, A.; Ahmadi, M.; Pourafshary, P.; Ayatollahi, S.; Al-Wahaibi, Y. Reduction of Fines Migration by Nanofluids Injection: An Experimental Study. *SPE J.* **2013**, *18* (02), 309–318.

(187) Arab, D.; Pourafshary, P. Nanoparticles-Assisted Surface Charge Modification of the Porous Medium to Treat Colloidal Particles Migration Induced by Low Salinity Water Flooding. *Colloids Surfaces A Physicochem. Eng. Asp.* **2013**, *436*, 803–814.

(188) Assef, Y.; Arab, D.; Pourafshary, P. Application of Nanofluid to Control Fines Migration to Improve the Performance of Low Salinity Water Flooding and Alkaline Flooding. *J. Pet. Sci. Eng.* **2014**, *124*, 331–340.

(189) Zou, W.; Zhao, J.; Sun, C. Adsorption of Anionic Polyacrylamide onto Coal and Kaolinite Calculated from the Extended DLVO Theory Using the van Oss-Chaudhury-Good Theory. *Polymers (Basel).* **2018**, *10* (2), 113.

(190) Muneer, R.; Pourafshary, P.; Hashmet, M. R. Application of DLVO Modeling to Predict Critical PH for Fines Migration Pre-and Post-SiO2 and MgO Nanofluid Treatments in Sandstones. *J. Fluid Flow, Heat Mass Transf.* **2022**, *9* (1), 106.

(191) Ahmadi, M.; Habibi, A.; Pourafshary, P.; Ayatollahi, S. Zeta-Potential Investigation and Experimental Study of Nanoparticles Deposited on Rock Surface to Reduce Fines Migration. *SPE J.* **2013**, *18* (03), 534–544.

(192) Zhao, X.; Qiu, Z.; Gao, J.; Ren, X.; Li, J.; Huang, W. Mechanism and Effect of Nanoparticles on Controlling Fines Migration in Unconsolidated Sandstone Formations. *SPE J.* **2021**, 1–13.

(193) Sikiru, S. Ionic Transport and Influence of Electromagnetic Field Interaction Within Electric Double Layer in Reservoir Sandstone. *J. Mol. Liq.* **2021**, 117675.

(194) Saharawat, Y. S.; Chaudhary, N.; Malik, R. S.; Jat, M. L.; Singh, K.; Streck, T.

Artificial Ground Water Recharge and Recovery of a Highly Saline Aquifer. *Curr. Sci.* **2011**, 1211–1216.

(195) Bergendahl, J.; Grasso, D. Prediction of Colloid Detachment in a Model Porous Media: Hydrodynamics. *Chem. Eng. Sci.* **2000**, *55* (9), 1523–1532.

(196) Bradford, S. A.; Torkzaban, S.; Wiegmann, A. Pore-scale Simulations to Determine the Applied Hydrodynamic Torque and Colloid Immobilization. *Vadose Zo. J.* **2011**, *10* (1), 252–261.

(197) Bradford, S. A.; Torkzaban, S.; Shapiro, A. A Theoretical Analysis of Colloid Attachment and Straining in Chemically Heterogeneous Porous Media. *Langmuir* **2013**, *29* (23), 6944–6952.

(198) Brady, P. V.; Morrow, N. R.; Fogden, A.; Deniz, V.; Loahardjo, N.; Winoto, A. Electrostatics and the Low Salinity Effect in Sandstone Reservoirs. *Energy and Fuels* **2015**, *29* (2), 666–677. https://doi.org/10.1021/EF502474A.

(199) Derjaguin, B. V; Muller, V. M.; Toporov, Y. P. Effect of Contact Deformations on the Adhesion of Particles. *J. Colloid Interface Sci.* **1975**, *53* (2), 314–326.

(200) Bradford, S. A.; Yates, S. R.; Bettahar, M.; Simunek, J. Physical Factors Affecting the Transport and Fate of Colloids in Saturated Porous Media. *Water Resour. Res.* **2002**, *38* (12), 61–63.

(201) Tufenkji, N.; Elimelech, M. Breakdown of Colloid Filtration Theory: Role of the Secondary Energy Minimum and Surface Charge Heterogeneities. *Langmuir* **2005**, *21* (3), 841–852.

(202) Masciopinto, C.; Visino, F. Strong Release of Viruses in Fracture Flow in Response to a Perturbation in Ionic Strength: Filtration/Retention Tests and Modeling. *Water Res.* **2017**, *126*, 240–251.

(203) Shen, C.; Bradford, S. A.; Li, T.; Li, B.; Huang, Y. Can Nanoscale Surface Charge Heterogeneity Really Explain Colloid Detachment from Primary Minima upon Reduction of Solution Ionic Strength? *J. Nanoparticle Res.* **2018**, *20* (6), 1–18.

(204) Burdick, G. M.; Berman, N. S.; Beaudoin, S. P. Hydrodynamic Particle Removal from Surfaces. *Thin Solid Films* **2005**, *488* (1–2), 116–123.

(205) Goldman, A. J.; Cox, R. G.; Brenner, H. Slow Viscous Motion of a Sphere Parallel to a Plane Wall—II Couette Flow. *Chem. Eng. Sci.* **1967**, *22* (4), 653–660.

(206) O'neill, M. E. A Sphere in Contact with a Plane Wall in a Slow Linear Shear Flow. *Chem. Eng. Sci.* **1968**, *23* (11), 1293–1298.

(207) Saffman, P. G. The Lift on a Small Sphere in a Slow Shear Flow. *J. Fluid Mech.* **1965**, *22* (2), 385–400.

(208) Chrysikopoulos, C. V; Syngouna, V. I. Effect of Gravity on Colloid Transport through Water-Saturated Columns Packed with Glass Beads: Modeling and Experiments. *Environ. Sci. Technol.* **2014**, *48* (12), 6805–6813.

(209) Tan, X.; Liu, F.; Hu, L.; Reed, A. H.; Furukawa, Y.; Zhang, G. Evaluation of the Particle Sizes of Four Clay Minerals. *Appl. Clay Sci.* **2017**, *135*, 313–324.

(210) Vie, R.; Azema, N.; Quantin, J. C.; Touraud, E.; Fouletier, M. Study of Suspension Settling: A Approach to Determine Suspension Classification and Particle Interactions. *Colloids Surfaces A Physicochem. Eng. Asp.* **2007**, *298* (3), 192–200.

(211) Muneer, R.; Hashmet, M. R.; Pourafshary, P. Predicting the Critical Salt Concentrations of Monovalent and Divalent Brines to Initiate Fines Migration Using DLVO Modeling. *J. Mol. Liq.* **2022**, *352*, 118690.

(212) Ivanov, E.; Khan, A. M.; Yudin, A.; Stukan, M.; Khan, V.; Dovgilovich, L. Digital Revolution Provides a Step Change in Efficiency for Core Testing and Reservoir Upscaling for Acid Treatments. In *International Petroleum Technology Conference*; IPTC, 2022; p D031S106R003.

(213) Mansoori, J. A Review of Basic Upscaling Procedures: Advantages and Disadvantages. **1994**.

Appendix

$$10.21\pi\mu r_f v_s + 7.55\pi\mu r_f v_s = F_g + F_e$$

$$v_s = \frac{F_g + F_e}{\left(10.21\pi\mu r_f + 7.55\pi\mu r_f\right)}$$

$$2v\left(1 - \frac{\left(r_p - r_f\right)^2}{r_p^2}\right) = \frac{F_g + F_e}{\left(10.21\pi\mu r_f + 7.55\pi\mu r_f\right)}$$

$$2v\left(\frac{r_p^2 - \left(r_p - r_f\right)^2}{r_p^2}\right) = \frac{F_g + F_e}{\left(10.21\pi\mu r_f + 7.55\pi\mu r_f\right)}$$

$$2v\left(\frac{r_p^2 - r_p^2 - r_s^2 + 2r_p r_f}{r_p^2}\right) = \frac{F_g + F_e}{\left(10.21\pi\mu r_f + 7.55\pi\mu r_f\right)}$$

$$2v\left[\frac{r_s\left(2r_p - r_f\right)}{r_p^2}\right] = \frac{F_g + F_e}{\left(10.21\pi\mu r_f + 7.55\pi\mu r_f\right)}$$

$$v\left[\frac{2r_s\left(2r_p - r_f\right)}{r_p^2}\right] = \frac{F_g + F_e}{\left(10.21\pi\mu r_f + 7.55\pi\mu r_f\right)}$$

$$v = \left(F_g + F_e\right).\left[\frac{2r_f\left(2r_p - r_f\right)}{r_p^2}.\left(17.76\pi\mu r_f\right)\right]^{-1}$$